ABSTRACT

Title of Dissertation: **HEAT TRANSFER AND MECHANICAL DESIGN ANALYSIS OF SUPERCRITICAL GAS COOLING PROCESS OF CO_2 IN MICROCHANNELS**

Guohua Kuang, Doctor of Philosophy, 2006

Directed By: **Professor Michael Ohadi, Department of Mechanical Engineering**
Professor Balakumar Balachandran (Co-Advisor), Department of Mechanical Engineering

An extensive review of the literature indicates a lack of systematic study of supercritical CO_2 gas cooling and no prior work on CO_2/oil mixture in supercritical region, suggesting a lack of fundamental understanding of supercritical gas cooling process and a lack of comprehensive data that would help quantify the performance potential of CO_2 microchannel heat exchangers for engineering applications.

This dissertation presents a systematic and comprehensive study on gas cooling heat transfer characteristics of supercritical CO_2 in microchannels. Semi-empirical correlation is developed for predicting heat transfer performance of supercritical CO_2 in microchannels. The effect of oil addition on heat transfer performance has been experimentally investigated as well. It is shown that presence of lubricant oil mixed with

supercritical CO_2 in the heat exchangers can substantially affect heat transfer and pressure drop coefficients.

Because of the outstanding performance of supercritical CO_2 and its promising potential as a substitute for current refrigerants, attention has been paid to the design of CO_2 microchannel heat exchangers. The extensive review of the literature also indicates no previous study in systematically developing a simulation model for structural design of microchannel heat exchangers. The dissertation extends the research to the mechanical design analysis of microchannel heat exchangers. A finite-element method (FEM) based mechanical design analysis of tube-fin heat exchangers is carried out to develop a simulation model of the heat exchangers. The solid modeling and simulation scheme can be served as a guide for mechanical design of CO_2 heat exchangers. Experiments are conducted to validate the developed models as well.

HEAT TRANSFER AND MECHANICAL DESIGN ANALYSIS OF SUPERCRITICAL GAS COOLING PROCESS OF CO_2 IN MICROCHANNELS

By

Guohua Kuang

Dissertation submitted to the Faculty of the Graduate School of the
University of Maryland, College Park, in partial fulfillment
of the requirements for the degree of
Doctor of Philosophy
2006

Advisory Committee:
Professor Michael M. Ohadi, Chairman / Advisor
Professor Balakumar Balachandran, Co-Advisor
Professor Reinhard Radermacher
Professor Gary Pertmer
Professor Tien-Mo Shih

DEDICATION

To

My Mother

.

ACKNOWLEDGMENTS

I would like to express my deep appreciation to my advisor, Dr. Michael M. Ohadi and co-advisor, Dr. Balakumar Balachandran, for their sincere guidance and insight throughout this study. Special gratitude goes to Dr. Yuan Zhao for his generous guidance and enlightening suggestions.

The supervision and suggestions of Dr. Reinhard Radermacher and Dr. Yunho Hwang are highly appreciated. Thanks also go to the members of my advisory committee, Dr. Gary Pertmer, and Dr. Tien-Mo Shih, for their valuable suggestions and comments. Grateful acknowledgement goes to Dr. John Lawler, for his suggestions and generous dedication of his time.

In addition, I am thankful to all my colleagues and friends in the Smart and Small Thermal Systems Laboratory (S2TS) and Heat Pump Laboratory at University of Maryland for their support and collaboration.

Last, but in no sense the least, I express my thanks and appreciation to my family for their understanding, motivation and patience.

TABLE OF CONTENTS

TABLE OF CONTENTS……..…...…iv

LIST OF TABLES……..……..ix

LIST OF FIGURES……..……....x

CHAPTER 1 INTRODUCTION..……..……..…….…..1

1.1 Ozone Depletion and Global Warming…….....……...1

1.2 Phase-out of Refrigerants…...……..……4

1.3 HFC Mixture Refrigerants ……...……..…….5

1.4 Natural Refrigerants……..……...…5

1.5 Carbon Dioxide as Working Fluid in Refrigeration Systems ..……..…….9

1.6 Objectives of the Present Study ……..…….11

1.7 Scope ..……..…….12

CHAPTER 2 RESEARCH BACKGROUND…….……...…..14

2.1 Heat Transfer of Supercritical CO_2……..……..…..……14

2.1.1 Supercritical Fluid...……..…..…….…14

2.1.2 Pseudo-Critical Temperature…..……..…….15

2.1.3 Previous Studies on Heat Transfer of Supercritical CO_2……..…..…….18

2.2 Heat Transfer in Microchannels…..……..……..…..……..21

2.3 Heat Exchangers – Thermal Design & mechanical Design……..……..…..……..24

2.4 Heat Transfer Models for forced convection of Supercritical CO_2……..…....25

2.4.1 Gnielinski's Correlation...…….……..…..….25

2.4.2 Krasnoshchekov-Protopopov's Correlation ……..……..……..26

2.4.3 Petrov-Popov's Correlation ……..……..…..…..27

2.4.4 Ghajar-Asadi's Correlation...……...…….…..…27

2.4.5 Liao-Zhao's Correlation ……..……...……...…….28

2.4.6 Pitla et al's Correlation ……..……..……..…….29

2.4.7 Yoon et al's Correlation ……..……...……...…….29

2.4.8 Huai et al's Correlation……..……...……..…….30

2.5 Concluding Remarks…….……..…….30

CHAPTER 3 EXPERIMENTAL MEASUREMENTS OF HEAT TRANSFER AND PRESSURE DROP COEFFICIENTS FOR GAS COOLING OF SUPERCRITICAL CO_2 IN MICROCHANNELS ……..…..……32

3.1 Introduction……..……..……..…..32

3.2 Experimental Apparatus and Procedure.……...……...……...….33

3.3 Data Reduction..…….……..……...……...….39

3.3.1 Overall Heat Transfer Coefficient…….…….…….39

3.3.2 Waterside Heat Transfer Coefficient……..……..….41

3.4 Uncertainty Analysis…….……..……..…….……...45

3.5 Results and Discussion…….……...……...……47

3.5.1 Heat Transfer Coefficient…….…….…….……..49

3.5.2 Pressure Drop…….…….…….…..……53

3.6 Conclusions……...…….……..……..56

CHAPTER 4 DEVELOPMENT OF EMPIRICAL CORRELATIONS FOR HEAT TRANSFER OF SUPERCRITICAL CO_2 IN MICROCHANNELS……..…….57

4.1 Introduction……..…….…….57

4.2 Comparison of Experimental Data and Existing Correlations……..……58

4.2.1 Gnielinski's Correlation...…….……..…..….58

4.2.2 Krasnoshchekov-Protopopov's Correlation …….……..……..60

4.2.3 Ghajar-Asadi's Correlation...……...…..…61

4.2.4 Pitla et al's Correlation …….……..……62

4.2.5 Huai et al's Correlation…….……..……..64

4.3 Proposed Correlation of the Present Study…..……..…….……..65

4.4 Conclusions……...…….……..……..67

CHAPTER 5 GAS COOLING OF SUPER CRITICAL CO_2 IN MICRO-CHANNELS IN THE PRESENCE OF LUBRICATING OIL …...…68

5.1 Introduction……..……..……..…….68

5.2 Experimental Apparatus and Procedure.……..…….69

5.3 Data Analysis…….……..……....…….71

5.4 Results and Discussions…….……..……....…….71

5.4.1 PAG/AN oil...…….……..……...72

5.4.2 PAG oil...…….……..……..74

5.4.3 POE oil...…….……..……..75

5.4.3 Discussion..……..……..……..77

5.5 Conclusions……...…….……..……..…….78

CHAPTER 6 STRUCTURAL & DYNAMICAL ANALYSIS OF MICROCHANNEL HEAT EXCHANGERS ……..…….80

6.1 Introduction……..……..…..……..80

6.2 Static Stress Analysis - Manifold Design …….……82

6.2.1 Single-Tube Header..……..…..…….……82

6.2.2 Double-Tube Extrusion Header……..…….…….85

6.2.3 Inline Tube Header…….……..……88

6.3 Development of Solid Model & Simulation Scheme ……..…….88

6.3.1 Equivalent Geometry ……..……..…..…….….89

6.3.2 Fin Approximation ……..……..…..……..….93

6.3.2.1 Shell Element Approximation Method…….……...93

6.3.2.2 Effective Block Approximation Method…….……96

6.3.2.3 Comparison of Two Methods of Fin Approximation…….…….....99

6.3.3 Large-Scale Structure Modeling – Substructuring Technique …….…..…100

6.3.4 Experimental Verifications……..…….…..……..…103

6.3.4.1 Experiments with Plate-Fin Modules…….103

6.3.4.2 Experiments with a Heat Exchanger…….…….106

6.4 Implementations ……..……..…….……111

6.4.1 Temperature Effect ……..……..…..…….…….……111

6.4.2 Pressure Effect ....……..…….…….…….…….…..…113

6.4.3 Modal Analysis …....……..…….…….…….115

6.4.4 Harmonic Analysis ....……..…….…….……119

6.5 Case Study: Thermal & Mechanical Evaluation of a Heat Exchanger Design ……123

6.6 Design Guideline……..……..……..…...128

6.7 Conclusions ……..……..……..…...129

CHAPTER 7 CONCLUSIONS AND FUTURE WORK ……...….131

7.1 Conclusions ……..……...131

7.1.1 Gas Cooling of Supercritical CO_2 in Microchannels..……..…..…131

7.1.2 Correlation Development..…….……..…...132

7.1.3 Gas Cooling of CO_2/Oil Mixtures in Microchannels…….....134

7.1.4 Mechanical Design Analysis of Microchannels CO_2 Heat Exchanger…...135

7.2 Future Work……..…….…….....317

7.2.1 Un-Pairing Thermal Resistances in Test Section……....137

7.2.2 Oil Separation Techniques……..…138

7.2.3 Mechanical Design of Microchannels HX……..…141

7.2.4 Additional Recommendations for Future Work…….……141

REFERENCES……..…….143

LIST OF TABLES

Table 1.1 Most commonly known refrigerants and their ODP and GWP……..…….3

Table 1.2 Overview of selected natural refrigerants……..……..8

Table 1.3 Thermo-physical properties of CO_2 and R-134a at 5 / 10 / 15 °C…….....11

Table 2.1 CO_2 properties at pseudo-critical temperature……..……18

Table 2.2 Summary of studies on single-phase flow in microchannels……..……...23

Table 3.1 Sample uncertainty results ……..…...47

Table 6.1 Natural frequencies comparison……..…...91

Table 6.2 Comparison of first three natural frequencies among the full mesh and shell element cases……...96

Table 6.3 Effective properties of the effective solid block……..…106

Table 6.4 First natural frequency comparison between experimental results and simulation results……..…..106

Table 6.5 Natural Frequency Results of the Heat Exchanger……..……112

Table 6.6 Thermal effect on natural frequencies of HX unit……..…….114

Table 6.7 Pressure effect on natural frequencies of HX unit……..…….115

LIST OF FIGURES

Figure 1.1 A transcritical cycle of carbon dioxide……..……..11

Figure 2.1 Specific heat versus temperature of supercritical CO_2……..…….. ...16

Figure 2.2 Density versus temperature of supercritical CO_2…..……..….....16

Figure 2.3 Conductivity versus temperature of supercritical CO_2……..……..……....17

Figure 2.4 Viscosity versus temperature of supercritical CO_2…….…….....17

Figure 3.1 Schematics of experimental apparatus……..……..34

Figure 3.2 Schematics of the test section……..……36

Figure 3.3 Cross section of microchannels tube……..…….36

Figure 3.4 Schematic of water preheater…….…….37

Figure 3.5 Heat exchanger in water preheater loop…….…….37

Figure 3.6 Wilson plot result for waterside heat transfer coefficient…….……..45

Figure 3.7 T-s diagram of carbon dioxide along test section…….……..48

Figure 3.8 Specific heat and pseudo-critical temperature of CO_2…….……...49

Figure 3.9 Heat transfer coefficient at 8 *MPa* with different mass fluxes……..……..50

Figure 3.10 Heat transfer coefficient at 9 *MPa* with different mass fluxes……..…….51

Figure 3.11 Heat transfer coefficient at 10 *MPa* with different mass fluxes……..…...51

Figure 3.12 Heat transfer coefficient at 332 *kg/m2-s* with different pressure……...52

Figure 3.13 Heat transfer coefficient at 870 *kg/m2-s* with different pressure……...53

Figure 3.14 Pressure drop at 8 *MPa* with different mass fluxes……..…..54

Figure 3.15 Pressure drop at 9 *MPa* with different mass fluxes……..…..55

Figure 3.16 Pressure drop at 10 *MPa* with different mass fluxes……..……55

Figure 4.1 Comparison with Gnielinski's correlation……..…….59

Figure 4.2 Comparison with Krasnoshchekov-Protopopov's correlation……..…...61

Figure 4.3 Comparison with Ghajar-Asadi's correlation……..……62

Figure 4.4 Comparison with Pitla et al's correlation…….……...63

Figure 4.5 Comparison with Huai et al's correlation……..……..64

Figure 4.6 Curve-fitting for the proposed correlation……..…….66

Figure 5.1 Test section for oil mixture tests…….……70

Figure 5.2 Heat transfer coefficient (PAG/AN oil addition)…….……...73

Figure 5.3 Pressure drop (PAG/AN oil addition)…….……....73

Figure 5.4 Heat transfer coefficient (PAG oil addition)…….……..74

Figure 5.5 Pressure drop (PAG oil addition)…….……...75

Figure 5.6 Heat transfer coefficient (POE oil addition)…….…..……..76

Figure 5.7 Pressure drop (POE oil addition)……..……...76

Figure 6.1 Mesh elements of single-tube header in ANSYS……..……..84

Figure 6.2 Failure results for single-tube header (pressure of 25 *MPa*)……..…….84

Figure 6.3 Mesh elements of double-tube extrusion header in ANSYS……..…….86

Figure 6.4 Failure results for double-tube extrusion header (pressure of 25 *MPa*)……..86

Figure 6.5 Mesh elements of inline-tube header in ANSYS…….....87

Figure 6.6 Failure results for inline-tube header (pressure of 25 *MPa*)…….…...87

Figure 6.7 Cross section of microchannel tube……..…...89

Figure 6.8 Alternative cross section……..…89

Figure 6.9 Two-port cross section and equivalent rectangular cross section……...90

Figure 6.10 First 4 vibration modes: two-port tube and equivalent rectangular bar……..92

Figure 6.11 Mesh elements of the HX unit using shell element approximation.....94

Figure 6.12 Mesh elements of the HX unit using full meshing……..…...94

Figure 6.13 A simple imaginary single-fin heat exchanger unit……..…..95

Figure 6.14 Displacement field of the fin array……..…...98

Figure 6.15 Displacement field of the effective block……..…….98

Figure 6.16 Shell-element approximation for the clamped-clamped heat exchanger unit (first natural frequency of 71.9Hz)……...99

Figure 6.17 Effective block approximation for the clamped-clamped heat exchanger unit (first natural frequency of 72.5Hz)…….100

Figure 6.18 Heat exchanger example (including 11 HX units)……..……..101

Figure 6.19 Meshing of HX unit for super-element…….……...101

Figure 6.20 Comparison of meshing with super-element to that with full meshing…..102

Figure 6.21 Clamped-free plate-fin-plate structure…….……104

Figure 6.22 Clamped-free plate-fin-plate-fin-plate structure…….……..104

Figure 6.23 Fin array and the effective block in meshes…….……105

Figure 6.24 Microchannel heat exchanger……..…….107

Figure 6.25 Fin arrays in microchannel heat exchanger……..……107

Figure 6.26 Fin array model used in the heat exchanger…….……108

Figure 6.27 Modified effective block approximation of fin array……..…….108

Figure 6.28 Simulation model of the heat exchanger……..……109

Figure 6.29 First vibration modes about the Y-axis and about the Z-axis……..…….110

Figure 6.30 Experimentally obtained power spectra indicating possible natural frequency locations……..110

Figure 6.31 Temperature field of a HX unit…….……...112

Figure 6.32 Meshing elements of the one-channel HX unit…….……...114

Figure 6.33 Three-pass HX unit with 300 *mm* in each pass…….……...116

Figure 6.34 First natural frequency versus pass length……..……..116

Figure 6.35 3-pass HX unit with 500 *mm* in each pass……..……..118

Figure 6.36 5-pass HX unit with 300 *mm* in each pass……..……..118

Figure 6.37 Schematic of a linear system……..……..119

Figure 6.38 Harmonic forces on clamped-clamped HX unit……..…….120

Figure 6.39 Frequency-response function with damping ratio of 0.1……..……121

Figure 6.40 Stress distribution with harmonic forces at 72Hz……..……...122

Figure 6.41 Max amplitude of FRF versus pass length…….……..123

Figure 6.42 Evaluated heat exchanger unit……...……124

Figure 6.43 Simulation model in FLUENT……..……...125

Figure 6.44 First natural frequency and heat transfer coefficient versus fin thickness……..126

Figure 6.45 Pressure drop and HX density versus fin thickness……..……126

Figure 6.46 First natural frequency and heat transfer coefficient versus fin pitch…..….127

Figure 6.47 Pressure drop and HX density versus fin pitch……....127

Figure 7.1 Settling chamber oil separator……...….138

Figure 7.2 Coalescing filtration oil separator…….…….139

Figure 7.3 Cyclone oil separator……..……139

CHAPTER 1

INTRODUCTION

Refrigerants are the working fluids in refrigeration, air-conditioning, and heat pump systems. These systems are necessary for comfortable and healthy living environments. An "ideal" refrigerant is chemically stable and inert, has excellent thermal and fluid flow characteristics, is compatible with common materials, is soluble in lubricating oils, is nontoxic and nonflammable, has low cost, and is environmentally acceptable. Since no single fluid meets all these attributes, a variety of refrigerants has been developed and applied to HVAC&R systems. However, with the growing awareness of the dual threats of ozone depletion and global warming, significant research activity has been directed toward the identification and development of environmentally benign refrigerants.

1.1 Ozone Depletion and Global Warming

Due to their low cost, high compatibility, and good thermal characteristics, chlorofluorocarbons (CFCs) were once used extensively in refrigerators and air conditioners. However, their use was found to deplete the ozone layer (Rowland and Molina 1974). In 1987, the "Montreal Protocol on Substances that Deplete the Ozone Layer," the first worldwide agreement on an environmental issue, went into force to regulate the production and trade of ozone-depleting substances such as CFCs. The production of CFCs has been forbidden in industrialized countries since January 1, 1996. The phase-out of chlorofluorocarbon (CFC) refrigerants, as mandated by the Montreal Protocol, left the HVAC&R industry no choice but to develop alternatives. As a result,

research efforts in the past decade have identified HCFC (hydrochlorofluorocarbon) refrigerants with much lower ozone depletion potentials (ODP) and HFC (hydrofluorocarbon) refrigerants with zero ODP.

In addition to ozone depletion, most traditional refrigerants have also been identified as a cause of global warming, as found in the world meteorological organization's international conference in 1985. As shown in Table 1.1 (Zhao, 2001), neither HCFCs nor HFCs sufficiently reduce the geophysical problem of global warming. There are two types of global warming effects: the direct global warming potential (DGWP) due to the emission of the refrigerants themselves, and the indirect global warming potential (IDGWP) due to the emission of CO_2 by consuming the energy obtained by the combustion of fossil fuels. Based on such concerns, HCFCs have been scheduled for phase-out by 2030 as well.

Table 1.1 Most commonly known refrigerants and their ODP and GWP (Zhao, 2001)

Refrigerant			Formula	ODP[1]	GWP[2]	Phase-out
Type	Name or Composition	No.				
CFCs	Trichlorofluoromethane	R-11	CCl_3F	1.0	4000	1996
	Dichlorodifluoromethane	R-12	CCl_2F_2	1.0	8500	
	Chloropentafluoroethane	R-115	$CClF_2CF_3$	0.6	9300	
	Trichlorotrifluoroethane	R-113	CCl_2FCClF_2	0.1	4800-6000	
HCFCs	Chlorodifluoromethane	R-22	$CHClF_2$	0.055	1700	2030
	Dichlorofluoroethane	R-141b	CCl_2FCH_3	0.11	630	
	Chlorodifluoroethane	R-142b	CH_3CClF_2	0.065	2000	
	R-22/115 (48.8/51.2)	R-502	-	0.333	5575	
HFCs	Pentafluoroethane	R-125	CHF_2CF_3	0	3200	Undetermined
	Tetrafluoroethane	R-134a	CH_2FCF_3	0	1300	
	Trifluoroethane	R-143a	CH_3CF_3	0	4400	
	Difluoroethane	R-152a	CH_3CHF_3	0	140	
	R-125/143a/134a (44/52/4)	R-404A	-	0	3750	
	R-32/125/134a (23/25/52)	R-407C	-	0	1600	
	R-32/125 (50/50)	R-410A	-	0	2200	
Natural Refrigerants	Air	-	-	0	0	Not likely
	Ammonia	R-717	NH_3	0	0	
	Carbon Dioxide	R-744	CO_2	0	1	
	Isobutene	R-600a	$CH(CH_3)_3$	0	3	
	Propane	R-290	C_3H_8	0	3	

1. The values of ODP are based on R-12 =1.0

2. The values of GWP are based on CO_2 = 1.0 for time horizon of 100 years.

1.2 Phase-Out of Refrigerants

The Montreal Protocol is an international treaty that controls the production of ozone-depleting substances, including refrigerants containing chlorine and/or bromine (U.N. 1994, 1996). The first version of the Protocol was signed September 16, 1987, by the European Economic Community (currently the European Union) and 24 nations, including the United States. As described in Chapter 18 of the ASHRAE Handbook of Fundamentals (2005), the Montreal Protocol was enacted on January 1 1989, and limits the 1998 production of specified CFCs to 50% of their 1986 levels. Starting in 1992, the production of specified halons (including R-13B1) was frozen at 1986 levels. Developing countries were granted additional time to meet these deadlines.

On June 14 1994, the Copenhagen Amendment to the Montreal Protocol, ratified by 58 parties, was enacted. It called for a complete cessation of the production of CFCs by January 1 1996, and of halons by January 1, 1994. Continued use from the existing (reclaimed or recycled) stock is permitted. Allowance is also provided for continued production for very limited "essential uses." In addition, HCFCs (including R-22) are to be phased out relative to a 1989 reference level for developed countries. Production was frozen at the reference level on January 1, 1996. Production will be limited to 65% of the reverence level by January 1, 2004; to 35% by January 1, 2010; to 10% by January 1, 2015; and to 0.5% of the reference level by January 1, 2020. Complete cessation of the production of HCFCs is called for by January 1, 2030. In addition to the international agreement, individual countries may enact domestic regulations for ozone-depleting compounds.

1.3 HFC Mixture Refrigerants

HFC mixture refrigerants, such as R-407C {R-32/125/134A (23/25/52)} and R-410A {R-32/125 (50/50)}, are currently proposed as replacements for CFCs and HCFCs. However, they are undergoing long-term testing to determine their reliability and hidden effects, since the extensive application of any unnatural substances may cause unexpected problems and should be used with caution. The production and use of hydrofluorocarbon (HFC) refrigerants (such as R-32, R-125, R-134a, and R-143a and their mixtures, including R-404, R-407, and R-410) are not regulated by the Montreal Protocol, but may be regulated by individual countries. However, uncertainties regarding the long-term effects of these refrigerant mixtures may put a cloud over the applications of these refrigerants and force the HVAC&R research community to continue work on finding new candidates to substitute for CFCs and their alternatives. The research community is therefore revisiting natural refrigerants as potentially viable substitutes to CFCs and their alternatives.

1.4 Natural Refrigerants

The environmental issues and the uncertainty of the effects of HFC-mixture refrigerants have promoted the research and investigation of new refrigerant alternatives. It has been suggested that the refrigeration industry bypass the HFCs altogether and employ “natural refrigerants” (Sanvordenker, 1997). "Natural refrigerants” refer to naturally occurring substances such as air, ammonia, carbon dioxide, isobutene, propane, and water. The use of these substances is expected to have the minimum adverse effect

on the environment. An overview of selected natural refrigerants is provided in Table 1.2 (Zhao, 2001).

The original application of natural refrigerants dates back to the middle of the nineteenth century when Linde, Perkins, Harrison, and others introduced pioneering refrigeration systems. In 1834, Perkins introduced the first refrigerant, sulfuric ether, in the first vapor compression refrigeration system. From the 1840s through 1920s, the main refrigerants in practical use were ammonia (NH_3) for large- and medium-size stationary systems, sulfur dioxide (SO_2) for household refrigerators and small commercial plants, and carbon dioxide (CO_2) for ship installations, with brine as a secondary refrigerant. CO_2 was also often used in stationary systems (Elefsen et al., 1995).

Midgley and Henne (1930) published papers on fluorochemical refrigerants as a result of their search for stable, nontoxic, nonflammable, efficient refrigerants. In 1931, dichlorodifluoromethane, CFC-12, was commercially produced (Downing, 1966). After the introduction of fluorochemical refrigerants, the early refrigerants, including CO_2, were replaced by many other CFCs, and later HCFCs. This course of action led to a drastic decline in the use of refrigerants other than CFCs and HCFCs after World War II. Only ammonia remained in use, though predominantly only in large industrial systems.

In 1998 Ohadi and Mo conducted a detailed review of natural refrigerants. They addressed the role of natural refrigerants in preventing or mitigating the problems associated with these phenomena (global warming, ozone depletion, etc.). Thermophysical properties and cycle performance of selected natural refrigerants were discussed and compared with their counterpart HCFC and HFC refrigerants. They concluded that while HFC blends have acceptable ODP, their GWP is high enough to

warrant a continued search for environmentally friendly refrigerants. The use of natural refrigerants appears to be one solution to this problem for immediate, as well as future applications. Research on natural refrigerants is therefore receiving renewed attention.

Table 1.2 Overview of selected natural refrigerants (Zhao, 2001)

Refrigerant	General Characteristics	Major Advantages	Major Disadvantages
Ammonia (NH_3)	Ammonia is a well-known refrigerant in large scale industrial refrigeration plants. It has been used as a refrigerant for more than 120 years, but until now it has not been widely used in small plants.	-More than 120 years of practical use -Excellent thermodynamic and thermophsical properties -Higher energy efficiency in most temperature ranges -Well known oil tolerance -Great tolerance to water contamination -Simple and immediate leak detection -No ODP or GWP -Lower cost -Smaller pipe dimensions leading to lower plant investments	-Toxic at low concentrations in air (above 500ppm) -No tolerance to some materials, e.g. copper -No miscibility with most known oils -High discharge temperatures -Flammable at 15-30% Vol.
Water (H_2O)	Environmentally attractive, water has potential as a long-term acceptable refrigerant. Water offers high plant energy efficiency.	-Higher Carnot COP due to the use of direct heat exchanger -High mechanical efficiency of compressor -Production of vacuum ice -Low energy consumption -No ODP or GWP	-Process under vacuum -Good only for cooling/ refrigeration above 0°C
Carbon Dioxide (CO_2)	In recent years, after the Montreal Protocol, much development activity has been devoted to CO_2 as a refrigerant. This development is based on new material technology which allows high pressures in the thermodynamic cycle. CO_2 is quite harmless; it is environmentally attractive, and is neither toxic, flammable nor explosive.	-Low weight and small dimensions of plant -Large refrigeration capacity -Tolerance with well known oils -Low compression ratio -Low environmental impact -Low price, ample supply	-High pressure -Low critical temperature (31°C)
Hydro-carbons	The measures taken to find suitable “natural” refrigerants as substitutes for CFC and HCFC have called attention to two hydrocarbons (propane and isobutene) that have properties similar to the most widely used CFCs and HCFCs.	-Compatible with materials normally used in refrigeration plants, such as copper and mineral oil -Similar physical properties to CFC-12 (isobutane) and HCFC-22 (propane) -Small amount of refrigerant needed -Lower prices than HFCs -Low environmental impact	-Flammable at concentration of 1-10% v/v (requires additional safety measures) -Smaller volumetric cooling capacity

1.5 Carbon Dioxide as Working Fluid in Refrigeration Systems

The development of refrigeration systems using CO_2 as a refrigerant began 1866 when Thaddeus created an ice production machine using CO_2 (Thevenot 1979). In 1880, Windhausen designed the first CO_2 compressor (Gosman, 1927). After the late 1800s, the use of CO_2 refrigeration systems increased. As a result of continuous efforts to improve efficiency, two-stage CO_2 machines were developed in 1889 in Great Britain (Thevnot, 1979). The multiple-effect CO_2 cycle was developed by Voorhess in 1905 (Thevenot, 1979). However, the use of CO_2 as a refrigerant declined drastically in the 1930s due to the appearance of CFCs and HCFCs, which offered lower absolute pressures and higher efficiencies in conventional vapor compression cycles.

Recently, however, CO_2 as a natural and environmentally favorable refrigerant has regained attention. Ozone depletion and global warming concerns call for the use of natural refrigerants. As discussed above, hydrofluorocarbons (HFCs) are replacement candidates, but have the disadvantages of high GWP, high cost, and unresolved issues regarding environmental impact. On the other hand, natural refrigerants, such as NH_3 and CO_2, have a low GWP, no ODP, and no adverse environmental effects (Lorentzen, 1995). Its low toxicity, non-flammability, and low cost make CO_2 the preferred refrigerant when compared with NH_3.

In addition to its environmental advantages, CO_2 offers certain attractive thermal characteristics. General physical and chemical properties of CO_2, as well as comparisons with those of other refrigerants, are listed in Chapter 19 of the ASHRAE Handbook of Fundamentals (2005). The thermo-physical properties listed include the standard

designation of characteristic properties, such as molecular mass, critical points, etc. Electrical properties, performance comparisons with other refrigerants, a safety classification, and CO_2's effect on several other materials are also provided. A brief chart and a saturated table of thermodynamic properties are given in Chapter 19 of the ASHRAE Handbook of Fundamentals (2005).

As a refrigerant, CO_2 offers thermodynamic and transport properties that are unique and substantially different than other conventional refrigerants, as mentioned by Devotta et al. (2000). Since the critical temperature of CO_2 is 31°C for air-conditioning applications, the heat rejection above 31°C is not by condensation, as in usual systems. This fact must lead to some changes in system design. Due to its higher volumetric capacity, which is five times higher than that of HCFC-22, the size of the system can also be reduced considerably.

Some important thermo-physical properties of CO_2 and comparisons with R-134a are listed in Table 1.3. As seen there, Carbon dioxide has a much smaller surface tension and liquid viscosity than R-134a. Lower surface tension facilitates bubble formation, thus resulting in higher heat transfer coefficients. Lower liquid viscosity indicates a smaller pressure drop when CO_2 flows in a tube or channel.

Recent CO_2 cycle research has focused on the development of a transcritical cycle. A thermodynamic model for transcritical carbon dioxide cycle is shown in Figure 1.1 (Robinson and Groll, 1998).

Table 1.3 Thermo-physical properties of CO_2 and R-134a at 5 / 10 / 15 °C

Refrigerant	CO_2	R-134a
P_{sat} (MPa)	3.969/4.502/5.086	0.350/0.414/0.488
Latent Heat (kJ/kg)	214.6/196.8/176.2	194.8/190.9/186.7
Surface Tension (mN/m)	3.53/2.67/1.88	11.0/10.3/9.6
Liq. Density (kg/m^3)	899.6/861.5/821.3	1277.1/1260.2/1242.8
Vap. Density (kg/m^3)	114.8/135.3/161.0	17.1/20.2/23.7
Liq. Viscosity (μPa·s)	95.9/86.7/77.2	270.3/254.3/239.7
Vap. Viscosity (μPa·s)	15.4/16.1/17.0	11.2/11.4/11.7
Liq. C_p (kJ/kg·K)	2.73/3.01/3.44	1.35/1.37/1.38
Vap. C_p (kJ/kg·K)	2.21/2.62/3.30	0.91/0.93/0.96

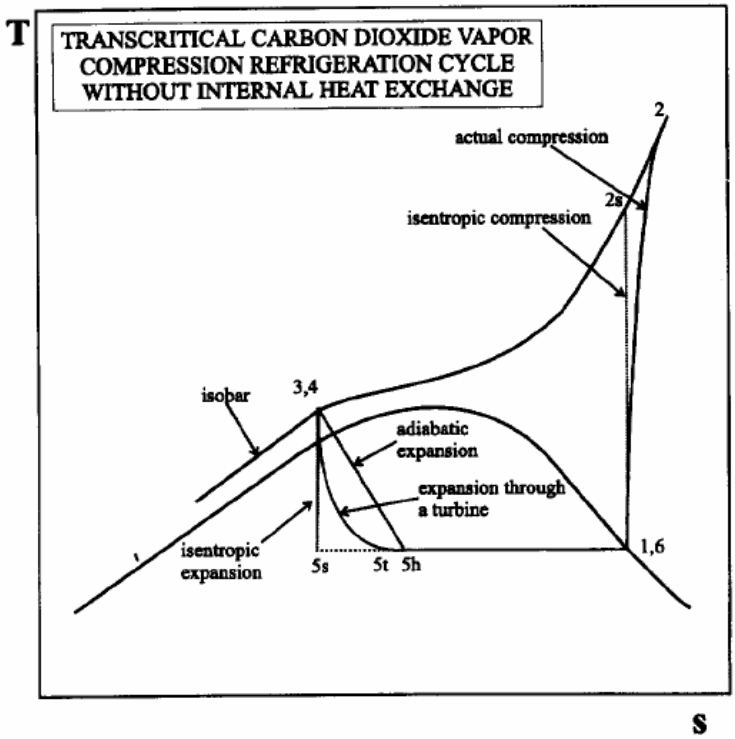

Figure 1.1. A transcritical cycle of carbon dioxide (Robinson and Groll 1998)

1.6 Objectives of the Present Study

The objectives of this study are to experimentally investigate the heat transfer characteristics in the gas cooling process of supercritical CO_2 in microchannels and to develop a simulation scheme for a CO_2 microchannel tube-fin heat exchanger design. Four major tasks are outlined to achieve these objectives:

- Quantify the gas cooling heat transfer coefficient and pressure drop of supercritical CO_2 in microchannels via experimental study.
- Develop semi-empirical correlations for the heat transfer coefficient in the supercritical gas cooling process.
- Quantify the influence of oil addition on the heat transfer coefficient and pressure drop in microchannels tube.
- Develop a FEM simulation scheme of structure and dynamic analysis for a microchannel heat exchanger design. Perform dynamic analysis to study the effect of geometry of the HX unit.

1.7 Scope

The organization of the chapters in this study is as follows:

Research background of refrigerant carbon dioxide, supercritical properties, and microchannels are reviewed in Chapter 2. A comprehensive literature review of heat transfer models for forced convection of supercritical fluids is given in this chapter as well.

The test facility, experimental procedure, and data analysis are examined in Chapter 3. The results of experimental investigation on heat transfer characteristics of supercritical carbon dioxide in microchannels are also presented in this chapter.

Chapter 4 presents the comparison between the experimental results and the current available correlations. New predicting model is proposed for heat transfer coefficient of supercritical gas cooling in microchannels.

Chapter 5 presents the experimental results for gas cooling heat transfer of Oil/ CO_2 mixture. Effects of oil type and oil concentration are investigated.

FEM-based mechanical design analysis of microchannel heat exchangers is presented in Chapter 6. Structural analysis, dynamic analysis, approximation tactics, and simulation model development are covered in this chapter. Experimental results are presented and compared with numerical simulation results. At the end of the chapter, a case study is given to evaluate the thermal and mechanical performance of heat exchanger design.

Finally, an overview of the conclusions and recommendations for future research is offered in Chapter 7.

CHAPTER 2

RESEARCH BACKGROUND

This chapter presents the extensive overview of prior investigations of the heat transfer characteristics in the supercritical region of CO_2 and its behavior in micro/mini channels.

2.1 Heat Transfer of Supercritical CO_2

2.1.1 Supercritical Fluid

Strictly speaking, a supercritical fluid is a fluid at pressures and temperatures higher than the critical pressure and critical temperature. A fluid that is at a pressure above the critical pressure but at a temperature below the critical temperature is considered to be a compressed fluid. However, in the present study, the term supercritical fluid will refer to a fluid that is at a pressure higher than the critical pressure, no matter what its temperature might be.

The thermo-physical properties of a gas at supercritical phase near the critical point are quite different from those at other phases. Taking the gas cooling process as an example, a phase change does not take place at supercritical pressure. However, the thermo-physical properties of the fluid do change drastically during the gas cooling process. Therefore, the heat transfer characteristics of gas cooling will be quite different from both those of condensation and those of a normal, single-phase cooling process. The thermo-physical properties of supercritical carbon dioxide (i.e., the specific heat, the

density, the conductivity, and the viscosity) are shown in Figures 2.1, 2.2, 2.3, and 2.4, respectively. As shown, the properties display extremely large variations near the pseudo-critical region.

2.1.2 Pseudo-Critical Temperature

In the supercritical region, the pseudo-critical temperature is defined as the temperature at which the corresponding specific isobaric heat capacity has the maximum value. The pseudo-critical region is very important since the thermo-physical properties of a supercritical fluid change drastically in this region.

In Figure 2.1, there are humps of specific heat near the pseudo-critical temperatures. The humps shift towards larger temperature values and become smoother as the absolute pressure increases. Some thermo-physical properties of carbon dioxide at pseudo-critical temperature are listed in Table 2.1.

This particular temperature point plays a very important role in heat transfer behavior because the specific heat capacity is directly related to the heat transfer coefficient. Usually, a higher specific heat will induce a higher heat transfer coefficient. But, near the pseudo-critical temperature, not only specific heat, but also density, conductivity, and viscosity have uneven values. Those uneven properties make the heat transfer characteristics much different from that of the normal, single-phase fluid.

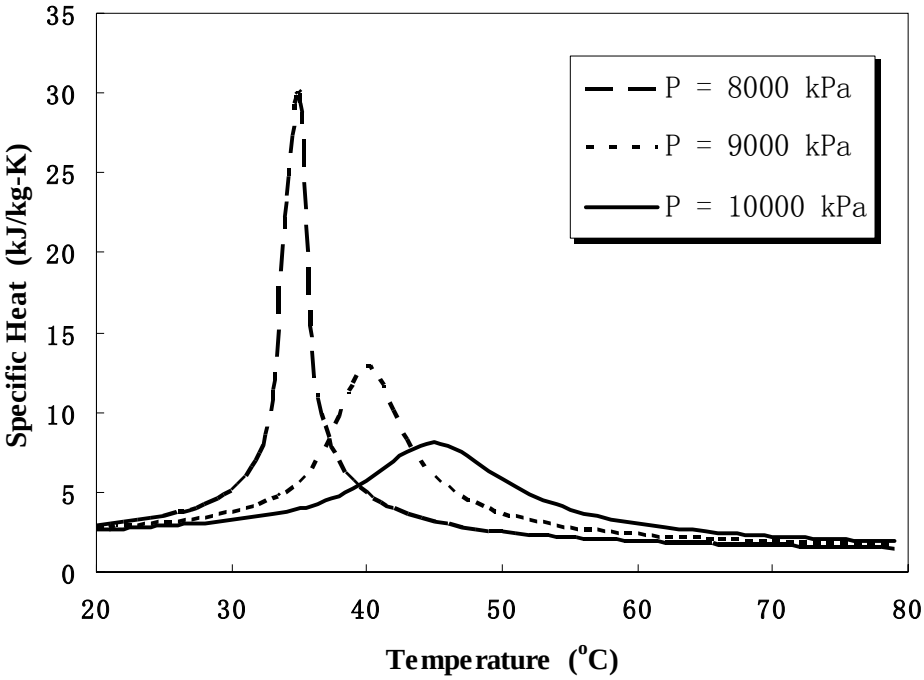

Figure 2.1. Specific heat versus temperature of supercritical CO_2

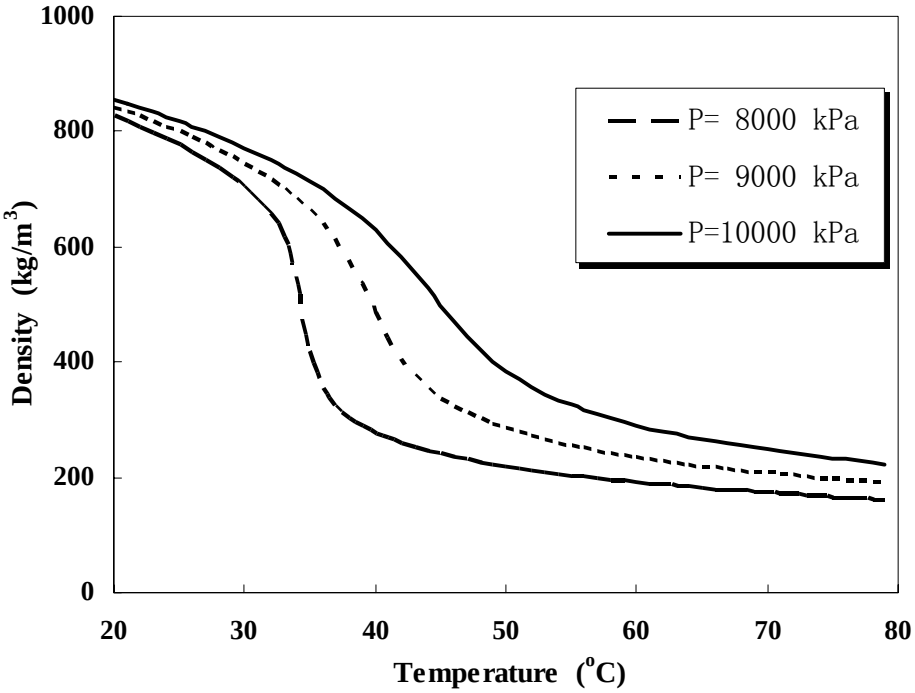

Figure 2.2. Density versus temperature of supercritical CO_2

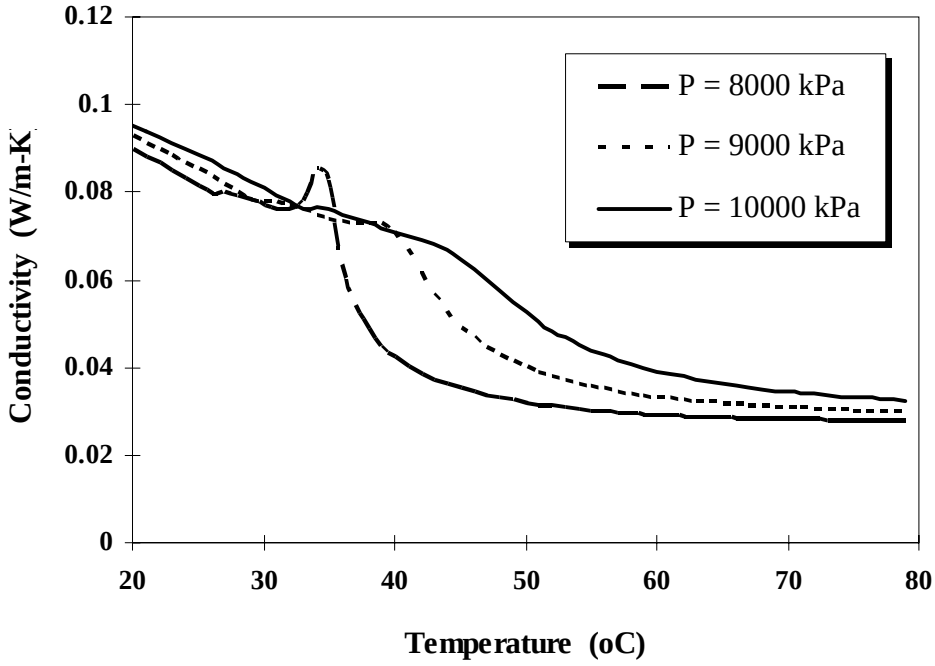

Figure 2.3. Conductivity versus temperature of supercritical CO_2

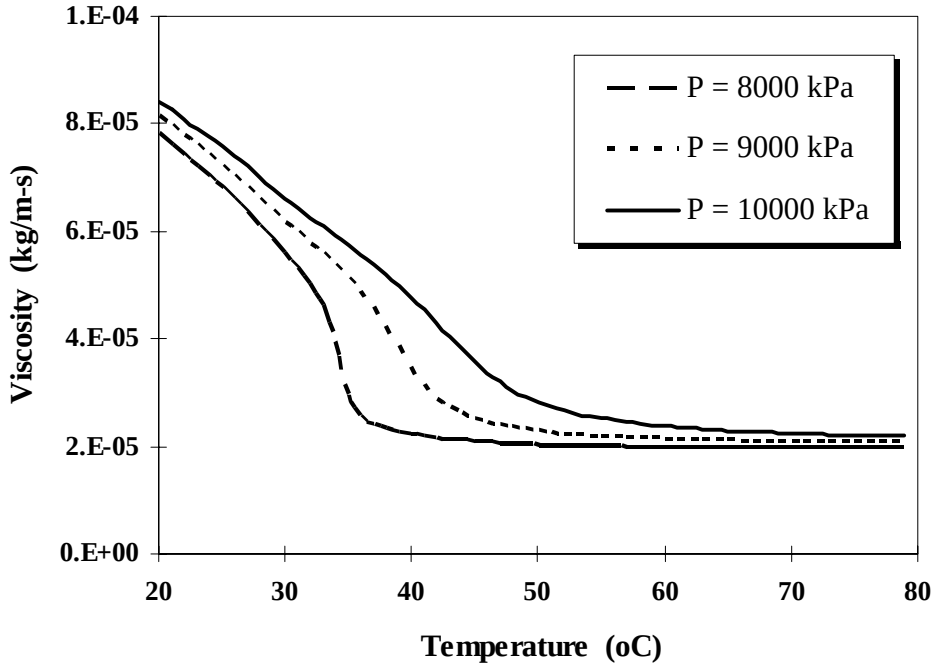

Figure 2.4. Viscosity versus temperature of supercritical CO_2

Table 2.1. CO_2 properties at pseudo-critical temperature

	8 MPa	9 MPa	10 MPa
T_pc (°C)	34.7	40	45
Cp (kJ/kg-K)	35.2	12.8	8.08
ρ (kg/m^3)	456	486	498
K (W/m-K)	0.08874	0.07081	0.06485
μ ($\times 10^{-6}$ kg/m-s)	32.2	34.6	35.8

2.1.3 Previous Studies on Heat Transfer of Supercritical CO_2

To match the temperature level in an ordinary heat pump or heating system, CO_2 has to work in the transcritical or supercritical region (critical point: 31.1°C / 73.8bar). In these regions, the thermodynamic and transport properties of CO_2 are quite different from those of conventional refrigerants, thus affecting the heat transfer and pressure drop characteristics accordingly.

A number of research projects on vapor compression systems using CO_2 as working fluid have been conducted or are underway. Bredesen et al. (1997) investigated flow boiling of CO_2 in a smooth tube. The test section was a 7 mm-diameter aluminum tube with direct heating. Based on their experimental results, Hwang et al. (1997) investigated the applicability of six commonly used empirical correlations for flow boiling reported by Chen (1966), Bennett-Chen (1980), Gungor-Winston (1987), Shah (1976), Schrock-Grossman (1959), and Liu-Winteron (1991). They also proposed a new empirical model, a modified Bennett-Chen's correlation, for CO_2 flow boiling in horizontal smooth tubes, which is claimed to be within a mean deviation of 14%.

Zhao et al. (1997) studied the boiling heat transfer characteristics of ammonia and CO_2 in horizontal smooth tubes. The test section was a tube with an inner diameter of 5.44 mm. The water-heating method was applied and the average heat transfer coefficient was determined. They also compared the typical values of the heat transfer coefficient of CO_2 with those for R-134a, R-12, and R-22, and found that the heat transfer coefficient of CO_2 is substantially higher.

Hwang et al. (1997) also investigated a few heat transfer correlations for forced convection near the critical region: Bring-Smith's correlation (1957), Petukhov's correlation (1961), and Ghajar-Asadi's correlation (1986). Based on the experimental data from Protopopov's group and Smith's group, a new empirical model, a modified Ghajar-Asadi's correlation, was proposed for CO_2 forced convection heat transfer near the critical region, which is claimed to be within a mean deviation of 11%.

Olson and Allen (1998) investigated the heat transfer characteristics of supercritical CO_2 in turbulent flow in a heated horizontal tube with 10.9 mm inner diameter. Operating pressure was varied from 7.8 MPa to 13.1 MPa. It was found that the measured Nusselt number agreed with the constant-property Petukhov-Gnielinski correlation for turbulent tube flow to within 6.6% at high-pressure operation. As the pressure was reduced toward the critical pressure, the measured Nusselt number diverged significantly from the constant-property correlation. They also found that at low pressure, the heat transfer coefficient increased with increasing mass flux/heat flux.

Zhao et al. (2001) studied the forced convection boiling heat transfer of CO_2 in microchannels. Tests were conducted in horizontal, triangular microchannels with a hydraulic diameter of 0.86 mm.

Pittersen et al. (2000) studied the gas cooling heat transfer & pressure drop of supercritical CO_2 in a microchannel tube (inner diameter of 0.8mm). It was found that the influence of the heat flux on heat transfer coefficient was rather small. The experimental data showed a low average deviation compared with Gnielinski's correlation. However, moderate deviation was also seen at high temperatures (deviation as much as 45% at pressure of 81bar and mass flux of 900 kg/m^2s).

Pitla et al. (2001) conducted experiments and numerical simulations for in-tube cooling of turbulent supercritical CO_2, which showed that supercritical CO_2 has excellent properties for operation in a gas cooler. A majority of the average heat-transfer coefficients predicted by the numerical model and the experimentally calculated ones were within 10% of each other. The tube inner diameter was 4.72mm.

Liao and Zhao (2002) investigated the heat transfer from supercritical CO_2 flowing in horizontal mini/micro circular tubes cooled at a constant temperature. Six circular tubes were tested with inner diameters of 0.5mm, 0.7mm, 1.1mm, 1.4mm, 1.55mm, and 2.16mm, respectively. Their experimental data deviated significantly from the existing correlations developed for large tubes. An empirical correlation was proposed based on their experimental data.

Yoon et al. (2003) presented the experimental data for the heat transfer and pressure drop characteristics obtained during the gas cooling process of carbon dioxide in a horizontal tube with an inner diameter of 7.73mm. The experimental results were compared with the existing correlations for the supercritical heat transfer coefficient, which generally under-predicted the measured data by up to 67%.

Huai et al. (2005) conducted the experimental study for the heat transfer of supercritical carbon dioxide in horizontal, multi-port mini channel under cooling conditions. The inner diameter was 1.31mm. The measured average heat transfer coefficients were compared with other literature, and a large discrepancy was observed. A new correlation was developed based on their experimental data.

Large discrepancies exist between the experimental data of these studies on supercritical CO_2 gas cooling. There is no single correlation that predicts all the data accurately for supercritical CO_2 in the gas cooling process, a knowledge gap this study will attempt to fill.

2.2 Heat Transfer in Microchannels

Heat transfer and fluid flow in microchannels have wide practical applications in highly specialized fields, such as bioengineering, micro-fabricated fluidic systems, and microelectronics. Lately, microchannels have been intensively used by the automotive air conditioning industry. They have almost completely replaced circular tubes in automotive condensers and have recently become the subject of study for automotive evaporators. Their advantages include an increased heat transfer surface area and a large surface-to-volume ratio, providing a much higher heat transfer rate. This feature allows heat exchangers to become compact and lightweight. In addition, microchannels can support high heat flux with small temperature gradients. These features have made microchannels essential for compact heat exchangers.

However, microchannels also have their weaknesses, such as large pressure drop, high cost of manufacture, dirt clogging, and flow mal-distribution, especially for two-phase flows. These problems are the focus of much of the research involving microchannels now.

The hydraulic diameters of microchannels are quite small, typically ranging from 1 μm to 2000 μm, and the fluid flow and heat transfer in microchannels are expected to be, in some cases, substantially different from those encountered in the normal-sized tubes and channels. There are many studies in heat transfer and fluid flow research for single-phase convection with microchannels. Zhao (2001) summarizes these studies in Table 2.1.

Table 2.2. Summary of studies on single-phase flow in microchannels (Zhao 2001)

Investigator	**Channel Geometry and Size (μm)**	**Reynolds Number, Fluid**	**Remarks**
Lancet, 1959	Gap: 580 to 640	8,000 - 40,000, air	• Experimental f is much larger than the correlation prediction value up to 100%
Gambill and Bundy, 1961	Rectangular channel D_h: 1910 – 2670	9,000 - 270,000, water	• Experimental f matches correlation prediction • Experimental Nu is only slightly smaller than correlation prediction
Wu and Little, 1983	Trapezoidal channel D_h: 56 – 83	100 - 15,000, N_2, H_2, Ar	• Friction factor depends on roughness • Critical Re decreases with increasing surface roughness (350 < Re < 900) • Experimental f is larger than correlation's prediction
Wu and Little, 1984	Trapezoidal channel D_h: 56 – 83	400 - 15,000, N_2	• Critical Re from 1000 to 3000 • Turbulent Nu higher than standard correlation prediction • Reynolds analogy not valid
Acosta, 1985	Rectangular channel D_h: 960 – 380	500 - 15,000, water	• Experimental f and Nu match correlation's prediction
Pfahler et al., 1991	Trapezoidal channel D_h : 0.96 – 39.7	0.0005 – 70	• Experimental f is slightly smaller than the prediction value (by less than 25%)
Choi et al., 1991	Circular channel D_h: 3 to 81.2	20 - 2500	• The critical Re for flow transition is 2300 • For both laminar and turbulent flows, real f is 25% smaller than correlation prediction • Experimental Nu is larger than that predicted by Dittus-Boelter correlation
Peng and Peterson, 1996	Rectangular channel D_h: 311 to 367	50 – 4000, water	• Critical Re in the range of 200 to 1500 • Flow transition occurs at smaller Re as the size of channel is decreased • Friction factor depends on the height-to-width ratio of the channel.
Wang and Peng, 1994	Rectangular channel D_h: 311 to 747	50 – 4000, water, methanol	• Experimental Nu is lower than that predicted by the Dittus-Boelter correlation • The critical Re is in the range of 1000 to 1500
Yang and Webb, 1996	Rectangular channel D_h: 1564 to 2637	2500 - 25,000, R-12, R-134a	• Experimental data agree with the predictions of the Petukhov correlation (within 10%)
Webb and Zhang, 1997	Rectangular channel D_h: 960 to 1310	5000 - 25,000, R-134a	• Experimental results match those predicted by the Petukhov and Dittus-Boelter correlations
Ravigururajan et al., 1996	Rectangular channel D_h = 425	4650 –3990, R-124	• The thinning of the boundary layer is the major contributor to high heat transfer coefficient. • Channel arrangement affects the heat transfer coefficient
Adams et al., 1998	Rectangular channel D_h: 760 to 1090	2600 - 23,000, water	• Experimental Nu is larger than that predicted by the Gnielinski correlation, and the deviation increases with increasing D_h and Re

2.3 Heat Exchangers – Thermal Design & Mechanical Design

Heat exchangers are devices that provide the flow of thermal energy between two or more fluids at different temperatures. Heat exchangers are used in a wide variety of applications. These include power production; process, chemical and food industries; electronics; environmental engineering; waste heat recovery; manufacturing; air-conditioning and refrigeration; and space applications. As is evident from this list, a large number of industries are engaged in designing various types of heat exchangers.

The thermal design of heat exchangers was developed decades ago. There is extensive literature on this subject (Kays and London 1984, Kuppan 2000, Kakac and Liu 2002). The majority of these studies have concentrated on developing correlations for heat transfer and flow friction in a variety of flow situations.

The numerical approach has also been frequently applied to the thermal design of heat exchangers (Smith 1997). As one of the numerical approaches, finite element method (FEM) is often used. Hamilton & Gopinath (2003) conducted a numerical study on a pin-fin array heat exchanger using finite element analysis (FEA). They found that the numerical model provided very accurate heat transfer predictions but overestimated the pressure drops.

Similar to thermal design, the mechanical design of heat exchangers has been under study for many years. Singh and Soler's 1984 book presents the fundamentals of the mechanical design on heat exchangers and pressure vessel components. The book covers the stress analysis on bolted flanges, boltless flanges, flat covers, heads, U-tubes, and expansion joints.

Many studies investigate the design and analysis of heat exchanger components. However, no previous study in the open literature has dealt with the systematic development of a model for such structural & dynamical designs. To analyze the structural dynamics of microchannel heat exchangers, an effective model has to be built with reasonable assumptions for structural and dynamical analysis.

2.4 Heat Transfer Models for Forced Convection of Supercritical CO_2

Since the thermophysical properties of supercritical fluids show uneven values and, even worse, change drastically near the pseudo-critical region, the conventional heat transfer correlations may not predict the heat transfer coefficient accurately. To better evaluate the performance of a CO_2 gas cooling heat exchanger, it is necessary to develop an accurate heat transfer correlation that is valid in the supercritical region. For this reason, in this section, several forced convection heat transfer correlations for supercritical fluids are investigated.

2.4.1 Gnielinski's Correlation

Gnielinski's correlation (Gnielinski 1976) has been widely used to predict the heat transfer coefficient for single-phase, forced convective, turbulent flow in a smooth single pipe/channel. Gnielinski's formula is given as:

$$Nu = \frac{(f/8)(\mathrm{Re}-1000)\,\mathrm{Pr}}{1.07+12.7\sqrt{f/8}\,(\mathrm{Pr}^{2/3}-1)} \qquad (2.1)$$

where the friction factor must be calculated from Petukhov's formula:

$$f = (0.790 \ln \mathrm{Re} - 1.64)^{-2} \qquad (2.2)$$

Gnielinski's correlation is valid for 0.5 < Pr < 2000 and 3000 < Re < 5× 10^6, given constant thermophysical properties.

2.4.2 Krasnoshchekov-Protopopov's Correlation

Considering the thermophysical properties of specific heat and density, Krasnoshchekov and Protopopov (1966) developed the following correlation for heat transfer near the critical region:

$$\boldsymbol{Nu_b} = \boldsymbol{Nu_b}' \left(\frac{\rho_w}{\rho_b} \right)^{0.3} \left(\frac{\overline{\boldsymbol{Cp}}}{\boldsymbol{Cp_b}} \right)^{\boldsymbol{b}} \qquad (2.3)$$

$$\overline{\boldsymbol{C}}\boldsymbol{p} = \left(\boldsymbol{H_b} - \boldsymbol{H_w} \right) / \left(\boldsymbol{T_b} - \boldsymbol{T_w} \right) \qquad (2.4)$$

where subscripts *b* and *w* represent the value evaluated at the bulk flow temperature and the wall temperature, respectively. *H* is enthalpy, $\overline{\boldsymbol{Cp}}$ is average integral specific heat, and $\boldsymbol{Nu_b}'$ is defined from Gnielinski's formula Equation (2.1).

For $\boldsymbol{T_w} / \boldsymbol{T_{pc}} \le 1$ or $\boldsymbol{T_b} / \boldsymbol{T_{pc}} \ge 1.2$, $b = 0.4$

For $1 \le \boldsymbol{T_w} / \boldsymbol{T_{pc}} \le 2.5$, $b = b_1 = 0.22 + 0.18\ (T_w / T_{pc})$

For $1 \le \boldsymbol{T_b} / \boldsymbol{T_{pc}} \le 1.2$, $b = b_1 + (5\ b_1 - 2)\ (1 - T_b / T_{pc})$

For $\boldsymbol{T_b} \le \boldsymbol{T_{pc}}$ and $\boldsymbol{T_b} / \boldsymbol{T_w} < 1$, $n = 0.7$

2.4.3 Petrov-Popov's Correlation

Petrov and Popov (1985) studied the local frictional resistance coefficient of inertia in the supercritical region and presented a new heat transfer correlation. The correlation combines the cooling condition of heat flux and the fluid properties of specific heat and density, as shown in Equation (2.5).

$$\boldsymbol{Nu} / \boldsymbol{Nu}' = \left(1 - \boldsymbol{m}\frac{\boldsymbol{q}}{\overline{\rho}}\right)\left(\frac{\overline{\boldsymbol{Cp}}}{\boldsymbol{Cp}}\right)^{\boldsymbol{n}} \qquad (2.5)$$

where

$$\boldsymbol{n} = \begin{cases} 0.66 - \boldsymbol{k}\left(\boldsymbol{q}/\overline{\rho}\right) & \textbf{\textit{when}} \quad \overline{\boldsymbol{Cp}}/\boldsymbol{Cp} \le 1 \\ 0.9 - \boldsymbol{k}\left(\boldsymbol{q}/\overline{\rho}\right) & \textbf{\textit{when}} \quad \overline{\boldsymbol{Cp}}/\boldsymbol{Cp} > 1 \end{cases}$$

m = 0.001 kg/J; $k = 4 \times 10^{-4}$ kg/J

The value of $\boldsymbol{q}/\overline{\rho}$ in this formula is given in J/kg. Nu' is the Nusselt number calculated at constant properties as Equation (2.1); and the average integral specific heat $\overline{\boldsymbol{Cp}}$ is defined as in Equation (2.4).

2.4.4 Ghajar-Asadi's Correlation

By comparing the existing empirical approaches for forced convective heat transfer in the near-critical region, Ghajar and Asadi (1986) suggested using the modified Dittus-Boelter-type heat transfer correlations while applying the property ratio method to account for large variations of physical properties in the near-critical region. The proposed formula is listed in Equation (2.5).

$$Nu_b = a\,\mathrm{Re}^b\,\mathrm{Pr}^c\left(\frac{\rho_w}{\rho_b}\right)^d\left(\frac{\overline{Cp}}{Cp_b}\right)^n \qquad (2.6)$$

where the average integral specific heat $\overline{Cp}$ is defined as in Equation (2.4), and *a*, *b*, *c* and *d* are curve-fitted constants. For *n*, the following criterion was used:

For $T < T_w \le T_{pc}$ and $T_w > T \ge 1.2\,T_{pc}$, $n = 0.4$

For $T \le T_{pc} < T_w$, $n = 0.4 + 0.2\,(T_w/T_{pc}-1)$

For $T_{pc} < T \le 1.2\,T_{pc}$ and $T < T_w$, $n = 0.4 + 0.2\,(T_w/T_{pc}-1)\,[1-5(T/T_{pc}-1)]$

2.4.5 Liao-Zhao's Correlation

Liao and Zhao (2002) conducted experiments on convection heat transfer of supercritical carbon dioxide in heated horizontal and vertical miniature tubes. They concluded that both the buoyancy effect and the heat flux, or temperature difference, between the bulk fluid and the wall must be taken into account for developing a heat transfer correlation in the supercritical region. Based on a least-square fit of 68 experimental data points for the circular tubes of d = 0.70, 1.40, and 2.16 mm, they obtained the following correlation for convection of supercritical CO_2 in miniature tubes heated at an approximately constant temperature:

$$Nu = 0.124\,\mathrm{Re}^{0.8}\,\mathrm{Pr}^{0.4}\left(\frac{Gr}{\mathrm{Re}^2}\right)^{0.203}\left(\frac{\rho_w}{\rho}\right)^{0.842}\left(\frac{\overline{Cp}}{Cp}\right)^{0.384} \qquad (2.7)$$

where *Gr* is the Grashof number of the bulk fluid. The average integral specific heat $\overline{Cp}$ was defined as in Equation (2.4).

2.4.6 Pitla et al's Correlation

Pitla et al (2002) performed both numerical and experimental study on the heat transfer during in-tube cooling of turbulent supercritical carbon dioxide. Using the obtained data as well as prior publications, the developed a new correlation to predict the heat transfer coefficient of supercritical carbon dioxide during in-tube cooling, as shown in Equation (2.8).

$$\boldsymbol{Nu} = \left(\frac{\boldsymbol{Nu}_{wall} + \boldsymbol{Nu}_{bulk}}{2} \right) \frac{\boldsymbol{k}_{wall}}{\boldsymbol{k}_{bulk}} \qquad (2.8)$$

where, the Gnielinski correlation Equation (2.1) is used to calculate both the Nusselt numbers Nu_{wall} and Nu_{bulk}. Subscript *wall* and *bulk* represent that the properties are evaluated at wall temperature and bulk flow temperature, respectively.

As seen, this correlation was based on mean Nusselt numbers that are calculated using the thermophysical properties at the wall and the bulk temperatures, respectively.

2.4.7 Yoon et al's Correlation

Based on their experimental data on gas cooling of supercritical carbon dioxide, Yoon et al (2003) suggested an empirical correlation using the form of Dittus-Boelter's correlation and multiplying the density ratio, as shown in Eq. (2.9):

$$\boldsymbol{Nu} = \boldsymbol{a}\,\mathrm{Re}^{\boldsymbol{b}}\,\mathrm{Pr}^{\boldsymbol{c}} \left(\frac{\rho_{\boldsymbol{pc}}}{\rho} \right)^{\boldsymbol{n}} \qquad (2.9)$$

$a = 0.14$, $b = 0.69$, $c = 0.66$, $n = 0$ for $\boldsymbol{T} > \boldsymbol{T}_{\boldsymbol{pc}}$

a = 0.013, b = 1.0, c = -0.05, n = 1.6 for $\boldsymbol{T} \le \boldsymbol{T}_{pc}$

In this correlation, only the effective of variance of density was considered.

2.4.8 Huai et al's Correlation

Based on their experimental data on gas cooling of supercritical carbon dioxide in multi-port mini channels, Huai et al (2005) proposed a correlation for heat transfer coefficient, as shown in Equation (2.10):

$$\boldsymbol{Nu} = 0.022186\,\mathrm{Re}^{0.8}\,\mathrm{Pr}^{0.3}\left(\frac{\rho_w}{\rho}\right)^{1.4652}\left(\frac{\overline{\boldsymbol{Cp}}}{\boldsymbol{Cp}_w}\right)^{0.0832} \qquad (2.10)$$

Again, the average integral specific heat $\overline{\boldsymbol{Cp}}$ is defined as in Equation (2.4), and the subscript w indicates the value measured at wall temperature.

The experimental data ranges are 8.5 $MPa \ge$ P $\ge$ 7.4 MPa, 53 °C $\ge$ T $\ge$ 22 °C, 419 $kg/m^2s \ge G \ge$ 114 kg/m^2s, and 9 $kW/m^2 \ge q \ge$ 0.8 kW/m^2.

In this correlation, the effect of variances in density and specific heat was considered.

2.5 Concluding Remarks

A brief review of the properties of carbon dioxide in the supercritical region was performed. In addition, an extensive overview of the prior research efforts that have been conducted to investigate heat transfer of supercritical carbon dioxide, heat transfer in

microchannels, and thermal design & mechanical design of heat exchangers was presented in this chapter.

The critical review of the related existing literature indicates that microchannel heat exchangers are more efficient than normal heat exchangers, and heat transfer coefficients of CO_2 are higher than those of fluorocarbons. However, the heat transfer experimental data of various studies of supercritical carbon dioxide show large discrepancies from each other. Even though some heat transfer correlation have been proposed in previous studies, no general agreement has been reached. Moreover, no previous work has been completed on the effect of oils on supercritical CO_2 heat transfer and pressure drops in gas cooling process. Therefore, comprehensive experiments relating to heat transfer characteristics of supercritical carbon dioxide will be highly valuable.

The overview of thermal & mechanical design of heat exchangers indicates that while the thermal design of heat exchangers is mature and comprehensive today, the mechanical design has mainly focused on the heat exchanger components. Therefore, the systematic development of a model scheme for structural & dynamical analysis will be valuable to provide a guide for the mechanical design of CO_2 heat exchangers.

CHAPTER 3

EXPERIMENTAL MEASUREMENTS OF HEAT TRANSFER AND PRESSURE DROP COEFFICIENTS FOR GAS COOLING OF SUPERCRITICAL CO_2 IN MICROCHANNELS

3.1 Instruction

From ozone depletion and global warming (ODP and GWP) viewpoints, natural refrigerants offer a clear advantage over CFCs and their substitutes. Ohadi and Mo (1997) have given a detailed analysis of selected properties of natural refrigerants. Recently, carbon dioxide (CO_2) has been investigated as an alternative for vapor compression systems. As a non-toxic and non-combustible gas, CO_2 offers ecological and personal safety. Furthermore, CO_2 is always available in sufficient quantities and is relatively inexpensive. However, the most important advantage of carbon dioxide is its attractive thermal characteristics. General physical and chemical properties of CO_2 and comparisons with those of other refrigerants are listed in Chapter 19 of the ASHRAE Handbook of Fundamentals (2005). Compared with R-134a, carbon dioxide has a lower liquid viscosity, which results in a smaller pressure drop when CO_2 flows in a tube or channel. And its larger refrigeration capacity makes carbon dioxide a competitive refrigerant.

To match the temperature levels in ordinary heat pump or heating systems, CO_2 has to work in the sub-critical or supercritical region (critical point: 31.1^{o}C / 73.8bar). In these regions, the thermodynamic and transport properties—in particular, the heat

transfer and pressure drop characteristics—of CO_2 are quite different from those of conventional refrigerants.

Heat transfer and fluid flow in microchannels have wide practical applications in highly specialized fields such as bioengineering, micro-fabricated fluidic systems, and microelectronics. Compared with normal-sized channels, microchannels have many heat transfer advantages. Since the microchannels have an increased heat transfer surface area and a large surface-to-volume ratio, they provide a high rate of heat transfer. Microchannel heat exchangers, therefore, can be compact and lightweight. However, microchannels also have weaknesses such as large pressure drops, and high cost of manufacture.

A number of research projects on vapor compression systems using CO_2 as the working fluid are in progress, as was documented in chapter 2 of this thesis. However, as indicated there, large discrepancies exist between experimental heat transfer data reported in the open literature. These discrepancies suggest the need for further experimental investigation of the gas cooling of supercritical CO_2. This chapter presents experimental gas cooling results of supercritical CO_2 in microchannels for a wide range of mass flux and pressure drop values.

3.2 Experimental Apparatus and Procedure

The facility used in the present experiments measures the average gas cooling heat transfer coefficient and pressure drops of supercritical CO_2 throughout the test

section. The test facility was designed to withstand up to 110 bar (1600psi) operating pressure.

The test rig was constructed mainly of stainless steel (low carbon 316 and 304 steel). It consisted of four main sections: (1) the test section; (2) the refrigeration loop; (3) the preheating loop and (4) the cooling water loop. A schematic diagram of the test facility is shown in Figure 3.1.

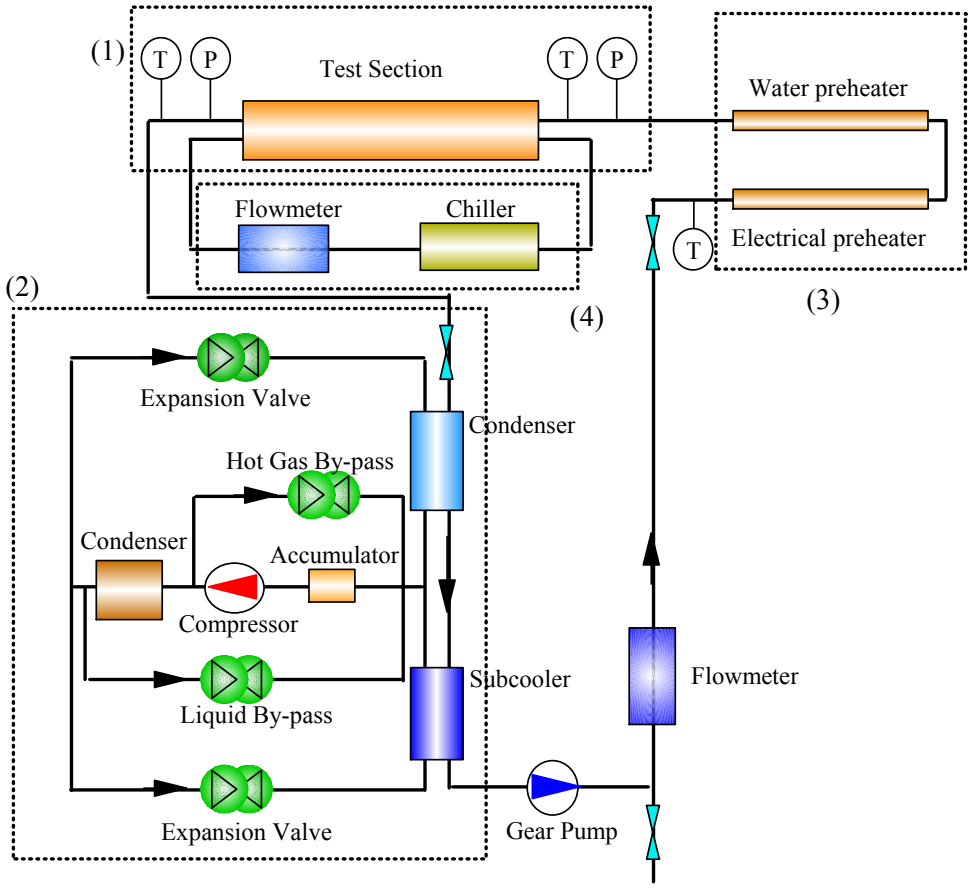

Figure 3.1. Schematics of experimental apparatus

CO_2 is circulated by a gear pump and passes through a mass flow meter, where its mass flow rate can be obtained directly. The advantage of the gear pump is that it does not require lubrication during operation. Therefore, the lubricant type and concentration will not affect the test results. In the pre-heater section, CO_2 is heated first by an electrical pre-heater, and then by a water-preheater to desired test conditions. Then CO_2 enters the test section, where heat exchange between CO_2 and the cooling water takes place. The inlet and outlet temperatures, the inlet pressure, and the pressure drop between inlet and outlet are measured directly. After the test section, CO_2 goes through the condenser and the sub-cooler to become subcooled liquid (or compressed fluid), and moves back to the gear pump. A chiller is utilized to circulate the cooling water through the test section and a volume flow meter, where the volume flow rate of water is measured.

The test section (area 1 of Figure 3.1) includes two microchannel tubes with a heat-exchange length of 635*mm*. Figure 3.2 presents the schematic geometry of the test section, which is a water-CO_2 counter-flow heat exchanger. Two aluminum microchannels tubes are soldered in headers on the both ends. The outside is a water jacket through which cooling water flows, while CO_2 remains inside the microchannel tubes.

Figure 3.3 shows the geometry details of the microchannel tube tested in the current experiments. The two identical tube slabs are made of aluminum, with 11 circular ports in each tube and a channel diameter of 0.79mm.

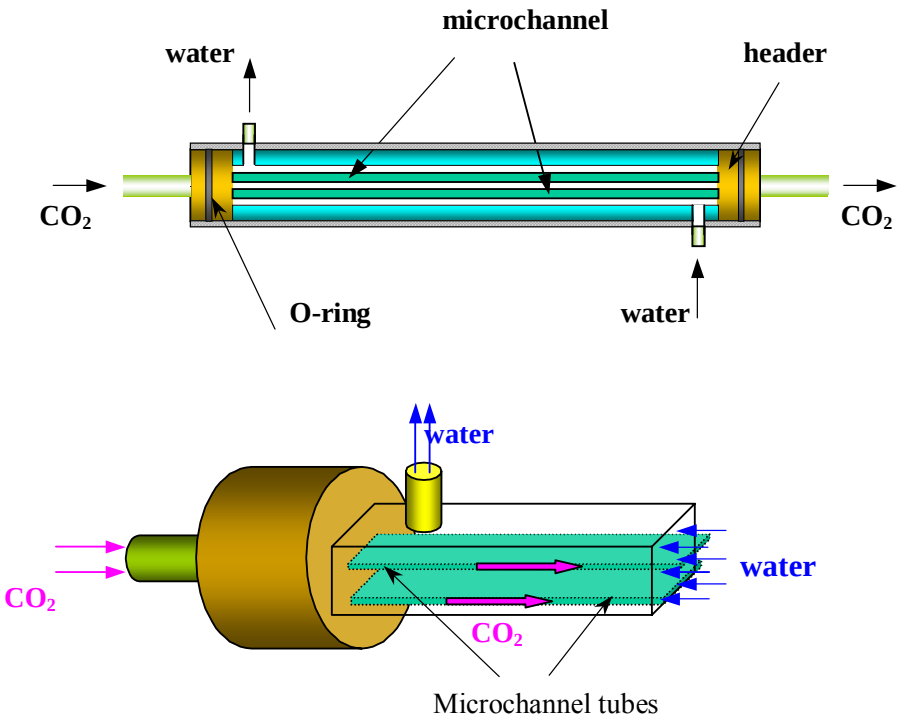

Figure 3.2. Schematics of the test section

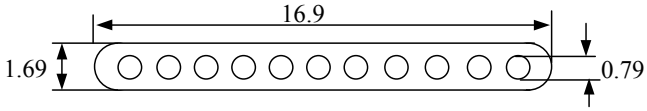

Figure 3.3. Cross section of microchannels tube (unit:*mm*)

The refrigeration loop (area 2 of Figure 3.1) consists of a compressor, a condenser, an accumulator, two thermal expansion valves, two heat exchangers (one that works as a condenser and the other as a sub-cooler for the CO_2), a hot gas by-pass, a liquid by-pass, and two pressure gauges. Adjusting the hot gas by-pass and liquid by-pass can compensate for the variations of the system pressure (suction and discharge pressures) due to variations in the cooling load. The refrigerant in the refrigeration loop is R-404a.

To reduce extraneous heat exchange with the environment, the refrigerant loop is covered with 50 *mm* of foam insulation (thermal conductivity 0.04 *W/m-K*).

The preheating loop (area 3 of Figure 3.1) consists of two parts: an electrical preheater and a water preheater. Subcooled refrigerant (or low temperature supercritical refrigerant) passes the electrical preheater first, where the refrigerant is evaporated into vapor (or heated to a high temperature fluid). Then the refrigerant gas goes through the water preheater, where it is heated to the desired temperature. Figure 3.4 demonstrates how the water preheater works. A pump is applied to circulate the water and an accumulator is used to store water and to collect any vapor.

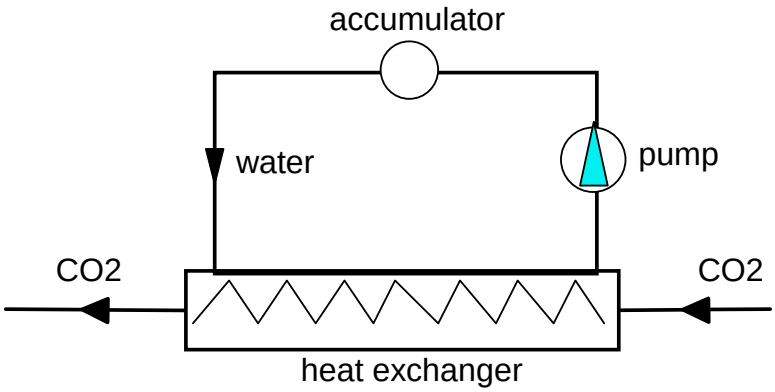

Figure 3.4. Schematic of water preheater

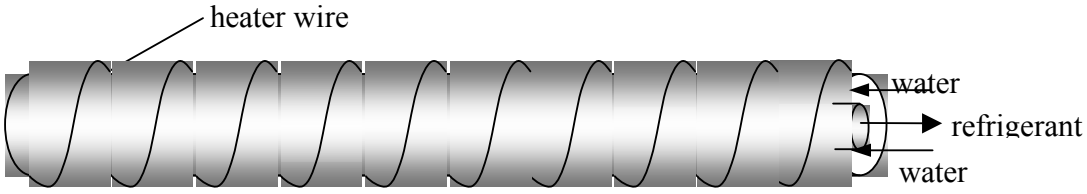

Figure 3.5. Heat exchanger in water preheater loop

Details of the heat exchanger in the water preheater loop are shown in Fig 3.5. Refrigerant flows through the inner tube, while the water is circulated in the annulus between the outer tube and the inner tube. The heater wire (D=0.8*mm*) is wrapped around the outer tube to heat the water. Thermal paste is applied to enhance the contact between the wire and the tube. The heated water is circulated to transfer the thermal energy to the refrigerant. Applying the water preheater ensures that the temperature of the refrigerant will never be higher than that of water.

The cooling water loop (area 4 of Figure 3.1) consists of a chiller and a water flowmeter. Cool water is provided by the chiller (Forma Scientific Inc.) with ± 0.1°C accuracy. A VFC flowmeter (Dwyer Instruments, Inc.) with a range of 0.1-1 GPM (±1% of full scale) measures the flow rate.

A Hewlett Packard (HP) data acquisition system makes it possible to trace the transient and steady behavior of the test unit. All outputs from the thermocouples and pressure transducers were connected to the HP multi-meter via an HP 34901A board. The data were recorded and displayed with HP Benchlink Data Logger software.

Several thermocouples (type T, Omega Engineering Inc.) were installed at the CO_2 inlet and outlet to measure the CO_2 temperature. The thermocouples were calibrated to within ±0.1 ℃ before assembling the test section.

The system's absolute pressure was measured at the inlet header of the test section by a 0 – 10 *MPa* pressure transducer (Setra Systems Inc.) with ±0.15% accuracy. A 0 –100 *kPa* differential pressure transducer (±0.5% accuracy) was employed to measure pressure drop along the test section. To reduce the extraneous heat exchange

with the environment, the test section was covered with 28 mm of foam insulation (thermal conductivity 0.04 *W/m-K*).

The flow rate of CO_2 was measured with a Coriolis mass flow meter (ABB K-Flow Inc.). The flow meter and the reading device were calibrated (within ±0.15%) before assembling the apparatus.

3.3 Data Reduction

3.3.1 Overall Heat Transfer Coefficient

The heat exchanged in the test section can be calculated based on the inlet and outlet conditions of the carbon dioxide:

$$Q = \dot{m} \cdot (H_{inlet} - H_{outlet}) \tag{3.1}$$

where H is the enthapy and $\dot{m}$ is mass flow rate.

On the other hand, utilizing the combined overall heat transfer coefficient U, the total exchanged heat amount Q can be written as:

$$Q = U \cdot A_1 \cdot \Delta T_{lm} \tag{3.2}$$

where U is the overall heat transfer coefficient based on the heat transfer surface on CO_2 side (A_1):

$$\frac{1}{U} = \frac{1}{h_1} + \frac{1}{h_2} \cdot \frac{A_1}{A_2} + R_w \tag{3.3}$$

where h is heat transfer coefficient, subscript *1* is CO_2, *2* is water, and A is the heat transfer surface area. The thermal resistance R_w in the tube wall is based on the CO_2-side heat transfer area.

The logarithmic mean temperature difference is defined as

$$\Delta T_{lm} = \frac{\Delta T_1 - \Delta T_2}{\ln(\Delta T_1 / \Delta T_2)} \tag{3.4}$$

with

$$\Delta T_1 = T_{1,in} - T_{2,out} \qquad \Delta T_2 = T_{1,out} - T_{2,in}$$

The validility of Equation (3.4) requires constant properties of both fluids and a constant overall heat transfer coefficient. But unfortunately, the properties of CO_2 vary widely along the test section in our test range, especially Cp .

Therefore, the following approch is applied to calculate the overall heat trasnfer coefficient U:

1) Divide the test section into N cells with equal heat exchanged ΔQ_i ;
2) Calculate the temperature profile of each fluid (water and CO_2) using inlet and outlet conditions (assuming the pressure drops linearly along the test section);
3) Calculate mean temperature difference $\overline{\Delta T_i}$ between water and CO_2 for each cell i ;
4) Also assume U is constant along the test section

The following relations can be wrriten based on the analysis above:

$$\Delta Q_i = U\,\Delta A_i\,\overline{\Delta T_i} \qquad i=1,2,3\ldots\ldots N \qquad (3.5)$$

$$\Delta Q_i = Q / N \qquad (3.6)$$

$$\sum \Delta A_i = A_1 \qquad (3.7)$$

There are *N+2* unknowns (ΔA_i, *U* and ΔQ_i) and *N+2* independent equations. The overall heat transfer coefficient *U* can be exactly calculated.

3.3.2 Waterside Heat Transfer Coefficient

From Equation (3.3), the water-side heat transfer coefficient h_2 has to be known to determine the heat transfer coefficient of CO_2 side h_1. Since the geometry of the cross-section of the water jacket is irregular and the water passage is narrow, current correlations cannot give a good approximation of the thermal resistance of the water. Therefore the modified Wilson plot method is employed to estimate the thermal resistance.

The Dittus-Boelter-type equation is a well-known expression for the single-phase heat transfer coefficient in a turbulent flow:

$$h_1 = C \cdot \mathrm{Re}^m \cdot \mathrm{Pr}^n \cdot \frac{k}{D_{hyd}} \qquad (3.8)$$

This equation can be used to describe the heat transfer coefficient on the CO_2 side if the CO_2 is in the liquid phase due to the almost constant thermodynamic properties. For this purpose, the Reynolds number exponent *m* and the constant *C* are assumed to be

unknown. The Prandtl number exponent n is commonly taken to be $n = 0.4$ for heating and $n = 1/3$ for cooling.

Combining (3.3) with (3.8) yields

$$\frac{1}{U} = \frac{1}{C} \cdot \left(\frac{1}{\mathrm{Re}^m \, \mathrm{Pr}^n \, k / D_{hyd}} \right)_1 + \left(\frac{1}{h_2} \cdot \frac{A_1}{A_2} + R_w \right) \qquad (3.9)$$

This equation has the form of

$$Y_1 = A \cdot X_1 + B \qquad (3.10)$$

where

$$X_1 = \frac{1}{\left(\mathrm{Re}^m \cdot \mathrm{Pr}^n \cdot \frac{k}{D_{hyd}} \right)_1} \qquad (3.11)$$

$$Y_1 = \frac{1}{U} \qquad (3.12)$$

$$A = \frac{1}{C} \qquad (3.13)$$

$$B = \frac{1}{h_2} \cdot \frac{A_1}{A_2} + R_w \qquad (3.14)$$

In Equation (3.12), the overall heat transfer coefficient U is known from experiments, since the exchanged heat, the heat transfer area and the mean temperature difference are obtained by measurement. Thus Y_1 is known.

The wall resistance R_w is rather small compared with the thermal resistance of the water side and the CO_2 side and it can be negelected in Equation (3.14).

In Equation (3.11), the Reynolds number *Re* and Prandtl number *Pr*, as well as the thermal conductivity *k* are known from measurement and the properties of liquid CO_2. As long as *m* is not known, X_1 stays unknown. During the experiments, the independent variable X_1 is controlled by changing the CO_2 mass flow rate. This corresponds to a variation of the Reynolds number. In one test series, *B* has to be maintained constant; i.e. h_2 has to be constant.

Applying experimental results, a linear curve in X_1-Y_1 coordinates will be obtained. From the plot, parameters *A* and *B* are determined by linear curve fitting; thus the constant *C* and the exponent *m* are calculated.

Unfortunately, it is impossible to solve a linear plot with more than two unknowns. Equation (3.10) actually includes three unknowns: h_2, *C* and *m*. The only solution is trial and error, as described below.

Equation (3.8) can be rearranged as

$$\left[\frac{1}{U} - B\right] \cdot \left(\mathrm{Pr}^n \, k / D_{hyd}\right)_1 = \frac{1}{C} \cdot \left(\frac{1}{\mathrm{Re}^m}\right)_1 \qquad (3.15)$$

or

$$Y_2 = D \cdot X_2 + E \qquad (3.16)$$

where

$$X_2 = \ln\left(\mathrm{Re}\right) \qquad (3.17)$$

$$Y_2 = \ln\left\{\left[\frac{1}{U} - B\right] \cdot \left(\mathrm{Pr}^{n}\ k / D_{hyd}\right)_1\right\} \qquad (3.18)$$

$$D = -m \qquad (3.19)$$

$$E = -\ln C \qquad (3.20)$$

Detailed steps for the *modified Wilson Plot method (trial and error)* are as follows:

1) Fix the water flow rate and conduct test series at various CO_2 flow rates for a given pressure while maintaining liquid status for the whole test section.
2) For each test, calculate the overall heat transfer coefficient U.
3) Guess a value for exponent m, and perform curve fitting for equation (3.10) to obtain B.
4) Perform another curve fitting for equation (3.16) with the value of B. The value of D is obtained from the curve fitting results.
5) Compare m with $-D$. If they don't equal each other, repeat steps (3) (4) and (5).
6) Stop when m equals $-D$.
7) Finally, the heat transfer coefficient of water side h_2 is calculated from equation (3.14).

In later experiments, the flow rate of water is kept constant to maintain a constant h_2. With heat transfer coefficient of water solved, the heat transfer coefficient of CO_2 can be determined from Equation (3.3).

The test results for the modified Wilson plot method are presented in Figure 3.6. The carbon dioxide was kept in liquid phase with pressure of 7 *MPa* all the time. The water flow rate stayed at 1 *GPM*, and the water temperature (inlet) was set as 25 °C (±1°C). The heat transfer coefficient of the water-side was calculated as h_2 = 2421 W/m^2-*K* with a flow rate of 1 *GPM* at 25°C for the test section geometry (Figure 3.2).

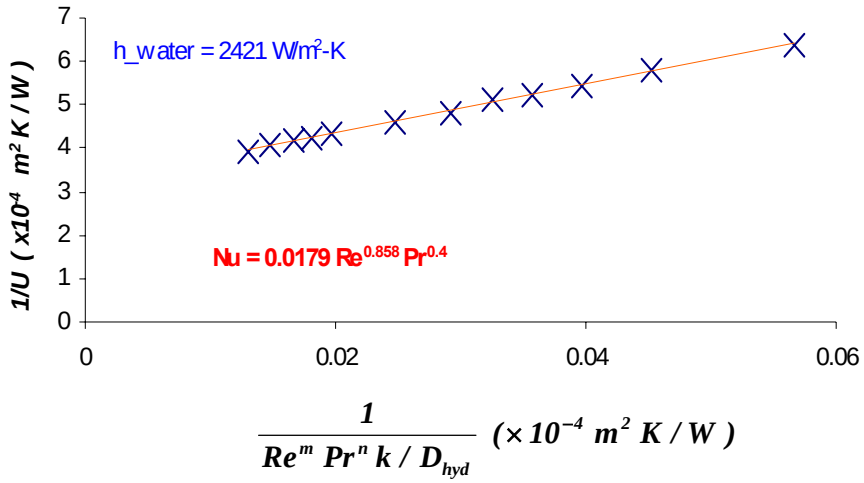

Figure 3.6. Wilson plot result for waterside heat transfer coefficient

3.4 Uncertainty Analysis

For a function y,

$$y = y(x_1, x_2, ..., x_n) \tag{3.21}$$

The uncertainty Δ_y can be calculated as the following:

$$\Delta_y = \sqrt{\left(\frac{\partial y}{\partial x_1}\Delta x_1\right)^2 + \left(\frac{\partial y}{\partial x_2}\Delta x_2\right)^2 + \ldots + \left(\frac{\partial y}{\partial x_n}\Delta x_n\right)^2} \qquad (3.22)$$

Neglecting the thermal resistance of tube wall R_w, Equation 3.3 can be re-arranged as:

$$Q \approx C_p \dot{m}\left(T_{in} - T_{out}\right) \qquad (3.23)$$

$$h_1 = \frac{1}{\frac{A_1}{Q}\Delta T_{lm} - \frac{1}{h_2}\frac{A_1}{A_2}} \qquad (3.24)$$

$$\frac{\delta Q}{Q} = \sqrt{\left(\frac{\delta \dot{m}}{\dot{m}}\right)^2 + \left(\frac{\delta(T_{in} - T_{out})}{T_{in} - T_{out}}\right)^2} \qquad (3.25)$$

$$\delta h_1 = \sqrt{\left(\frac{\partial h_1}{\partial Q}\delta Q\right)^2 + \left(\frac{\partial h_1}{\partial \Delta T_{lm}}\delta \Delta T_{lm}\right)^2 + \left(\frac{\partial h_1}{\partial h_2}\delta h_2\right)^2} \qquad (3.26)$$

By substituting Equation (3.24) into it, Equation (3.26) becomes:

$$\frac{\delta h_1}{h_1} = \sqrt{\left(\frac{h_1}{U}\frac{\delta Q}{Q}\right)^2 + \left(\frac{h_1}{U}\frac{\delta \Delta T_{lm}}{\Delta T_{lm}}\right)^2 + \left(\frac{h_1}{h_2}\frac{A_1}{A_2}\frac{\delta h_2}{h_2}\right)^2} \qquad (3.27)$$

From Equation (3.27), one may conclude that the uncertainty is almost proportional to the value of h_1. Apprently, larger h_1 will cause larger uncertainty.

During data reduction, uncertainty for every reported data is calculated based on the method described above. One sample uncertainty analysis is shown in Table 3.1.

Table 3.1. Sample uncertainty results

P=9MPa, G=560 kg/m^{2}s, h_1=5770 W/m^{2}K

Parameters	Normal Values	Uncertainty
T_{in} *(℃)*	47.9	±0.1
T_{out} *(℃)*	42.7	±0.1
m *(g/min)*	360	±10
Q (W)	215	±7
h_2 (W/m^{2}K)	2420	±40

Δh_1 = 865 W/m^{2}K

$\Delta h_1 / h_1 = \pm 15\%$

The largest uncertainty of the experimental data was 34.1%, with a heat transfer coefficient of *32759 W/m^2-K* and pressure of *8 MPa*. The second largest was 19.8%, with a heat transfer coefficient of *24338 W/m^2-K* and pressure of *9 MPa*. Thus, if the single experiment data with error of 34.1% is discarded, the uncertainty of the heat transfer coefficient is within 20% for all the remaining reported experimental data.

3.5 Results and Discussions

The main test series were conducted at pressures of 8, 9 and 10 *MPa* and for a mass flux range of 300 to 1,200 *kg/m^2-s*. The Reynolds number was varied from 4,000 to 40,000. The influence of CO_2 temperature was investigated in each test series. All the properties were evaluated at average temperatures and pressures along the test section.

The experimental data were chosen to cover the pseudo-critical temperature point. The temperature difference across the test section was around 5 ~ 10ºC.

Figure 3.7 shows a typical test region (circled) on the T-s diagram of CO_2. Dashed lines present the CO_2 critical pressure of 7377 *kPa*. In the present experiments, three different supercritical pressure levels of 8000 *kPa*, 9000 *kPa* and 10000 *kPa* were tested along the isobars. All the supercritical pressures were above the saturated line, and therefore no phase change occurred in the test section. Figure 3.8 shows the specific heat near the test region, with pseudo-critical temperature marked.

Some data points are incomplete due to some unexpected technical problems. To save time, the experimental series were not repeated. However, the missing data won't affect the trend of the curve, therefore won't change our conclusions.

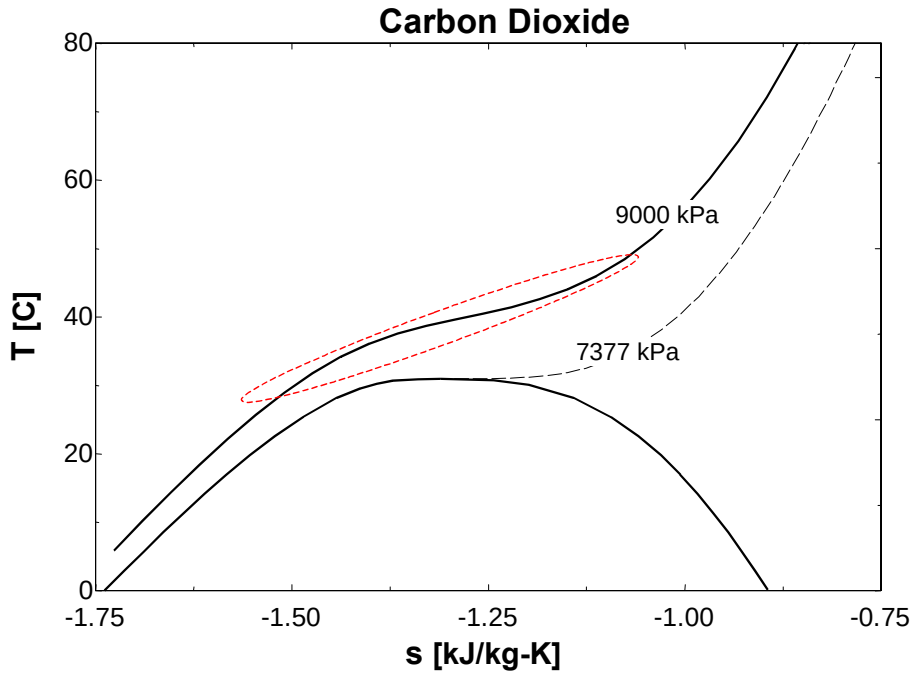

Figure 3.7. T-s diagram of carbon dioxide along test section

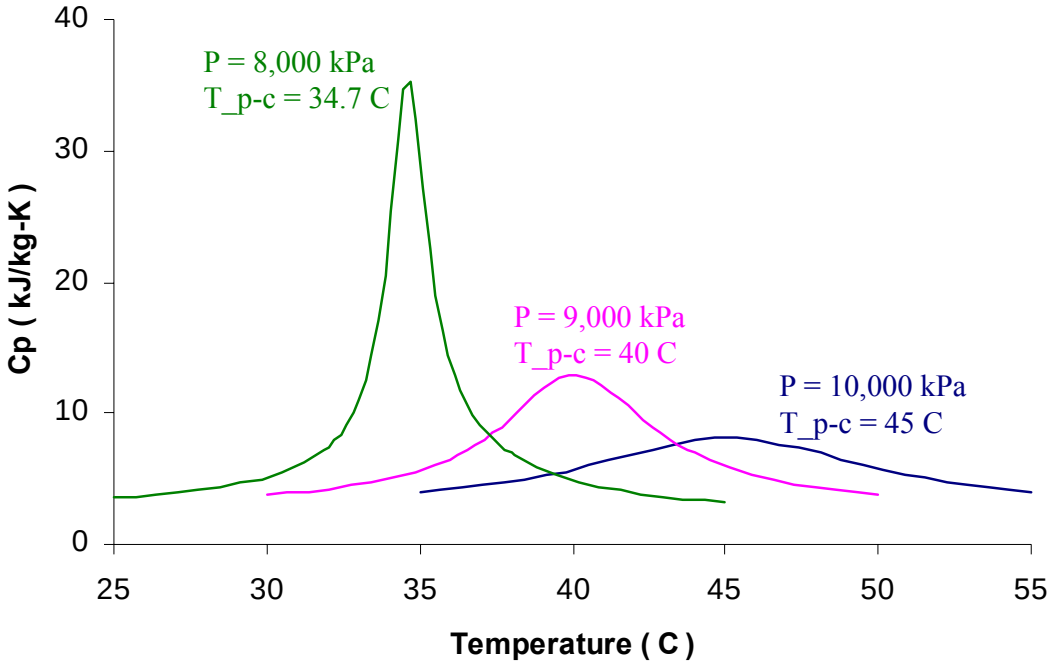

Figure 3.8. Specific heat and pseudo-critical temperature (T_p-c) of CO_2

3.5.1 Heat Transfer Coefficient

Pressure of 8 *MPa*. In this test series, with the pressure of the carbon dioxide fixed at 8 *MPa*, three different mass fluxes were tested. With a pseudo-critical temperature of 34.7 °C, the tested average temperature range was set from 25°C to 45°C. Figure 3.9 presents the experimental results of the heat transfer coefficient at a pressure of 8 *MPa*. The test data are shown as individual points in figure. As expected, the mass flux significantly influences the heat transfer coefficient. The larger the mass flux, the larger the heat transfer coefficients and vice versa.

As shown in Figure 3.9, the maximum heat transfer coefficient occurs near the pseudo-critical temperature (34.7 °C), where the specific heat is also at its maximum

value. The experimental data of the heat transfer coefficient show the same trend as the specific heat does in Figure 3.8.

Pressure of 9 *MPa*. Data for four different mass fluxes at pressure of 9 *MPa* are presented in Figure 3.10. With a pseudo-critical temperature of 40 °C, the tested average temperature range was set to vary between 30°C to 50°C. Again, the larger the mass flux, the larger the heat transfer coefficients, with the maximum values of heat transfer coefficient located near the pseudo-critical temperature.

Pressure of 10 *MPa*. Figure 3.11 depicts the heat transfer coefficient at a pressure of 10 *MPa* and for two different mass fluxes. With a pseudo-critical temperature of 45 °C, the tested average temperature range was set from 35°C to 55°C. As seen in Figure 3.11, the test results trends were similar to those of the specific heat trend depicted in Figure 3.8.

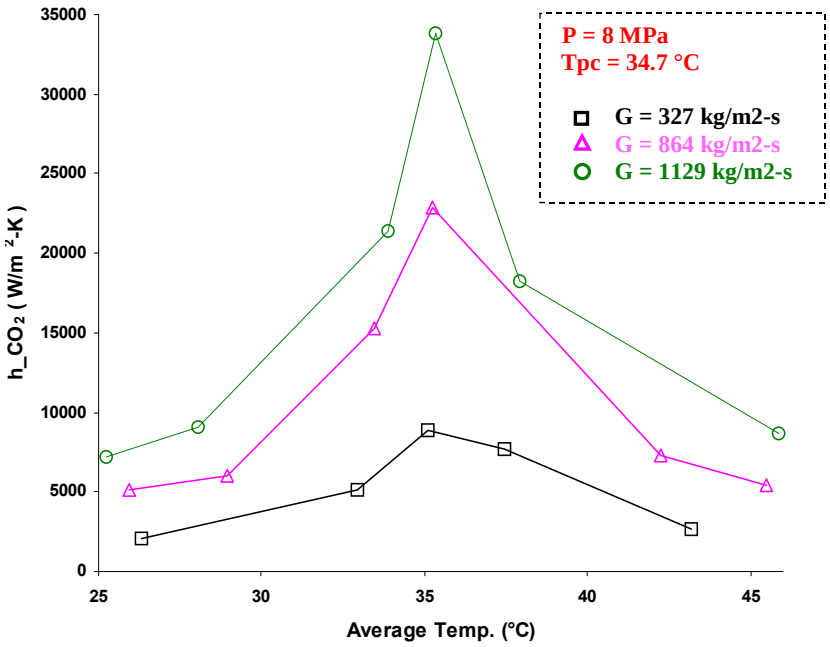

Figure 3.9. Heat transfer coefficient at 8 *MPa* with different mass fluxes

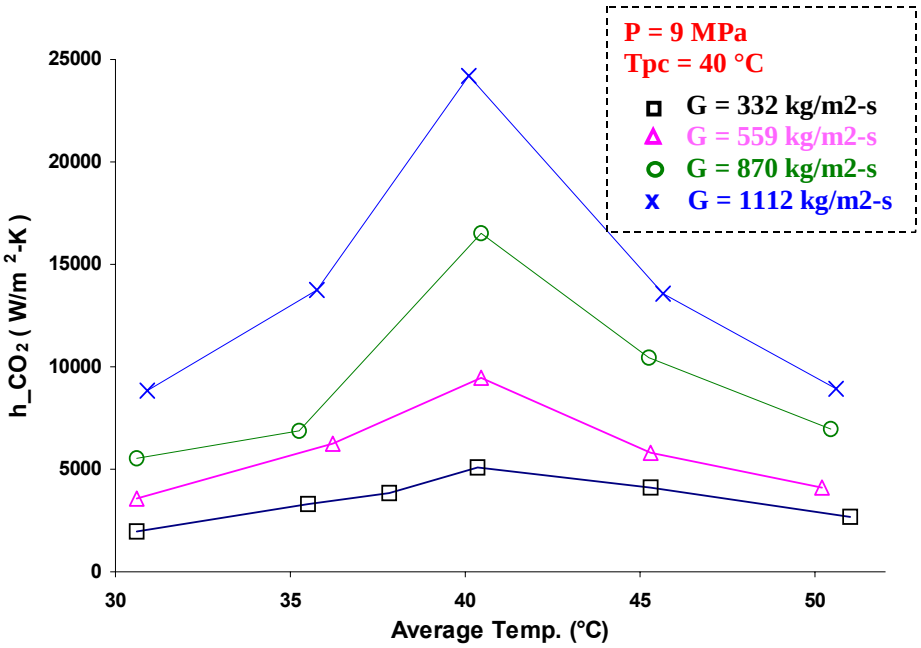

Figure 3.10. Heat transfer coefficient at 9 *MPa* with different mass fluxes

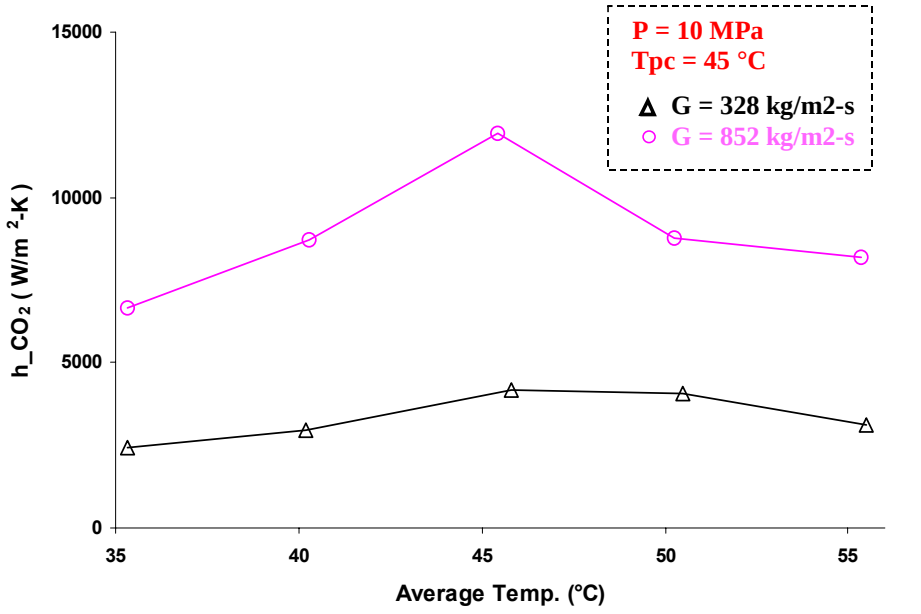

Figure 3.11. Heat transfer coefficient at 10 *MPa* with different mass fluxes

Pressure Influence. To better understand the influence of pressure on heat transfer coefficient, the experimental data were rearranged at the same mass flux instead of the same pressure. Figure 3.12 and Figure 3.13 present the heat transfer coefficient at mass fluxes of 332 kg/m^2-s and 870 kg/m^2-s, respectively, at three different pressures.

Compared the two figures (Figure 3.12 and Figure 3.13) with the figure depicting specific heat (Figure 3.8), similar trends can be seen. When the pressure increases, the peaks shift to higher temperatures, which is clearly due to the shift in pseudo-critical temperature. The peak value increases when the pressure is closer to critical pressure.

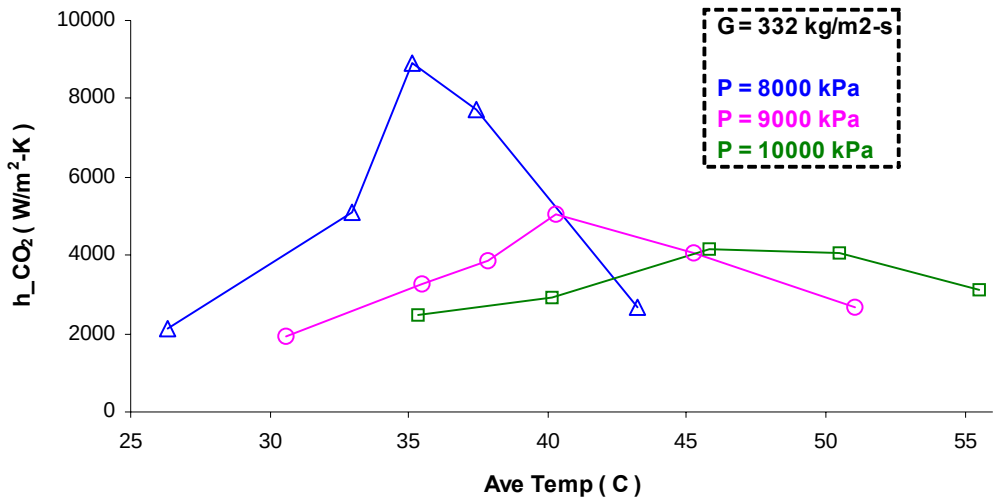

Figure 3.12. Heat transfer coefficient at 332 *kg/m2-s* with different pressure

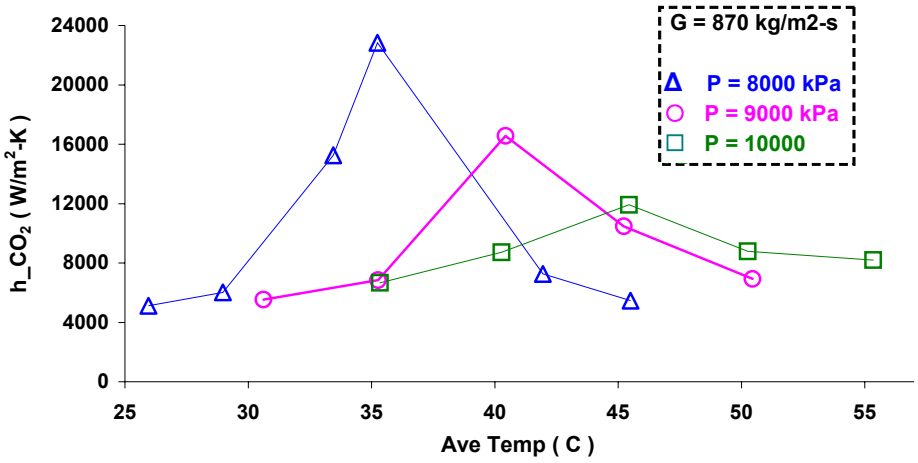

Figure 3.13. Heat transfer coefficient at 870 *kg/m2-s* with different pressure

3.5.2 Pressure Drop

Pressure drop were also measured in each experimental series. The results for pressure of 8 *MPa*, 9 *MPa*, and 10 *MPa* are shown in Figure 3.14, Figure 3.15, and Figure 3.16, respectively.

Considering pressure 9 *MPa* (Figure 3.15) as a typical case, the individual data points represent the experimental data, and the curves represent the calculation results based on Colebrook-White's correlation (1938). The roughness of the channel plays a role on the pressure drop coefficients. Greater roughness will cause additional pressure drop. In the calculation, the microchannel tubes were assumed to have a roughness of 3μm.

The Colebrook-White's correlation is given as an implicit form:

$$\frac{1}{\sqrt{f}} = -2\log\left(\frac{\varepsilon}{3.7D} + \frac{2.53}{\mathrm{Re}\sqrt{f}}\right) \qquad (3.26)$$

where *f* is the friction factor, ε is the roughness, *D* is the hydraulic diameter, and *Re* is Reynolds number.

As seen in the figure (Figure 3.15), the calculation results under-predicted the experimental data at the lower average temperature range region. The flow mal-distribution in the headers is believed to be at least partially responsible for the deviation between the experimental data and the correlation. Since the tested microchannel tubes were multi-port tube, the flow mal-distribution effect cannot be eliminated completely.

Furthermore, the viscosity of supercritical CO_2 has an uneven value at temperatures lower than its pseudo-critical temperature of 40°C, as shown in Figure 2.4. It stays almost constant when the temperature is higher than 40°C. Such viscosity properties partially explain why the correlation predicts the pressure drop well at temperatures higher than its pseudo-critical point, while it performs more poorly when the temperature is lower.

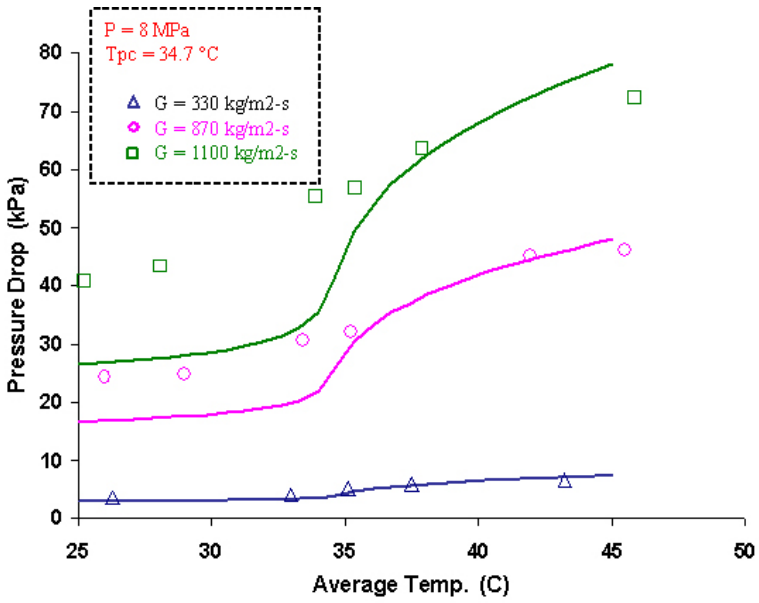

Figure 3.14. Pressure drop at 8 *MPa* with different mass fluxes

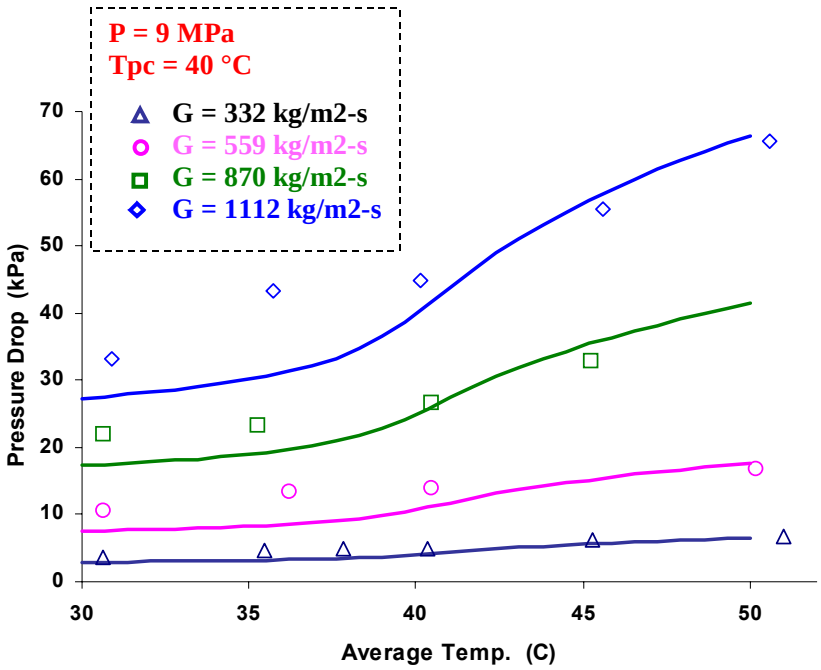

Figure 3.15. Pressure drop at 9 *MPa* with different mass fluxes

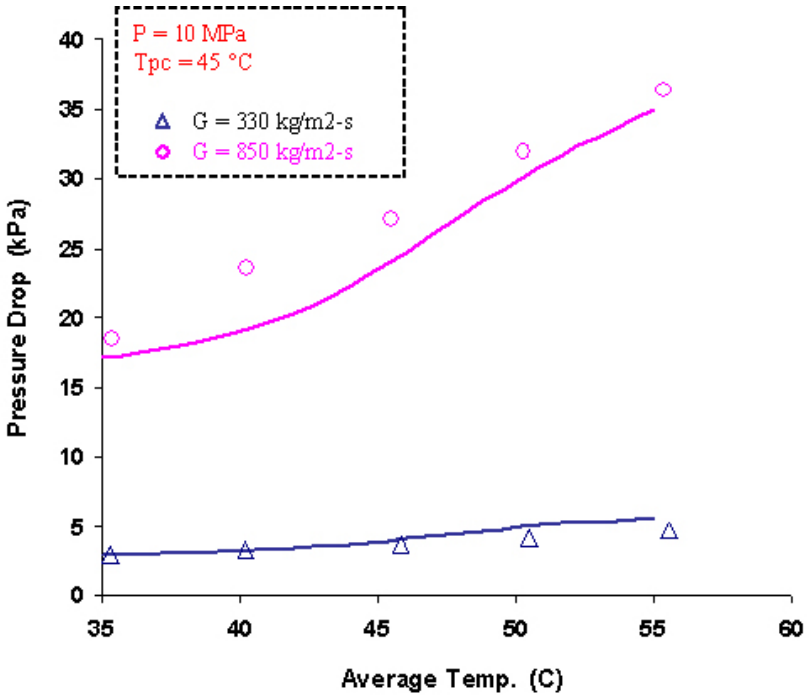

Figure 3.16. Pressure drop at 10 *MPa* with different mass fluxes

3.6 Conclusions

This chapter presented the results of an experimental study on gas cooling heat transfer coefficients and pressure drop of supercritical CO_2 in microchannel tubes. Experiments were conducted over mass fluxes ranging from 300 to 1,200 kg/m^2s, and for pressures ranging from 8 to 10 MPa. The experimental data were taken in the temperature region around pseudo-critical temperatures, where the values of thermal-physical properties are unique.

It was demonstrated that the mass flux has a significant influence on both the heat transfer coefficient and the pressure drop of supercritical CO_2. The larger the mass flux, the higher the heat transfer coefficient and pressure drop.

Heat transfer coefficients increase near pseudo-critical temperatures, mostly because of the large specific heat. When the pressure changes, the peak of the heat transfer coefficient shifts as the pseudo-critical temperature shifts. It was also found that the peak value increases when the pressure approaches its critical pressure.

The classic correlation predicted well the experimental data of the pressure drop in the high temperature region. Certain deviations were found at low temperatures, which can be attributed to the uneven value of viscosity at temperatures below the pseudo-critical point. The flow mal-distribution might also be responsible for these deviations.

CHAPTER 4

DEVELOPMENT OF EMPIRICAL CORRELATIONS FOR HEAT TRANSFER OF SUPERCRITICAL CO_2 IN MICROCHANNELS

This chapter focuses on developing empirical correlations to predict the gas cooling heat transfer coefficient of supercritical CO_2 in microchannels. The correlations are based on the available literature and the experimental results of the present study presented in Chapter 3.

4.1 Introduction

Due to the difficulty of dealing with the wide property variations of supercritical CO_2, satisfactory analytical methods have not been developed yet. Therefore, empirical generalized correlations based on experimental data are usually used to predict the heat transfer coefficient at supercritical pressure.

Since Bringer and Smith (1957), and Miropolskii and Shitsman (1957) proposed the Dittus-Boelter type correlation for supercritical water, studies have focused on how to integrate the effects of property variations into the correlation. Considering the thermophysical properties of specific heat and density, Ghajar and Asadi (1986) modified the Dittus-Boelter type correlation for heat transfer near the critical region. Krasnoshchekov and Protopopov (1966) proposed a correlation that adds the specific heat and density effect into Gnielinski's correlation. Liao and Zhao (2002) revised the Dittus-Boelter type correlation by adding the effect of specific heat, density, and the buoyancy

force. Pitla et al. (2002) developed a correlation that is based on mean Nusselt numbers that are calculated using the thermophysical properties at the wall and the bulk temperatures, respectively. Later, Yoon et al (2003) and Huai et al. (2005) proposed other modified Dittus-Boelter type correlations based on their own experimental data.

4.2 Comparison of Experimental Data and Existing Correlations

Gnielinski's correlation, Krasnoshchekov-Protopopov's correlation, Ghajar-Asadi's correlation, Pitla et al's correlation, and Huai et al's correlation were selected for comparison with the present experimental results for pure supercritical CO_2 gas cooling in microchannel tubes.

4.2.1 Gnielinski's Correlation

Gnielinski's correlation (Gnielinski, 1976) is valid for 0.5 < Pr < 2000 and 3000 < Re < 5×10^6, given constant thermophysical properties. The formula is given as:

$$Nu = \frac{(f/8)(\mathrm{Re}-1000)\,\mathrm{Pr}}{1.07+12.7\sqrt{f/8}\,(\mathrm{Pr}^{2/3}-1)} \qquad (4.1)$$

where the friction factor must be calculated from Petukhov's formula (Petukhov et al., 1961):

$$f = (0.790\ln \mathrm{Re} - 1.64)^{-2} \qquad (4.2)$$

Figure 4.1 shows a comparison of the results of the experimental data and Gnielinski's correlation at a pressure of 9 *MPa*. The individual data points are

experimental data, and the dash lines are calculation results based on Gnielinski's correlation. Different colors are relative to different mass fluxes.

As shown there, the correlation works well only at the lower mass flux regions and the region far from pseudo-critical temperature. At the high mass flux region, the correlation under-predicts the experimental data up to 54%, especially near the pseudo-critical temperature.

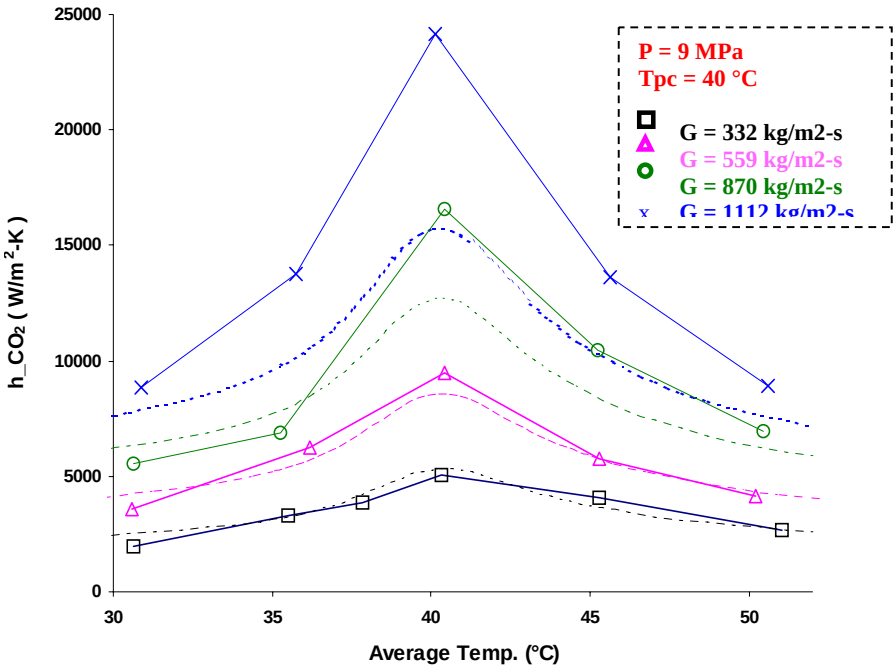

Figure 4.1. Comparison with Gnielinski's correlation

The current single-phase heat transfer coefficient correlations, such as Gnielinski's correlation, assume single-phase and flat thermodynamic properties. However, in the neighborhood region of pseudo-critical temperature, the thermodynamic properties of CO_2 do not qualify as the "flat" condition, as shown in Figures 2.1, 2.2, 2.3

and 2.4. The specific heat, as well as the density, has extremely uneven values in the region. This phenomenon explains why there is a larger deviation between experimental data and the correlation results in the region of pseudo-critical temperature.

4.2.2 Krasnoshchekov-Protopopov's Correlation

Krasnoshchekov-Protopopov's formula (Krasnoshchekov and Protopopov, 1966) is given as:

$$Nu_b = Nu_b' \left(\frac{\rho_w}{\rho_b} \right)^{0.3} \left(\frac{\overline{Cp}}{Cp_b} \right)^{0.4} \tag{4.3}$$

$$\overline{\boldsymbol{Cp}} = \left(\boldsymbol{H_b} - \boldsymbol{H_w} \right) / \left(\boldsymbol{T_b} - \boldsymbol{T_w} \right) \tag{4.4}$$

where subscript *b* and *w* present the value evaluated at the bulk flow temperature and the wall temperature, respectively. *H* is enthalpy. $\overline{\boldsymbol{Cp}}$ is called average integral specific heat, and $\boldsymbol{Nu_b}'$ is defined from Gnielinski's formula Equation (4.1).

Figure 4.2 shows the comparison between experimental data and Krasnoshchekov-Protopopov's correlation. Different colors are relative to different pressures. As shown, the experimental data match the correlation well at the region with low mass flux/heat transfer coefficient. But the correlation generally under-predicts the experimental data otherwise. The maximum deviation is up to 86%.

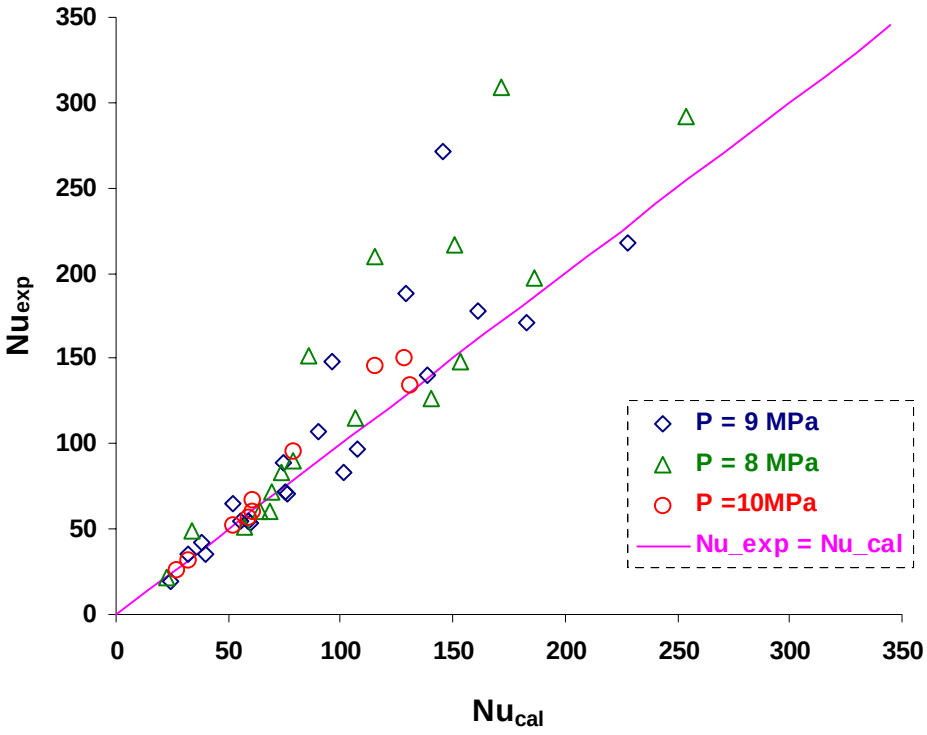

Figure 4.2. Comparison with Krasnoshchekov-Protopopov's correlation

4.2.3 Ghajar-Asadi's Correlation

Ghajar and Asadi (1986) proposed the following correlation for the heat transfer in the near-critical region:

$$Nu_b = a\,\mathrm{Re}^b\,\mathrm{Pr}^c\left(\frac{\rho_w}{\rho_b}\right)^d\left(\frac{\overline{Cp}}{Cp_b}\right)^n \qquad (4.5)$$

where the average integral specific heat $\overline{Cp}$ was defined as in Equation (4.4); *a*, *b*, *c* and *d* are curve-fitted constants; and *n* is suggested as a value of 0.4.

The results of the comparison between the experimental data and Ghajar- Asadi's formula and are shown in Figure 4.3. As shown, the deviation between the curve fitting

correlation and the experimental data is within 35% for majority of the data. The performance of the correlation is better than the Krasnoshchekov-Protopopov's correlation. But still, it does not accurate enough to predict the heat transfer coefficient.

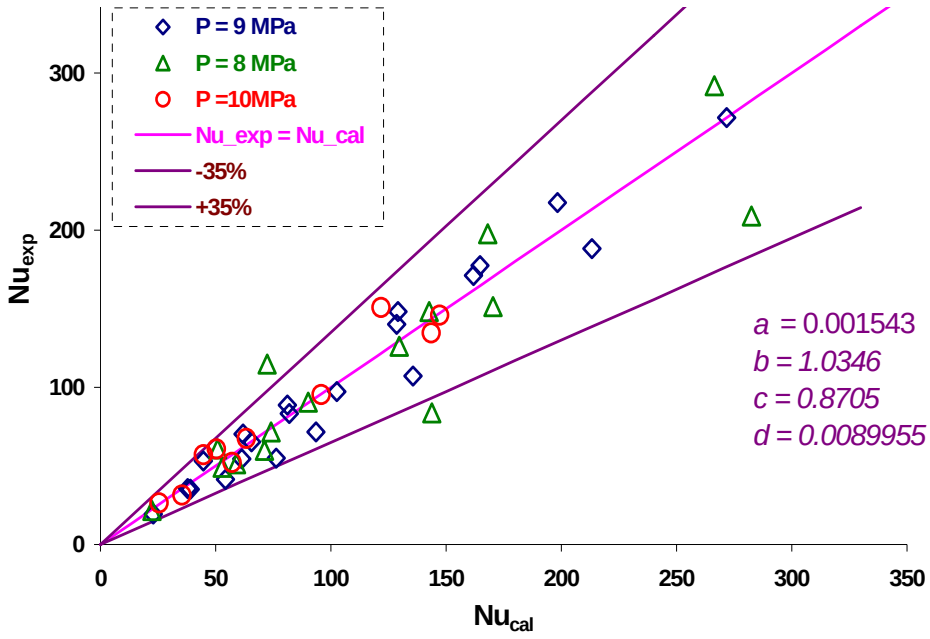

Figure 4.3. Comparison with Ghajar-Asadi's correlation

4.2.4 Pitla et al's Correlation

Pitla et al (2002) developed a new correlation to predict the heat transfer coefficient of supercritical carbon dioxide during in-tube cooling, as shown in Equation (4.6), below:

$$Nu = \left(\frac{Nu_{wall} + Nu_{bulk}}{2} \right) \frac{k_{wall}}{k_{bulk}} \qquad (4.6)$$

where Gnielinski's correlation Equation (4.1) is used to calculate both the Nusselt numbers Nu_{wall} and Nu_{bulk}. Subscript *wall* and *bulk* indicate that the thermophysical properties are evaluated at the wall temperature and bulk flow temperature, respectively.

Figure 4.4 shows the results of the comparison between experimental data and the Pitla et al's correlation. Different colors designate different pressure levels. Unlike Krasnoshchekov-Protopopov's correlation (Figure 4.2), the experimental data scatter both above and below the Pitla et al's correlation results. The deviation is up to 85%.

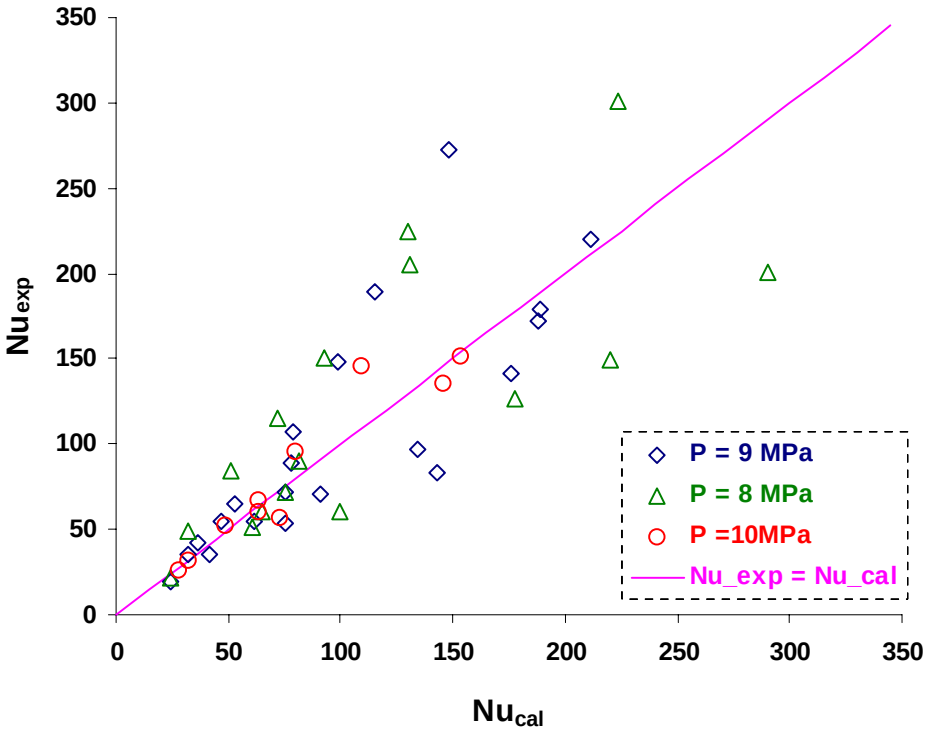

Figure 4.4. Comparison with Pitla et al's correlation

4.2.5 Huai et al's Correlation

Based on their experimental data on gas cooling of supercritical carbon dioxide in multi-port mini channels, Huai et al. (2005) proposed a correlation for heat transfer coefficient, as given by Equation (4.7), below:

$$Nu = 0.022186\,\mathrm{Re}^{0.8}\,\mathrm{Pr}^{0.3}\left(\frac{\rho_w}{\rho}\right)^{1.4652}\left(\frac{\overline{Cp}}{Cp_w}\right)^{0.0832} \qquad (4.7)$$

Again, the average integral specific heat $\overline{Cp}$ was defined as in Equation (4.4), and the subscript *w* indicates the value measured at wall temperature.

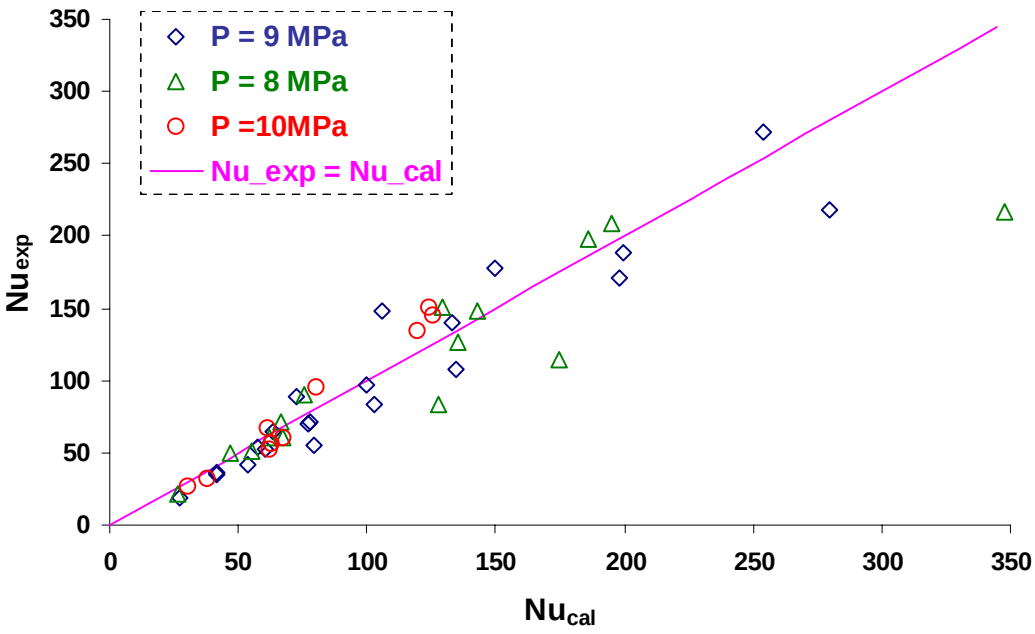

Figure 4.5. Comparison with Huai et al's correlation

Figure 4.5 shows results of the comparison between experimental data and Huai et al's correlation. As shown, Huai et al's correlation predicted 90% of experimental data within an error of 25%.

4.3 Proposed Correlation of the Present Study

When compared against the existing correlations, Ghajar-Asadi's curve-fitting method and Huai et al's formula were found to best predict the present experimental heat transfer data. As a matter of fact, Huai et al's formula is also based on a curve-fitting criterion. The difference between the two is the definition of the ratio of specific heat. Ghajar and Asadi defined the ratio as the average integral specific heat over the specific heat at bulk flow temperature, while Huai et al. defined the ratio as the average integral specific heat over the specific heat at wall temperature.

In Ghajar-Asadi's formula (Equation 4.5), two terms are added into the original Dittus-Boelter-type heat transfer correlations. One is the density ratio and the other is specific heat ratio. Generally, the density ratio can be considered as to account for the effect of density gradient and buoyancy. The specific heat ratio here may be considered to account for the effect of uneven specific heat along the cross section of the tube.

However, it may be more important to consider the effect of the uneven specific heat along the whole length of the tube. Based on such an assumption, the mean specific heat along the whole test section is defined as in the following:

$$\overline{Cp} = \left(H_{in} - H_{out}\right)/\left(T_{in} - T_{out}\right) \qquad (4.8)$$

With the modification of mean specific heat in Equation 4.8, a new correlation can be developed to predict the heat transfer coefficient at the supercritical region. Via curve-fitting, the formula is given as in the following:

$$Nu = 0.001546\,\mathrm{Re}^{1.054}\,\mathrm{Pr}^{0.653}\left(\frac{\rho_w}{\rho}\right)^{0.367}\left(\frac{\overline{Cp}}{Cp}\right)^{0.4} \qquad (4.9)$$

Figure 4.6 shows the curve-fitting results based on the present experimental data. As shown there, the proposed correlation predicts the experimental data much better than the previously reviewed correlations. Most (91%) of the data are within an error of 15%. The R-squared value here, also known as the coefficient of determination of the linear regression, is 97.94%.

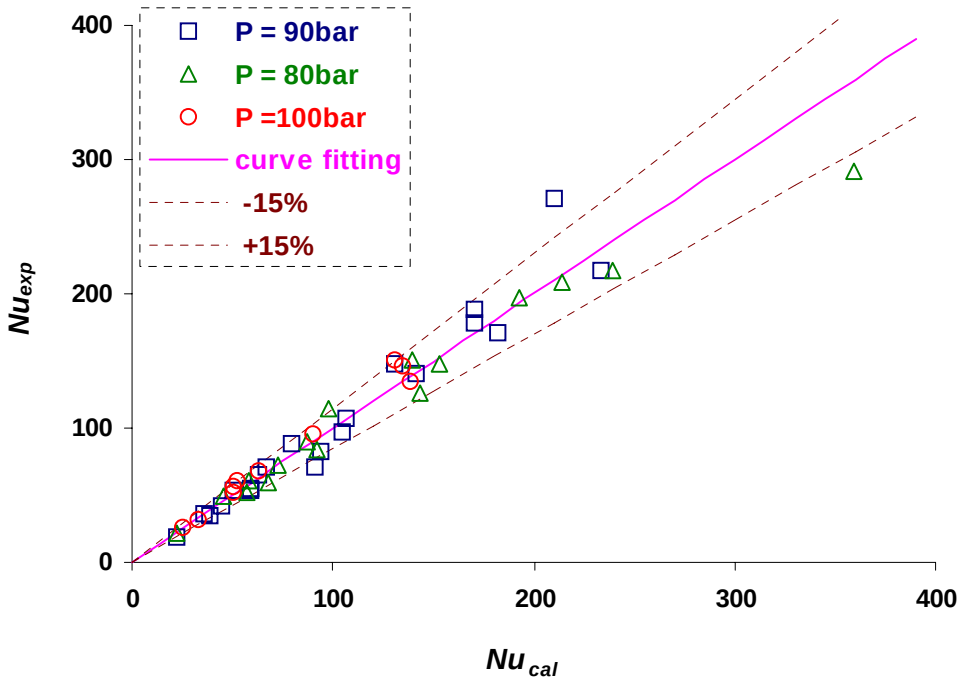

Figure 4.6. Curve-fitting for the proposed correlation

4.4 Conclusions

The present study compared five existing empirical models with the present study experimental results at the supercritical region for CO2 gas cooling. It was found that the conventional heat transfer correlation (Gnielinski's correlation) for forced convection in-tube flow failed to predict the experimental data near the pseudo-critical region, where the thermophysical properties have uneven values.

Both Krasnoshchekov-Protopopov's correlation and Pitla et al's correlation showed large deviations from the present experimental data, which may suggest that they are not valid for predicting the heat transfer of supercritical cooling in microchannel tubes.

Ghajar-Asadi correlation and Huai et al's correlation showed fair matches with the experimental data. The deviations were 35% and 25%, respectively. Both empirical models employed the curve-fitting method and the modified Dittus-Boelter-type heat transfer correlations.

In the present study, a new empirical correlation was proposed to predict the heat transfer of the supercritical gas cooling process in microchannel tubes. This new model is based on Ghajar-Asadi's correlation but redefines the average specific heat to account for the effect of fluctuation along the whole test section. The new model agrees very well with the experimental data, within an error of 15% for most (91%) of the experimental data.

CHAPTER 5

GAS COOLING OF SUPER CRITICAL CO_2 IN MICROCHANNELS IN THE PRESENCE OF LUBRICATING OIL

5.1 Introduction

In typical vapor compression systems, such as typical air conditioning (AC)/heat pump systems, oil is required to lubricate the compressors. When in operation, and over time, some oil leaves the compressor crankcase with the refrigerant. When this happens some of the oil will coat the inner surfaces of the heat exchanger (such as the condensers, evaporators, and internal heat exchangers) and thus reduces the rate of heat transfer, lowers the system's capacity and increases the pressure drop. Oil also reduces the volumetric capacity of the heat exchanger in that it reduces the amount of refrigerant by the amount of its own volume, and thus the unit must operate longer to pass the required amount of refrigerant through the heat exchanger. In addition, when oil in circulation is subjected to heat at the compressor and cold in the evaporator during repeated passages of circulation with contaminates, it forms carbon sludge, which is detrimental to all parts of the system.

During the start-up (30-40 seconds) of AC systems, often a compressor that has been in use for some while may lack sufficient oil due to a potential large amount of oil having left the compressor with the refrigerant. In order to prevent inadequate lubrication, it is common practice to pre-fill the compressor with an extra quantity of oil. But this excess oil adversely affects both system performance and energy efficiency. The presence

of oil inside a system drastically increases the flow resistance and thus results in higher compressor work and lower COP. The overall effect of oil in circulation is to lower the efficiency of the unit and thereby to require additional running time and thus added operating costs.

The behavior of such oil-refrigerant mixtures differs from that of pure refrigerant in heat transfer and pressure drop coefficient. When it comes to microchannel heat exchangers, such differences are more significant. Numerous studies in the past have addressed the effect of oil on CFC/HCFC refrigerant/oil mixtures with plain and microfin tubes. A number of papers have also considered the effect of oil on boiling heat transfer. However, no previous work has addressed the effect of oil on heat transfer and pressure drops of supercritical CO_2.

In the present study, efforts were focused on investigating the influence of oil(s) on the gas cooling heat transfer characteristics of supercritical CO_2 in microchannels. Different oils, both miscible and immiscible, were studied as a function of such operational conditions as oil concentration and temperature. Tests were conducted in a horizontal circular microchannel tube with a hydraulic diameter of 0.79 *mm*.

5.2 Experimental Apparatus and Procedure

The facility used previously for pure supercritical CO_2 (Chapter 3, Figure 3.1) was used in the present oil mixture experiments as well. The only change was in the test section, which had suffered corrosion damage. Therefore, a new test section was built, as shown in Figure 5.1.

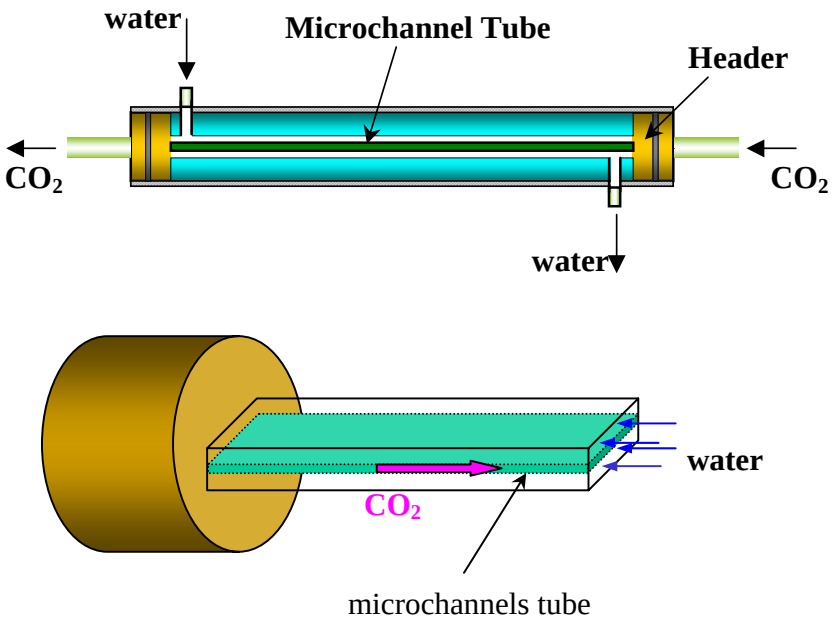

Figure 5.1. Test section for oil mixture tests

As shown, the new test section had only one microchannel tube slab, since small mass flux was not tested; this design avoids possible contact between the two microchannel tube slabs. The wall of the water jacket was fluted to enhance the turbulence in the water flow. The tube was the same as before: it was made of aluminum with 11 circular ports each with inner diameter of 0.79 *mm*, thickness of 1.69 *mm*, width of 16.9 *mm* and length of 635 *mm*, as was shown in Figure 3.3.

To run the oil mixture tests, a certain amount of oil was pre-charged into the vacuumed test loop first, followed by the refrigerant CO_2. The mixture percentage (oil concentration) was based on the weight of the charged oil/CO_2. After cycling for a certain amount of time, the oil and CO_2 were assumed to be well mixed. To reduce the extraneous heat exchange with the environment, the test section was covered by foam insulation (thermal conductivity 0.04 *W/m/K*) with thickness of 28 *mm*.

5.3 Data Analysis

With the new test section, the water passage was changed as well. To determine the thermal resistance at the water-side, a series of experimental tests was conducted again based on the modified Wilson plot method, which was demonstrated in Chapter 3.3.2. The heat transfer coefficient of the water-side was calculated as h_2 = 4891 W/m^2-K with a flow rate of 1 *GPM* at 25°C for the new test section geometry (Figure 5.1). All the properties were evaluated at the bulk temperature, assuming 100% of the refrigerant CO_2.

5.4 Results and Discussions

One of objective of the present work is to study the effect of oil addition on heat transfer coefficient and pressure drop in the CO2 supercritical gas cooling process in microchannels. The effect of the oil type is also addressed.

Three types of oil were tested with CO_2 in the supercritical region of CO_2. Two of them are immiscible oils and one is miscible. The test conditions were set at pressure of 9 *MPa* (90 *bar*, around 1300 *psi*) and mass flux of 890 kg/m^2-*s*. The pseudo-critical temperature at 9 *MPa* is 40 ºC. The experimental data were chosen in the temperature region between 30 ºC and 50 ºC so that they covered the pseudo-critical temperature point. The temperature difference across the test section was around 5 ~ 10ºC. The influence of CO_2 temperature was investigated for different oil concentrations. All the properties were evaluated at average temperature and pressure along the test section.

5.4.1 PAG/AN Oil

In the section, the effect of PAG/AN oil is studied. This oil mixture is immiscible with the refrigerant CO_2. Two oil concentrations (2% and 5% in weight) were tested. Figure 5.2 shows the heat transfer coefficient results for PAG/AN oil addition cases compared with the case of pure CO_2 (0% oil). In Figure 5.2, the circular data points represent the pure CO_2 case, the triangular points represent 2% oil addition and the rectangular points represent 5% oil addition. The hunchbacks of the heat transfer coefficient curves are mainly due to the change of the specific heat as temperature changed, as discussed in Chapter 3.

As we can see, the addition of immiscible oil PAG/AN substantially reduces the heat transfer effect. At pseudo-critical temperature, where the peak value of heat transfer coefficient appears, the heat transfer coefficient was reduced by 12% for 2% oil addition and by 32% for 5% oil addition.

Figure 5.3 shows the pressure drop results for 5% oil addition. The rectangular data represent 5% oil addition data and the solid line represents the case of pure CO_2. As shown in the figure, pressure drop dramatically increases by up to 49% for 5% oil addition.

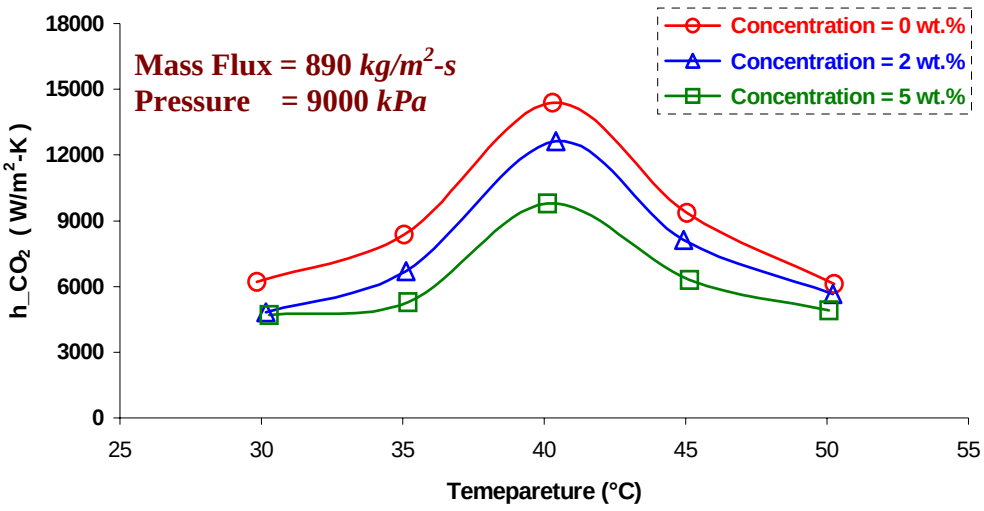

Figure 5.2. Heat transfer coefficient (PAG/AN oil addition)

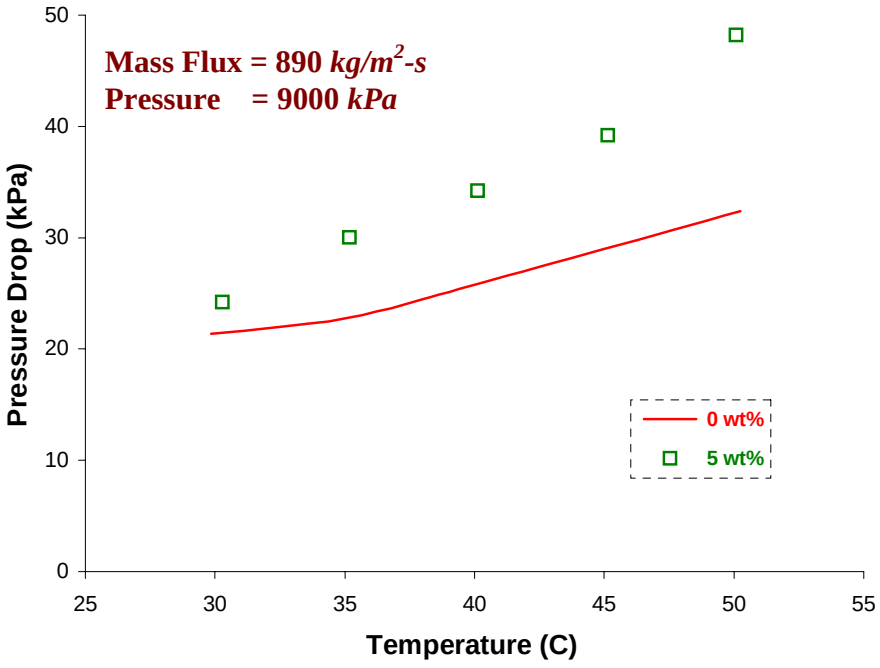

Figure 5.3. Pressure drop (PAG/AN oil addition)

5.4.2 PAG Oil

In this section, the effect of PAG (Polyalkylenglycol) oil on heat transfer and pressure drop coefficients is studied. This oil is also immiscible with refrigerant CO_2. Four different oil concentrations (1%, 2%, 3% and 5% in weight) were tested. Figure 5.4 shows the heat transfer coefficient results for PAG oil addition cases compared with the case of pure CO_2 (0%). In Figure 5.4, the circular data represent pure the CO_2 case, the diamond data correspond to 1% oil addition, the triangular data correspond to 2%, the star data correspond to 3%, and the rectangular data represent 5%. Again, any oil addition will weaken the heat transfer capacity. As shown in the figure, the more oil, the lower the heat transfer coefficient. The heat transfer coefficient was reduced by up to 57% for 5% oil addition.

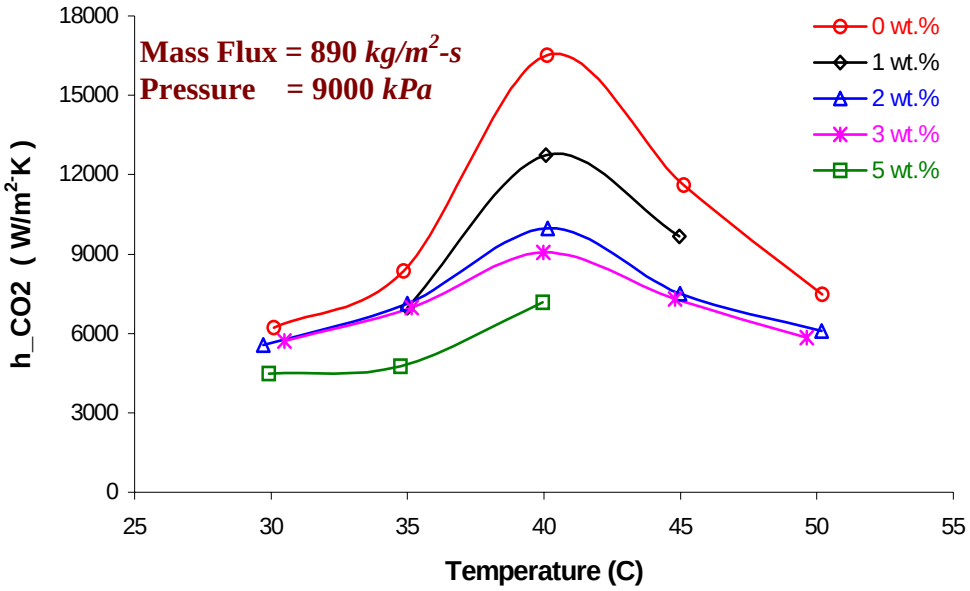

Figure 5.4. Heat transfer coefficient (PAG oil addition)

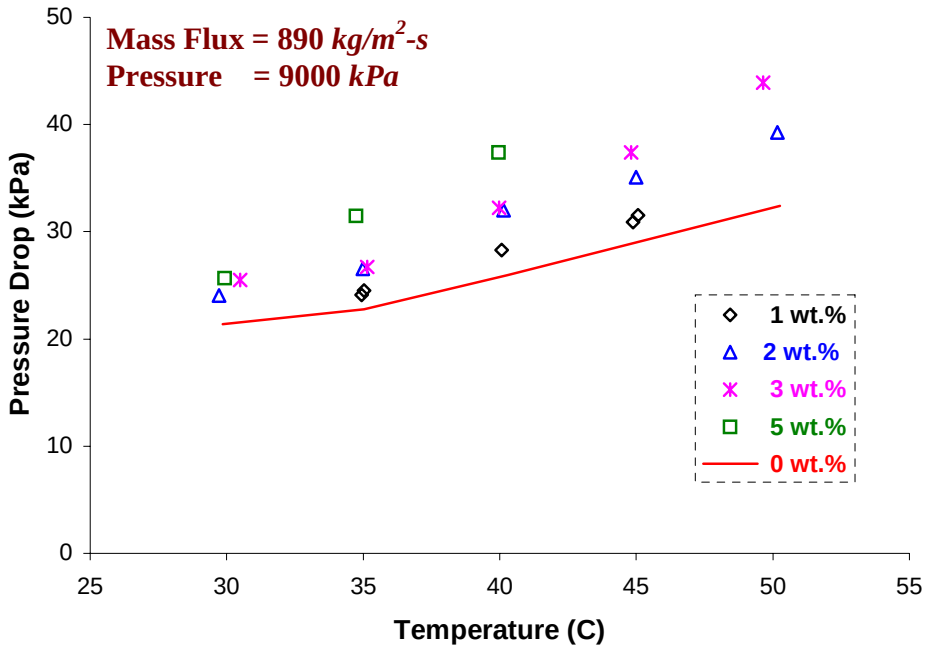

Figure 5.5. Pressure drop (PAG oil addition)

Figure 5.5 shows the pressure drop results. The solid line represents the pure CO2 gas case. As shown, additional oil causes higher pressure drop. Pressure drop can increase by up to 44% for 5% PAG oil addition. Some data points are incomplete due to some unexpected technical problems. To save time, the experimental series were not repeated. However, the missing data won't affect the trend of the curve, therefore won't change our conclusions.

5.4.3 POE Oil

In this section, the effect of POE (Polyolester) oil is studied. Unlike the previous two oils PAG/AN and PAG, this oil is miscible with refrigerant CO_2.

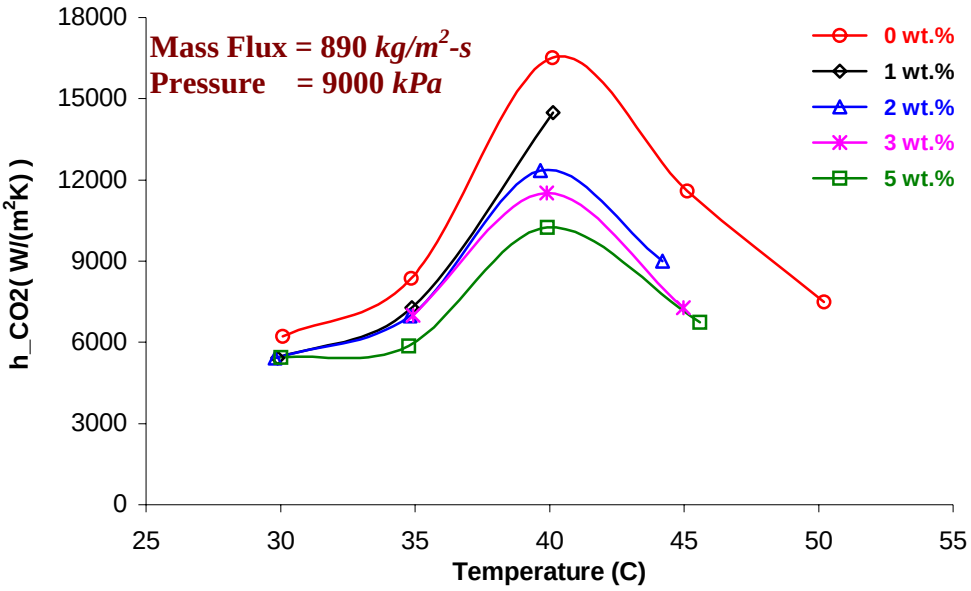

Figure 5.6. Heat transfer coefficient (POE oil addition)

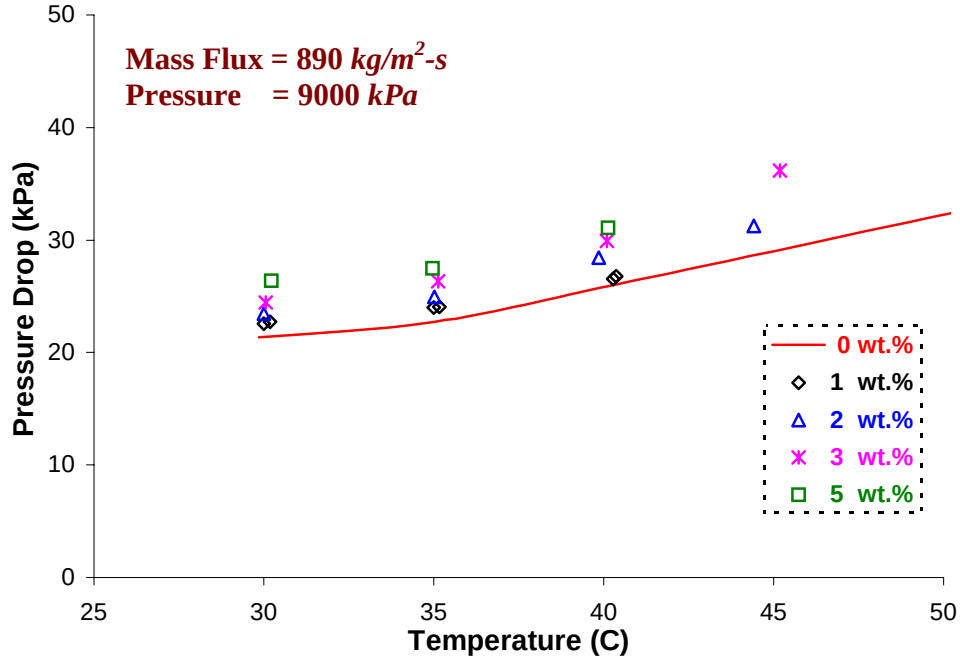

Figure 5.7. Pressure drop (POE oil addition)

Four different oil concentrations (1%, 2%, 3% and 5% in weight) were tested. Figure 5.6 shows the heat transfer coefficient results for the POE oil addition. As with the last two oils, the POE oil addition suppresses the heat transfer effect. A higher oil concentration leads to a lower heat transfer coefficient, which was reduced by up to 38% for 5% oil addition.

Figure 5.7 shows the pressure drop results for POE oil addition. As shown, additional oil causes higher pressure drop. Pressure drop can increase by up to 20% for 5% POE oil addition.

5.4.4 Discussion

From the experimental results, it can be concluded generally that oil addition will suppress the heat transfer effect and increase the pressure drop for the supercritical gas cooling process. Both impacts are negative for a heat exchanger.

When an oil/CO_2 mixture passes through the microchannels, some oil droplets (in small oil concentrations) or oil film (in large oil concentrations) will attach to the tube wall, which adds to thermal resistance in both the mass transfer and heat transfer processes. Those oil droplets (or oil liquid film) will obstruct the heat transfer between the CO_2 bulk flow and the tube wall. Higher oil concentration will lead to more oil droplets or oil film, and consequently more thermal resistance. Thus, the heat transfer coefficient decreases as the oil concentration increases.

Since the viscosity of liquid oil is much greater than supercritical CO_2, those oil droplets (or oil film) attached to the tube wall will significantly increase the friction

resistance for the bulk flow. Accordingly, more pressure drop is needed to drive the gas flow through the microchannels.

Based on the experimental results, immiscible oils have more negative influence on pressure drop than miscible oils. For immiscible oils (PAG/AN and PAG oil), the pressure drop increases up to 45~50%. But for miscible oil (POE), pressure drop only increases up to 20%, under 5 wt.% oil concentration and for equivalent operating conditions. This phenomenon is explained by the fact that there is less oil that turns into droplets or film for miscible oil, assuming that miscible oil mixes better with CO_2. On the other hand, miscible oil does not present evident advantage over immiscible oil for heat transfer performance.

Even though it generates less pressure drop than immiscible oil does, miscible oil has its own disadvantage. Generally speaking, miscible oil is more difficult to separate from the refrigerant with current oil separation technology.

Due to some error found in data reduction, a few data of oil tests in high temperature region are eliminated. However, as shown in figures, those missing data won't change the trend line of the data, therefore has limited effect on the concluding remarks.

5.5 Conclusions

The heat transfer and pressure drop of oil/CO_2 mixtures, with different oil types and concentrations, were measured in the supercritical gas cooling process of CO_2 in

microchannels. The experimental data were chosen in the temperature region around the pseudo-critical temperature, given a pressure of 9Mpa and mass flux of 890kg/m^2-s.

As expected, oil addition has a significantly negative effect on both heat transfer coefficient and pressure drop. At higher oil concentrations the heat transfer coefficients are substantially lower and the pressure drops are higher. The heat transfer coefficient decreases by up to 57% for immiscible oil PAG/AN and 38% for miscible oil POE at an oil concentration of 5 wt.%. The pressure drop increases by up to 49% for immiscible oil PAG and 20% for miscible oil POE with 5 wt.% oil concentration. As far as the type of oil is concerned, the immiscible oil demonstrated more negative influence on the pressure drops than the miscible oil. This is because miscible oil may mix better with CO_2 than immiscible oil. Effect of miscibility is not observed on heat transfer performance.

CHAPTER 6

STRUCTURAL & DYNAMICAL ANALYSIS OF MICROCHANNEL HEAT EXCHANGERS

6.1 Introduction

The design and characteristics of microchannel heat exchangers (HXs) used for refrigerant CO_2 are different from those used for conventional refrigerants. This is because the operating pressure of a CO_2 system is much higher than that of the others. Also, since the typical operating conditions of CO_2 are near the critical region, the performance and heat transfer characteristics of the two kinds of heat exchangers are expected to be different.

Research on microchannel heat exchangers with CO_2 refrigerant is relatively new, and the available information is limited. In 1998, Pettersen et al. developed a micro channel heat exchanger for CO_2 and experimentally evaluated the overall heat transfer coefficient. In 2000, Cutler et al. developed a transcritical carbon dioxide environmental control unit by using microchannel heat exchangers. They reported that the capacity of a microchannel evaporator increases with increasing refrigerant mass flow rates. Pitla et al. (2000) numerically analyzed heat exchangers for transcritical CO_2 systems. They suggested that experimental results were hard to predict when the operating conditions are close to the critical point. Ortiz and Groll (2000) developed a finite-element model to study a microchannel CO_2 evaporator. In 2001, Zhao experimentally studied the performance of CO_2 microchannel evaporators and gas coolers over a range of operating

conditions found in residential heat pumps.

Although the thermal design and analysis of CO_2 micro channel heat exchangers has been carried out recently, dynamical analysis of CO_2 microchannel heat exchangers has not received much attention yet. To fit the temperature range of an ordinary heat pump or heating system, CO_2 has to be used in a sub-critical or supercritical region (critical point: 31.1^{o}C / 73.8 bar). The pressure inside a CO_2 heat exchanger is expected to range up to 10 *MPa* (1,400 *Psi*). For safety reasons, this heat exchanger is required to withstand pressures up to 15 *MPa*. The higher the pressure in the system, less stiff are the microchannel tubes, and the design requirements of compact size and low weight make it necessary to determine an optimal mechanical design of the heat exchanger. To create such a design, an effective simulation model is needed to evaluate the influence of different parameters. However, no studies have been undertaken to systematically develop a model for structural design.

To address the above mentioned need, in this chapter, a finite-element method (FEM) based analysis of tube-fin heat exchangers is carried out to develop a model for HX design. This model and related analysis can serve as a guide for structural and mechanical design analysis of heat exchangers for a variety of applications. All of the numerical simulations are performed via ANSYS, if not indicated explicitly. Experimental results are also included for comparison.

6.2 Static Stress Analysis - Manifold Design

Due to the high pressure in CO_2 heat exchangers and the requirement of material saving, a static stress analysis was performed for the manifold design. The objective was to evaluate the manifold alternatives based on weight cost and failure criteria. Three manifold alternatives are studied in this section: i) single-tube headers, ii) double-tube extrusion headers, and iii) inline tube headers.

6.2.1 Single-Tube Header

Single tubes are the most common design of headers due to their simple design. However, high volumes and weights are required for a high-pressure system to avoid material failure.

In Figure 6.1 and Figure 6.2, the mesh elements and results of failure analysis carried out for a single tube header are shown. The single tube has an inner diameter of 18 *mm* and a thickness of 2.0 *mm*. A microchannel tube is inserted and soldered to the header. A pressure of 25 *MPa* is applied to the inner walls of the header and the microchannel tube, while the two ends of header are fixed.

The failure factor ξ is defined as the ratio of local stress over the failure stress, as shown in Equation 6.1. Whenever the failure factor is higher than 1, failure behavior is assumed to happen.

$$\xi = Maximum\ of \begin{cases} \dfrac{\sigma_{xt}}{\sigma_{xt}^{f}} \quad or \quad \dfrac{\sigma_{xc}}{\sigma_{xc}^{f}} \quad whichever\ is\ applicable \\ \dfrac{\sigma_{yt}}{\sigma_{yt}^{f}} \quad or \quad \dfrac{\sigma_{yc}}{\sigma_{yc}^{f}} \quad whichever\ is\ applicable \\ \dfrac{\sigma_{zt}}{\sigma_{zt}^{f}} \quad or \quad \dfrac{\sigma_{zc}}{\sigma_{zc}^{f}} \quad whichever\ is\ applicable \\ \left|\dfrac{\sigma_{xy}}{\sigma_{xy}^{f}}\right| \\ \left|\dfrac{\sigma_{yz}}{\sigma_{yz}^{f}}\right| \\ \left|\dfrac{\sigma_{zx}}{\sigma_{zx}^{f}}\right| \end{cases} \tag{6.1}$$

where ξ is failure factor, σ is stress, subscript *x*, *y*, *z* present directions, subscript *t* = *tensile*, *c* = *compression*, superscription *f* = *failure*, and $\sigma_{xt} = \max\begin{cases} 0 \\ \sigma_x \end{cases}$, $\sigma_{xc} = \min\begin{cases} \sigma_x \\ 0 \end{cases}$.

In Figure 6.2, different colors are used to indicate the contours of failure factor. As shown, the microchannels has lower failure factor than the header, which is due to its smaller inner diameter. The header itself could withstand the pressure of 25 *MPa*. However, the maximum failure factor is 1.064, which locates at the junction of the header and the microchannels tube. This suggests that the junction is the weakest part and a thickness of at least 2 *mm* is required for a header with an ID of 18 *mm* to survive a pressure of 25 *MPa*.

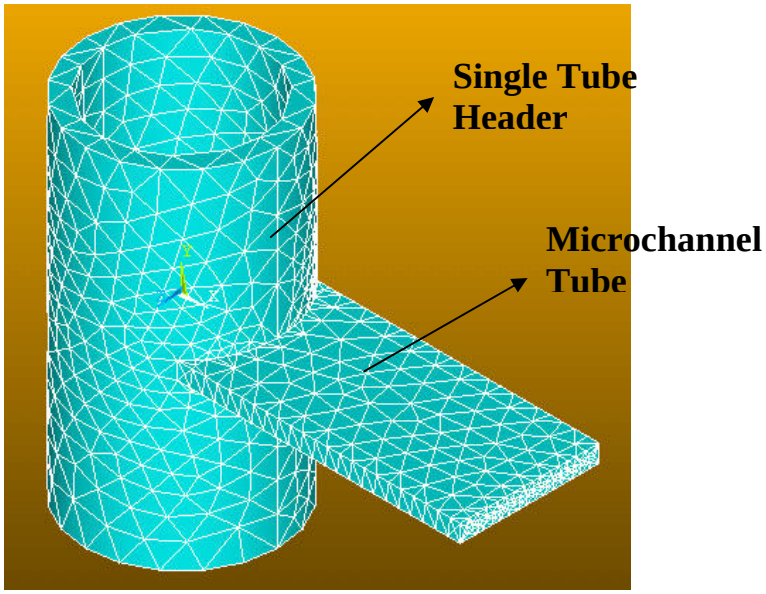

Figure 6.1. Mesh elements of single-tube header in ANSYS

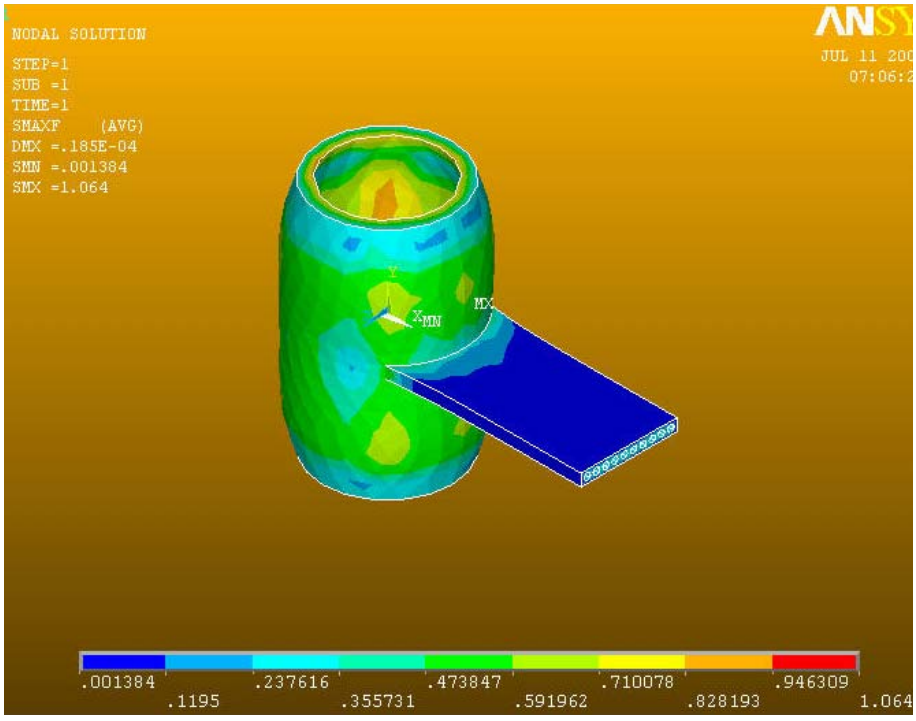

Figure 6.2. Failure results for single-tube header (pressure of 25 *MPa*)

6.2.2 Double-Tube Extrusion Header

It has been argued that a double-tube extrusion header can better withstand high pressure with low volume and low weight. However, the numerical simulation results show the opposite, as discussed next.

In Figure 6.3 and Figure 6.4, the mesh elements and the results of failure analysis for a double-tube extrusion header are shown. The header has an inner diameter of 13 *mm* and a thickness of 1.4 *mm*. A microchannel tube is inserted and soldered to the header. A pressure of 25 *MPa* is applied to the inner walls of both the header and the microchannel tube, while the two ends of header are fixed.

As shown in Figure 6.4, the maximum failure factor is 9.967, far above the failure criteria of 1, which means minor modification in dimension of the header won't solve the problem. The stress concentration is located at the connection between the microchannel tube and the junction of the double tube. This result suggests that the design of double-tube extrusion header is vulnerable to high pressure loadings.

Therefore, it can be concluded that double-tube extrusion header is not a good option for a high-pressure system such as a CO_2 heat exchanger, unless special enhancement is made at the junction, such as thick soldering. However, such effort may also block some microchannels.

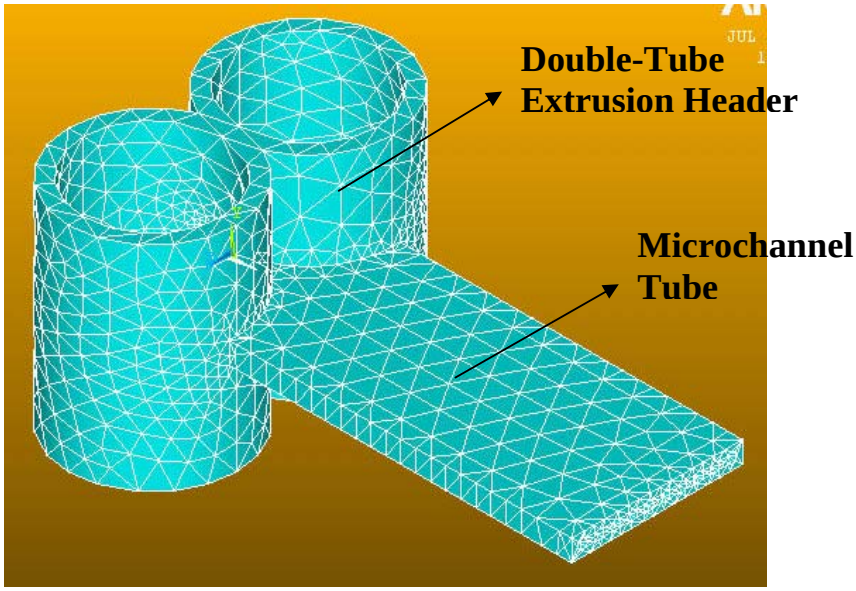

Figure 6.3. Mesh elements of double-tube extrusion header in ANSYS

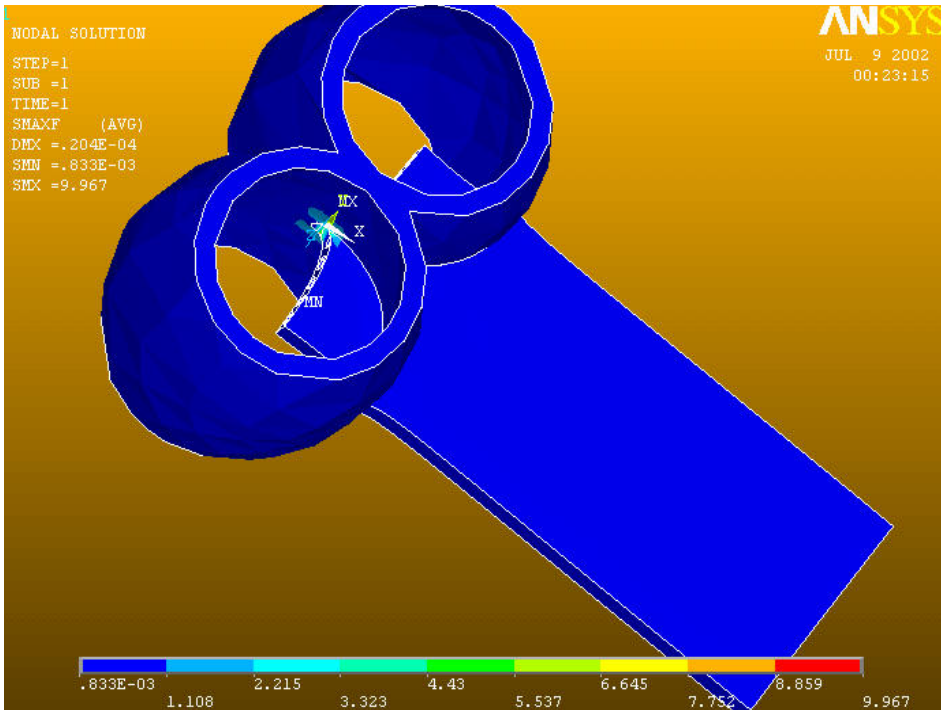

Figure 6.4. Failure results for double-tube extrusion header (pressure of 25 *MPa*)

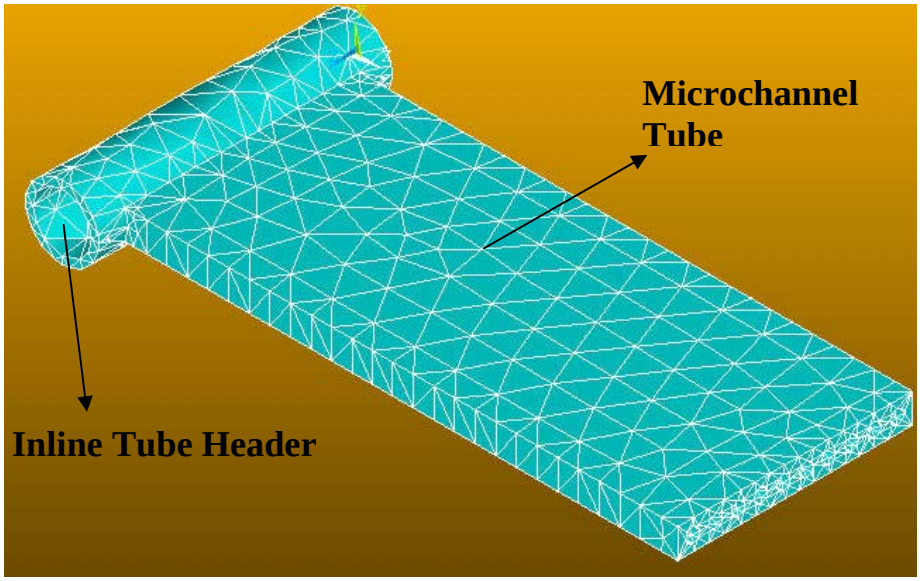

Figure 6.5. Mesh elements of inline-tube header in ANSYS

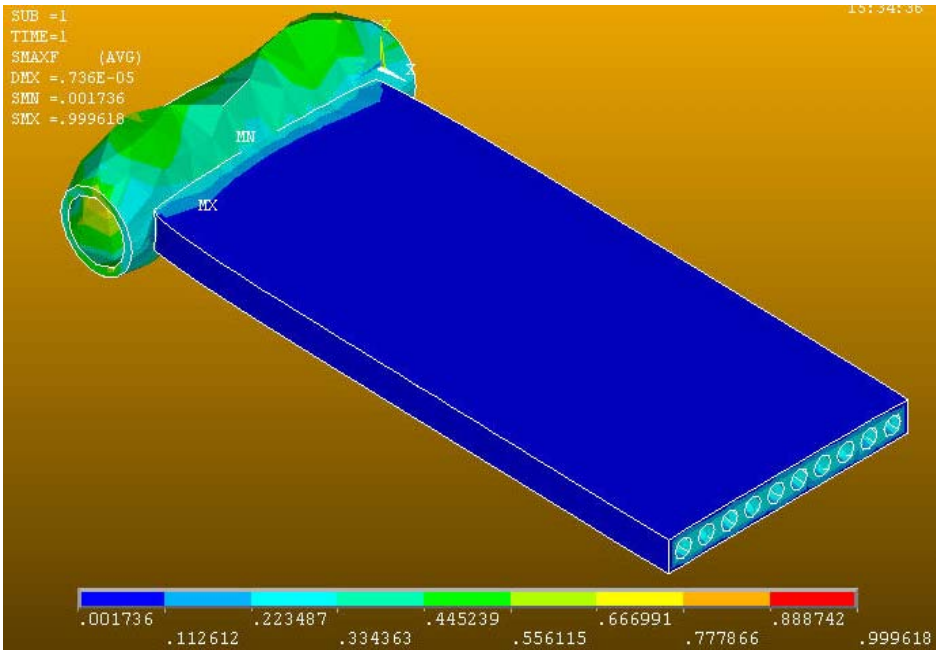

Figure 6.6. Failure result for inline tube header (pressure of 25 *MPa*)

6.2.3 Inline Tube Header

Due to its small diameter, it would seem that an inline tube should be able to survive high pressure while significantly saving volume and weight. In Figure 6.5 and Figure 6.6, the mesh elements and the results of the failure analysis of an inline tube header are shown. The header has an inner diameter of 4.5 *mm* and a thickness of 0.5 *mm*. A microchannel tube is inserted and soldered to the header. A pressure of 25 *MPa* is applied to the inner walls of both the header and the microchannel tube, while the two ends of header are fixed.

As shown in the figure, the maximum failure factor is 0.9996, less than the failure criteria of 1, which means the current geometry will survive the high pressure of 25 *MPa*. And again, the max failure factor locates at the junction of the header and the microchannels tube.

The diameter and thickness of the inline tube header is only 1/6 and 1/4, respectively, of the corresponding diameter and thickness of the single tube header. The weight saving of the inline tube is significant.

6.3 Development of Solid Model and Simulation Scheme

A main objective of the present work is to develop a finite-dimensional vibratory model (Balachandran and Magrab, 2003) for a tube-fin heat exchanger and to use this model to determine the first of many natural frequencies of the system. This model will have the form

$$[M]\{\ddot{q}\} + [C]\{\dot{q}\} + [K]\{q\} = \{Q\} \qquad (6.2)$$

where the $N\times1$ displacement vector is represented by $\{q\}$, the inertia matrix is represented by [***M***], the stiffness matrix is represented by [***K***], and the damping matrix is represented by [***C***]. Each matrix is an $N\times N$ matrix, and the $N\times1$ force vector is represented by {***Q***}. here, such a finite-dimensional model is developed by using ANSYS, a commercial finite element analysis software.

6.3.1 Equivalent Geometry

For finite element analysis, it is always difficult to model and mesh a multi-port microchannel tube due to its complex geometry. The geometry of a typical microchannel tube is shown in Figure 6.7. In many cases, the required meshes become too numerous for the computation program to handle.

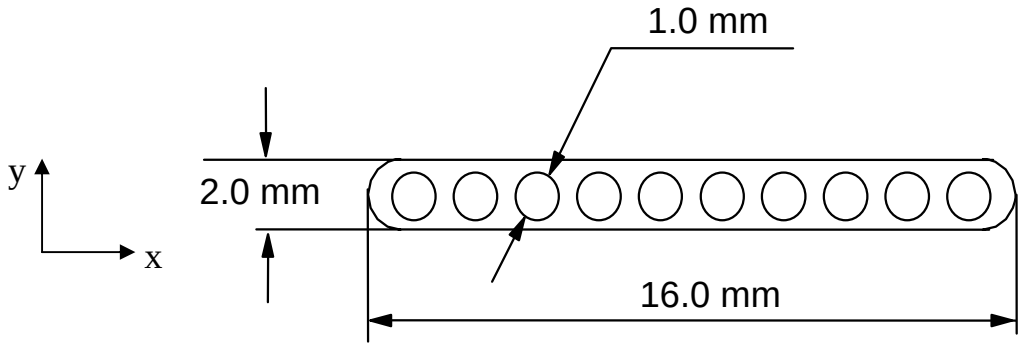

Figure 6.7. Cross section of microchannel tube

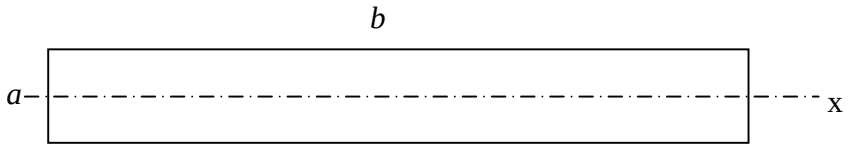

Figure 6.8. Alternative cross section

If certain bending axis or only certain vibration directions are of concern, such complex geometry is unnecessary to consider and it is inefficient for evaluating the dynamical characteristics. For example, if the x-axis is the bending axis, the geometry in Figure 6.7 can be simplified to an alternative rectangular geometry, as shown in Figure 6.8.

Assuming the same area and same area moment of inertia I_{xx}, the size of a and b are calculated as

$$a = 2.25\ mm \qquad b = 10.74\ mm$$

where, I_{xx} is defined as $I_{xx} = \iint y^2 dA$.

Case Study. To validate the equivalent geometry method, an example with two ports is given below. In Figure 6.9, the two geometries have the same cross-section area and the same area moment of inertia I_{xx}.

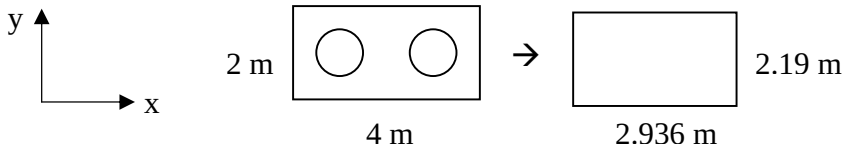

Figure 6.9. Two-port cross section and equivalent rectangular cross section

Table 6.1. Natural Frequencies Comparison

Mode #	Natural Frequencies (*Hz*) for 2 ports cross section	Natural Frequencies (*Hz*) for rectangular cross section
1	4.50	4.53
2	8.12	6.01
3	12.15	12.30
4	21.14	16.14

With a length of 50 *m*, material of aluminum, and the clamped-clamped boundary condition, modal analyses were performed in ANSYS to obtain the natural frequencies and the mode shapes for both geometries. The first four natural frequencies obtained are shown in Table 6.1, and the corresponding vibration shapes are shown in Figure 6.10.

In Figure 6.10, the four modes shown on the left correspond to the first four natural frequencies of the two-port tubes, and the four modes shown on the right correspond to the first four natural frequencies of the rectangular bar. From Table 6.1, it can be observed that both the first and the third natural frequencies are very close to each other. On checking the vibration modes from Figure 6.10, it can be found that the deformation of the first and third vibration is about the X-axis, so that I_{xx} is dominant in these cases. Whenever the deformation of vibration (second and fourth) is about the Y-axis, I_{yy} would be dominant.

From the above analysis, it is clear that the equivalent geometry would be valid as long as the deformation of vibration matches the assumption (i.e., dominant I_{xx} or dominant I_{yy}). In this chapter, all the microchannel tubes were simplified as a rectangular bar by using the equivalent geometry method.

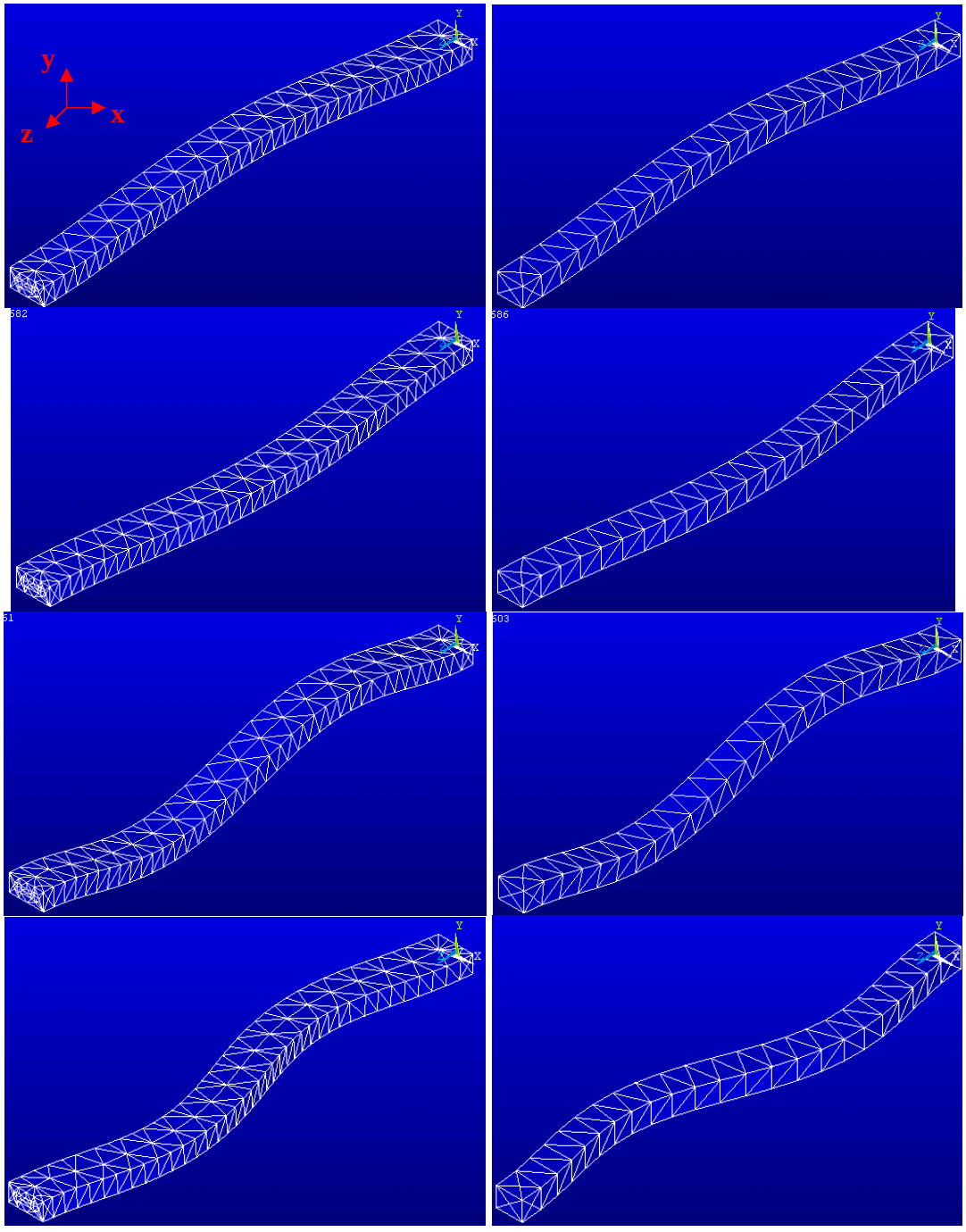

Figure 6.10. First 4 vibration modes:
two-port tube (left-side) and equivalent rectangular bar (right-side)

6.3.2 Fin Approximation

A considerable challenge in modeling a tube-fin heat exchanger is effectively approximation of the fin arrays, which are used between the microchannel tubes to enhance the airside heat transfer coefficient. Such an approximation is critical for computational tractability, since the total fin number can be in the hundreds or thousands, depending on the heat exchanger's dimensions. It would be impossible to model every single fin using the full meshing method, given the computational cert.

Therefore, two approximation methods for fin modeling have been developed for this work: i) the shell element approximation method and ii) the effective block approximation method. The first method is an approximation to a single fin while the second one is an approximation to a fin array.

6.3.2.1. Shell Element Approximation Method

Since the fin thickness is quite small (0.1~0.4mm), it is natural to model each fin as a shell element, as shown in Figure 6.11. By contrast, a full mesh of the fin would be as shown in Figure 6.12, and this mesh would require hundreds of elements for a single fin.

For demonstration, in Figure 6.13, an imaginary heat exchanger unit is shown. This unit includes two headers, a 5-pass microchannel tube with 400 *mm* each pass, and a single fin. In Table 6.2, the results obtained for the first three natural frequencies of the system by using the shell element approximation (Figure 6.11) and the full mesh method (Figure 6.12) are listed, respectively. (It should be noted that the mesh density is considerably lower in the case of the shell element approximation for the same accuracy

in calculation of natural frequencies.) This representative comparison indicates that the shell element approximation is an adequate approximation for the dynamic analysis, if one is interested only in the first few natural frequencies and the corresponding vibration modes.

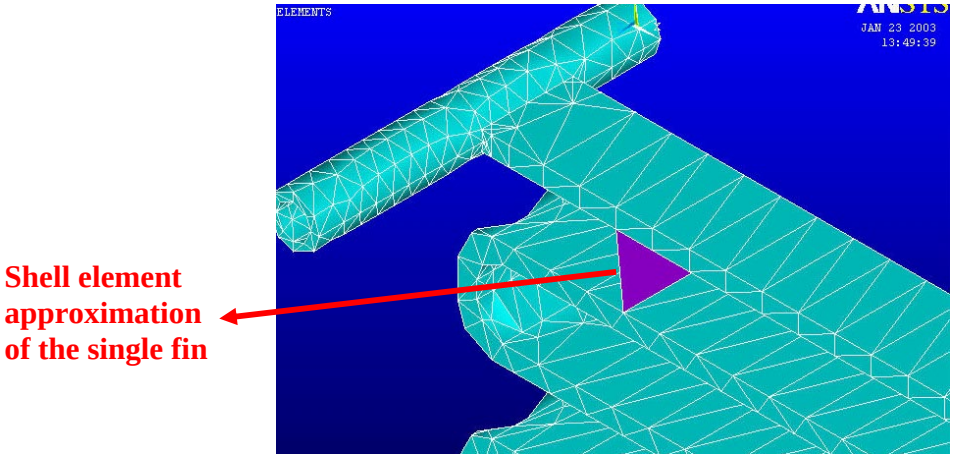

Figure 6.11. Mesh elements of the HX unit using shell element approximation

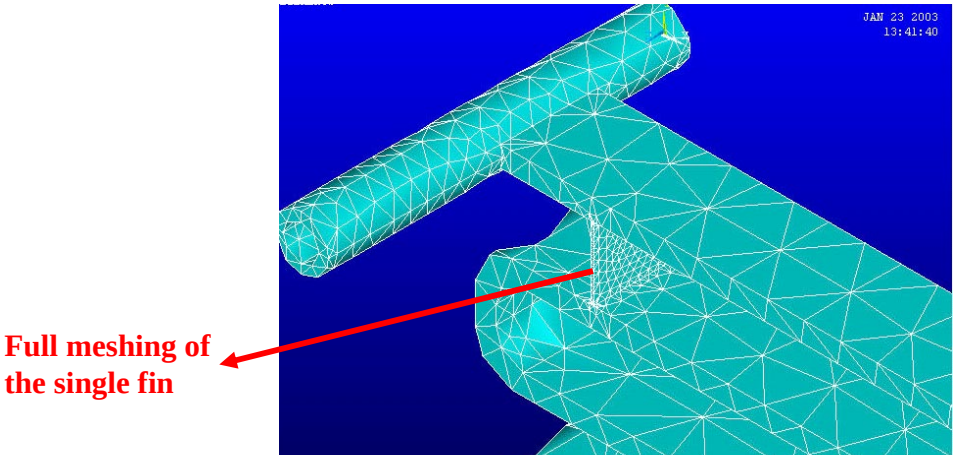

Figure 6.12. Mesh elements of the HX unit using full meshing

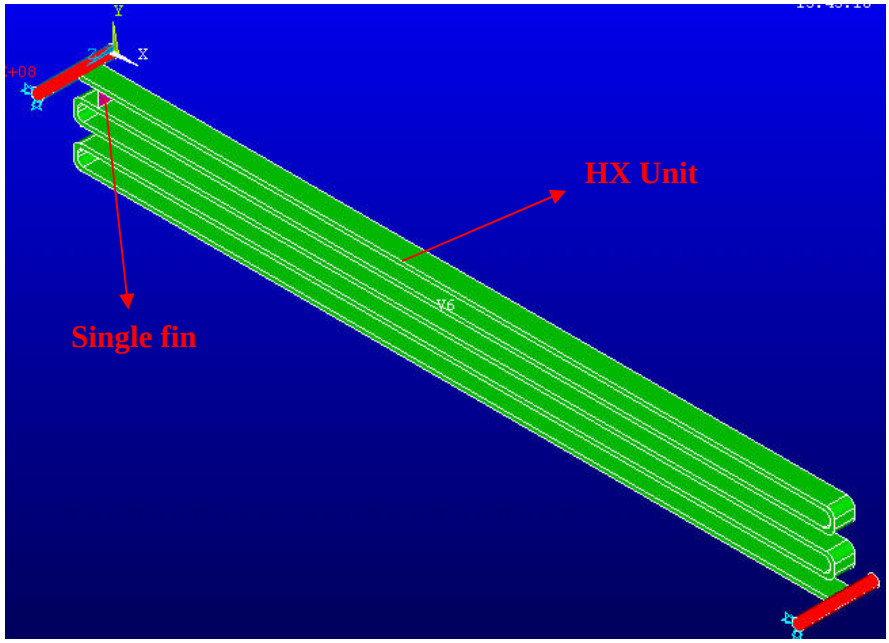

Figure 6.13. A simple imaginary single-fin heat exchanger unit

Table 6.2. Comparison of first three natural frequencies among the full mesh and shell element cases

Mode #	Natural Frequencies (Hz) Shell Element Approximation	Natural Frequencies (Hz) Full Meshing
1st	8.3	8.3
2nd	10.6	11.8
3rd	20.5	20.8

By employing an element approximation scheme, the total required number of the mesh elements can be greatly reduced. Consequently, the simulation workload can be greatly reduced. However, the element approximation method has certain disadvantages. Creating a shell element has to be done manually, which makes it very complex for a large geometry.

6.3.2.2. Effective Block Approximation Method

An alternative to approximating a single fin is to model the whole fin array instead. To achieve this goal, an effective block method has been developed.

As discussed earlier, the meshing of a solid block is simple, and there are not many elements that are required. Thus, the complexity is reduced, while the element number remains low. The basic idea for an equivalent block model is to obtain a model for a fin array that would have the same stiffness and inertial characteristics in the considered direction. This equivalent block model should have a first natural frequency as close as possible to the first natural frequency of the fin array for the considered vibration mode. To determine the smeared properties of the effective solid block, the following was carried out:

i) the effective dimension of the block was determined so that the lengths were the same as that of the fin array

ii) the density of the effective block was determined so that the block had the same mass as the fin array

iii) the Young's modulus of the effective block was determined so that the axial (X) stiffness was the same as that of the fin array in the considered direction (X).

In this method, the effective properties of the effective block are certainly not isotropic. The Young's modulus values along the Y-axis and Z-axis are expected to be much higher than the corresponding value along the X-axis.

To determine the Young's modulus in the considered direction (i.e., the X axis), the detailed steps taken are listed as follows:

1) Certain force is applied on the end of the fin sheet in the direction of interest (major vibration direction), and the corresponding displacement is obtained at this end. As shown in Figure 6.14, the colors ranging from red to blue indicate the displacement magnitude (minimum to maximum) when a certain force is applied along the Y direction at the right end with the left end fixed.
2) Solid block is created with the same outline volume and same mass, to determine the effective density.
3) The same force is applied to the end of the block. The displacement obtained is a function of Young's modulus of the material.
4) To get the same displacement as in step (1), the value of the Young's modulus is determined through trial and error. As shown in Figure 6.15, the force and the boundary conditions are the same as those used in Figure 6.14.

On comparing the results shown in Figure 6.15 to those given in Figure 6.14, it is clear that the effective block approximation provides the same static response for the loading considered. Since they have the same overall stiffness, the same dynamic characteristics are expected.

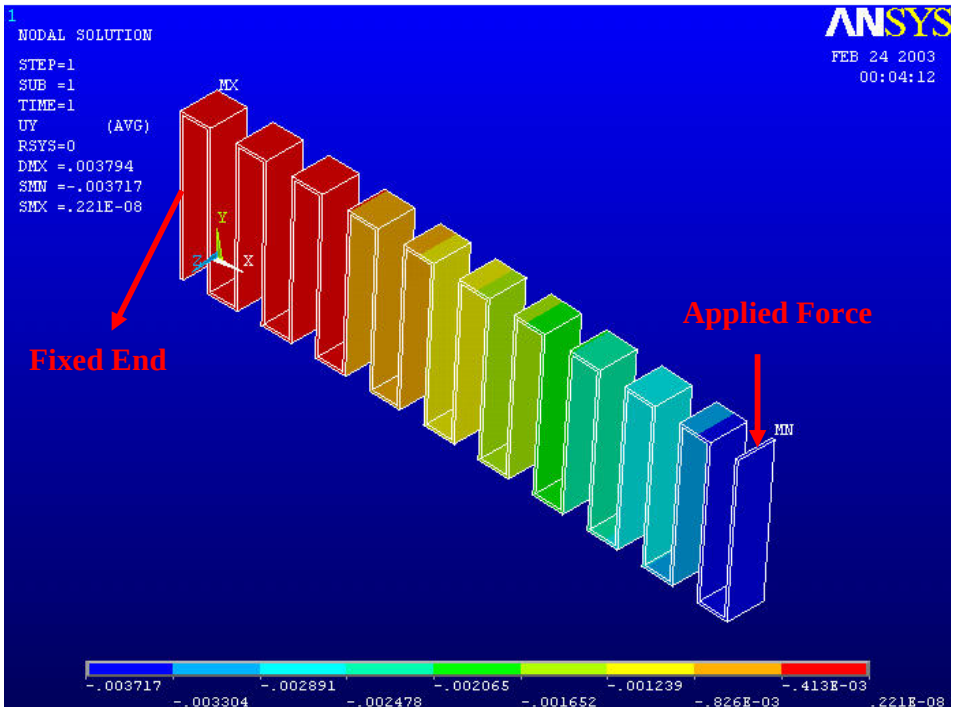

Figure 6.14. Displacement field of the fin array

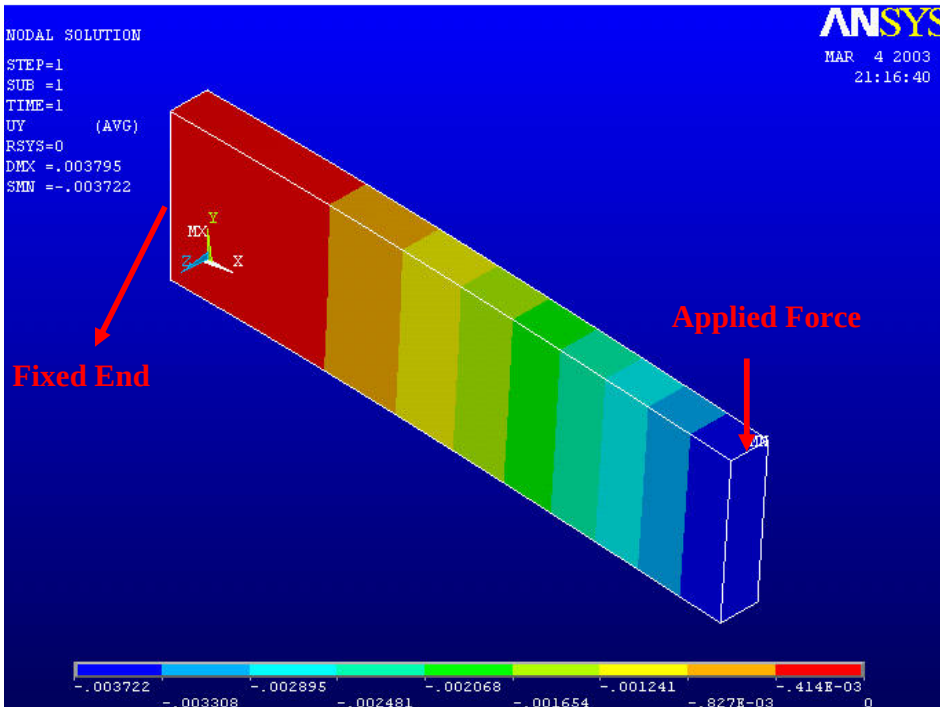

Figure 6.15. Displacement field of the effective block

6.3.2.3. Comparison of Two Methods of Fin Approximation

To compare the two approximation methods discussed previously, a heat exchanger unit with three passes of 300 *mm* long microchannel tubes and a fin density of 8 FPI (fins per inch) was considered. In Figures 6.16 and 6.17, the mesh used to approximate a heat exchanger unit is shown along with the predicted first natural frequency. To generate the result shown in Figure 6.16, a shell element approximation was used for a single fin, and to generate the result shown in Figure 6.17, the effective block method was used to approximate a fin array. For the heat exchanger unit under consideration, both of the approximations yielded results that were fairly close to each other (first natural frequency of 71.9Hz and 72.5Hz, respectively), with a deviation of 0.8%.

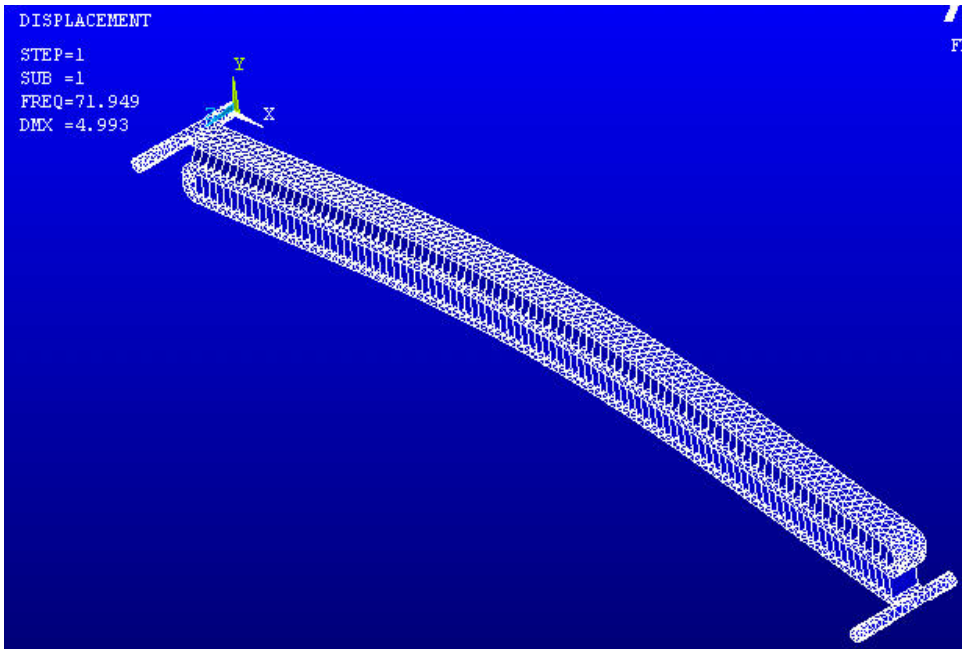

Figure 6.16. Shell-element approximation for the clamped-clamped heat exchanger unit (first natural frequency of 71.9Hz).

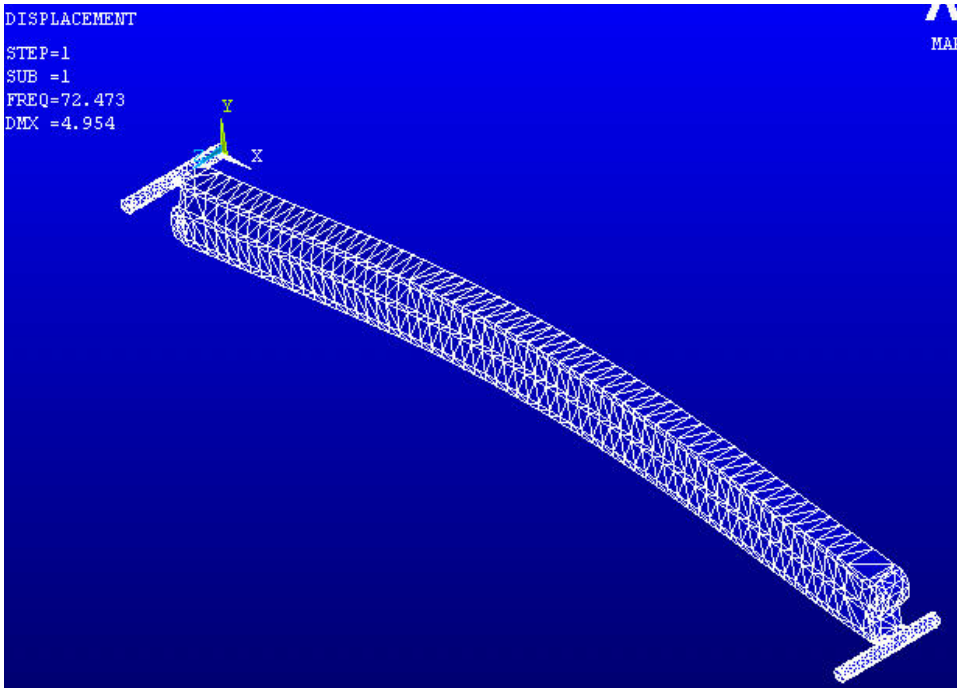

Figure 6.17. Effective block approximation for the clamped-clamped heat exchanger unit (first natural frequency of 72.5Hz).

6.3.3 Large-Scale Structure Modeling – Substructuring Technique

A complete heat exchanger may include dozens of units. For example, a pre-design is modeled, as shown in Figure 6.18. It consists of eleven identical HX units with 5 passes of 460 *mm* for each pass. With 11 units, the length of the HX is 550 *mm*.

Even with the fin simplification techniques discussed previously, the size of the finite-element model may not be computationally tractable. However, since identical units are used, it may not be necessary to model each of the units individually. To this end, the sub-structuring method [Bouhaddi and Fillod, 1996; Yee and Leung, 1978;

Leung, 1997; Craig, 1995] has been used here to convert a set of components of the system into a single super-element.

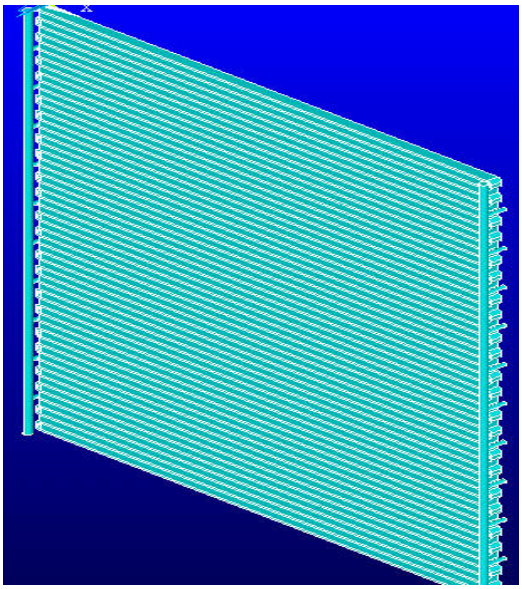

Figure 6.18. Heat exchanger example (including 11 HX units)

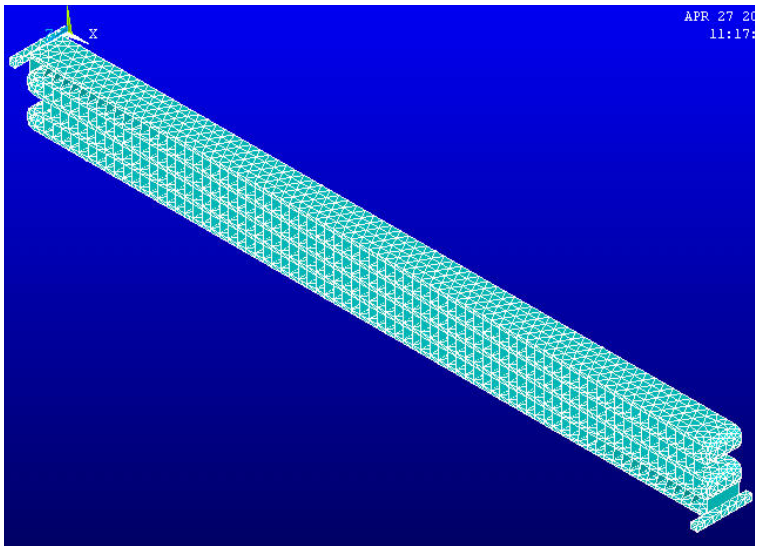

Figure 6.19. Meshing of HX unit for super-element

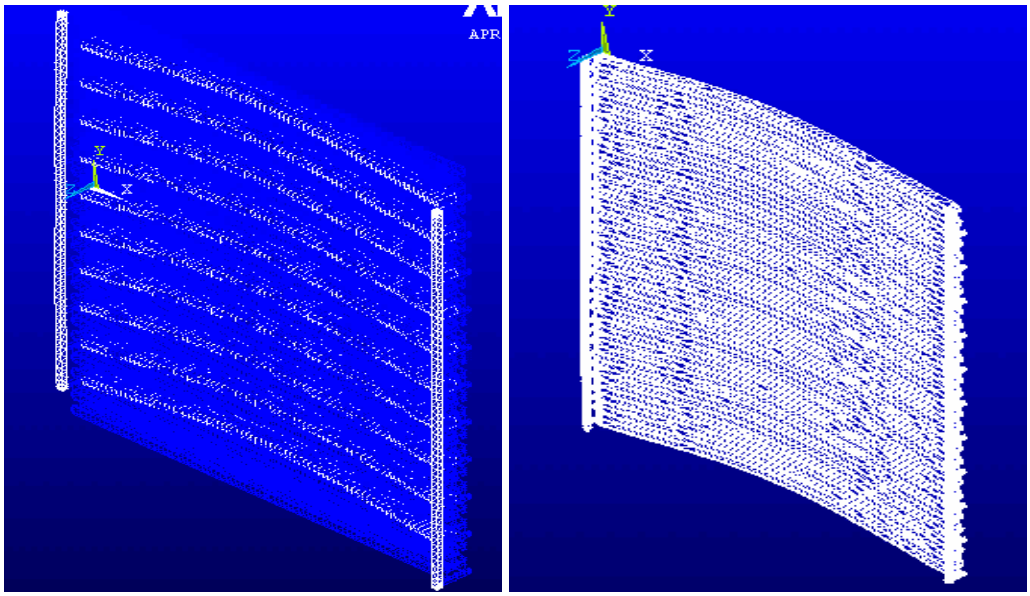

Figure 6.20. Comparison of meshing with super-element to that with full meshing

The substructure analysis uses the technique of matrix reduction to reduce the system matrices to a smaller set of DOFs (degree of freedoms). The basic idea is to divide a large structure into many small structures. By adding those small structures back into the frame of the large structure, the whole structure is simplified. This method is a very effective way to reduce the computational workload.

In Figure 6.19, a meshed heat exchanger unit, which consists of thousands of elements, is shown. The fins here are approximated by shell elements. By using the sub-structuring technique, the HX unit with these thousands of elements can be converted into a single super-element.

For the heat exchanger system of Figure 6.18, when one uses the super-element meshing shown in Figure 6.20 (left-hand side), a first natural frequency of 31.4 Hz is obtained, and when a full mesh is used (right-hand side), a first natural frequency of 33.0

Hz is obtained. This result suggests that the sub-structuring technique can be a useful tool for modeling a large-scale structure.

6.3.4 Experimental Verification

Thus far, steps undertaken to develop a solid model of the heat exchanger in one bending plane have been described in previous sections. This model is validated by comparing the numerical results of the previous section with experimental results.

Two sets of experiments were conducted, one with two different plate-fin modules and another with a heat exchanger. The experiments were conducted in the Vibrations Laboratory in the mechanical engineering department. In the experiments, an acceleration sensor was placed close to the free edge of the structures, and an impact hammer was used to excite the structural system. The vibration signals were acquired by using a data acquisition system. Then, a spectrum analyzer was used to process the measured responses and determine the natural frequencies.

6.3.4.1. Experiments with Plate-Fin Modules

In Figure 6.21 and Figure 6.22, two different plate-fin modules are shown. The assembly shown in Figure 6.21 consists of a plate-fin-plate structure constructed from two copper plates and one aluminum rectangular fin sheet that is sandwiched between the copper plates. The assembly shown in Figure 6.22 consists of a plate-fin-plate-fin-plate structure, with the plate and fin elements identical to those used in the assembly of Figure 6.21. The aluminum fins are attached between the plates with epoxy glue, and the copper

plates are soldered onto a thick copper plate as the base. By using these simple structures, the fin approximation method can be evaluated.

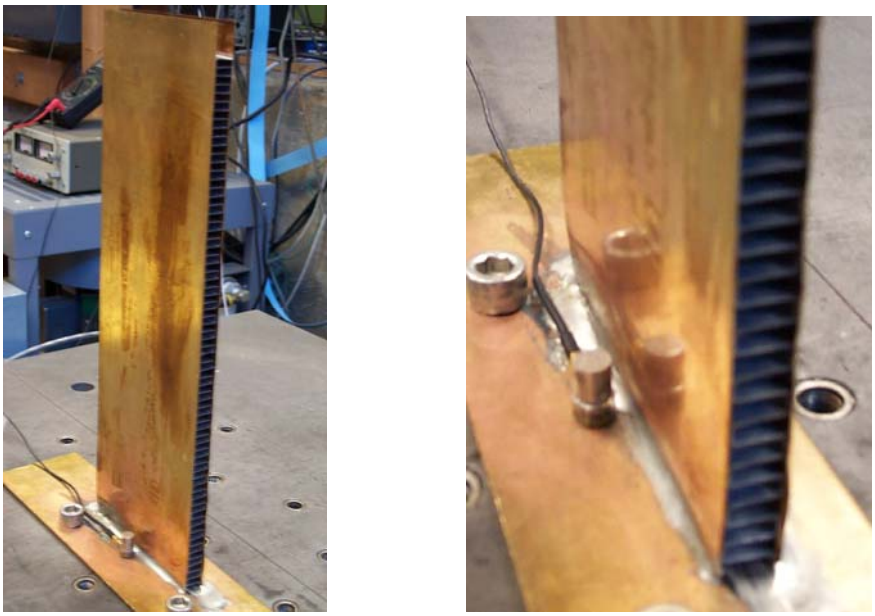

Figure 6.21. Clamped-free plate-fin-plate structure

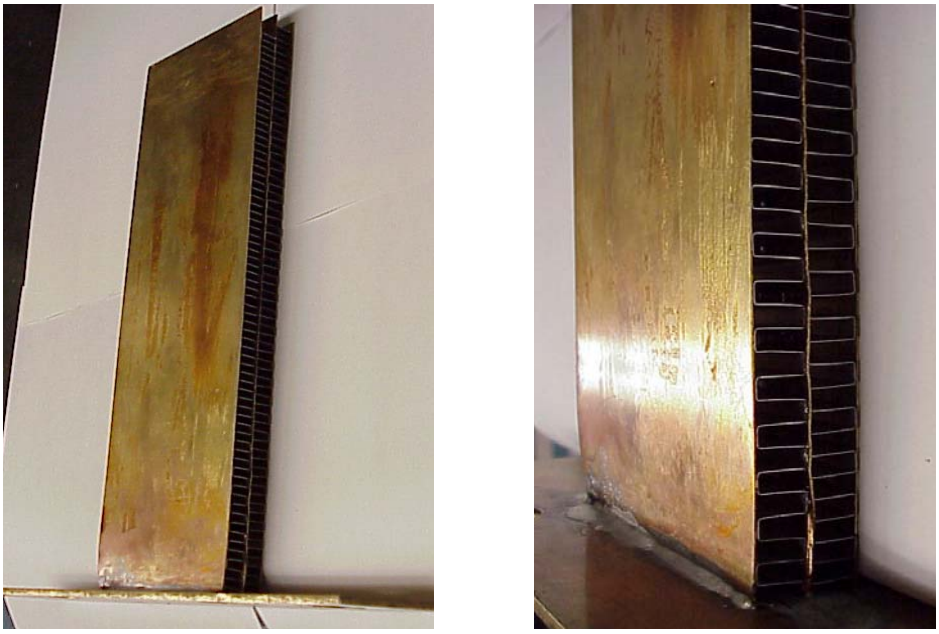

Figure 6.22. Clamped-free plate-fin-plate-fin-plate structure

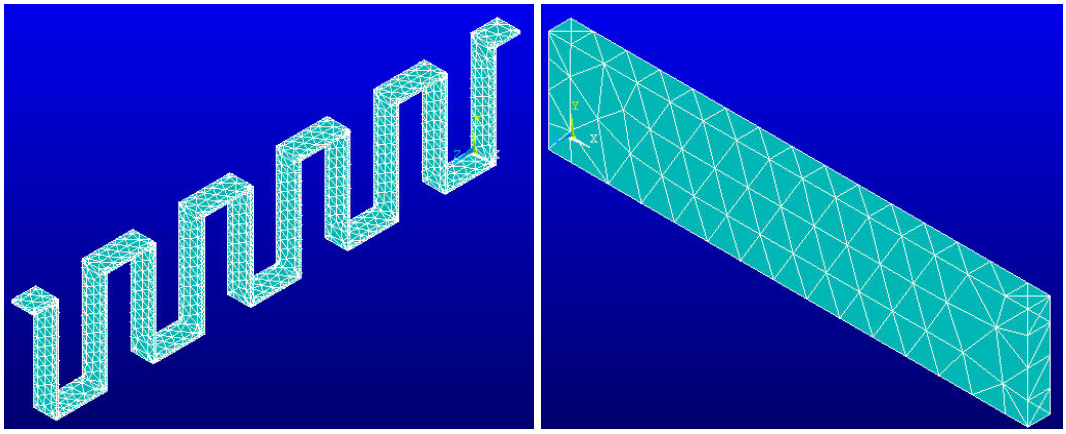

Figure 6.23. Fin array and the effective block in meshes

Table 6.3. Effective properties of the effective solid block

	Fin (Aluminum)	Block (effective properties)
Density (kg/m^3)	2730	122
Young's Modulus (Pa)	6.9×10^{10}	2.56×10^{5}

Table 6.4. First natural frequency comparison between experimental results and simulation results

	Experiment	Simulation	Deviation
Plate-fin-plate	28.0 Hz	32.5 Hz	16%
Plate-fin-plate-fin-plate	33.0 Hz	37.1 Hz	12%

In the simulation, the effective block approximation method was employed, as shown in Figure 6.23. The aluminum fin array can be approximated as an effective solid block, with the properties as shown in Table 6.3.

The experimental results obtained for the first natural frequencies of the two plate-fin modules are shown in Table 6.4, along with the numerical simulation results. Noting that the uncertainty in the experiments is within ±0.5 *Hz*, the deviation between experiments and simulations is in a reasonably acceptable range. As listed, each model's prediction for the first natural frequency is higher than the corresponding experimental value, which is to be expected since the model probably has a stiffer structure, and in addition, the experimental boundary conditions may not be close to the clamped boundary conditions as assumed in the model.

For the plate-fin modules discussed above, the success of the simulation modal is directly related to the success of the fin approximation. As far as the first vibration mode is concerned, the present fin approximation is valid within allowable deviation.

6.3.4.2. Experiments with a Heat Exchanger

In Figure 6.24, the geometry of the microchannel heat exchangers studied in the second set of experiments is shown. The heat exchanger was tightly mounted on the platform. A close up of the fin arrays used in the heat exchanger is shown in Figure 6.25. They do not have the standard rectangular shapes.

It is known that the stiffness of a trapezia structure is greater than a rectangular structure. To account for this characteristic, a modified approximation method was developed. The fin arrays shown in Figure 6.26 are approximated as an effective block, as shown in Figure 6.27, which is used further to develop the solid model. The complete meshing used in the simulations is shown in Figure 6.28.

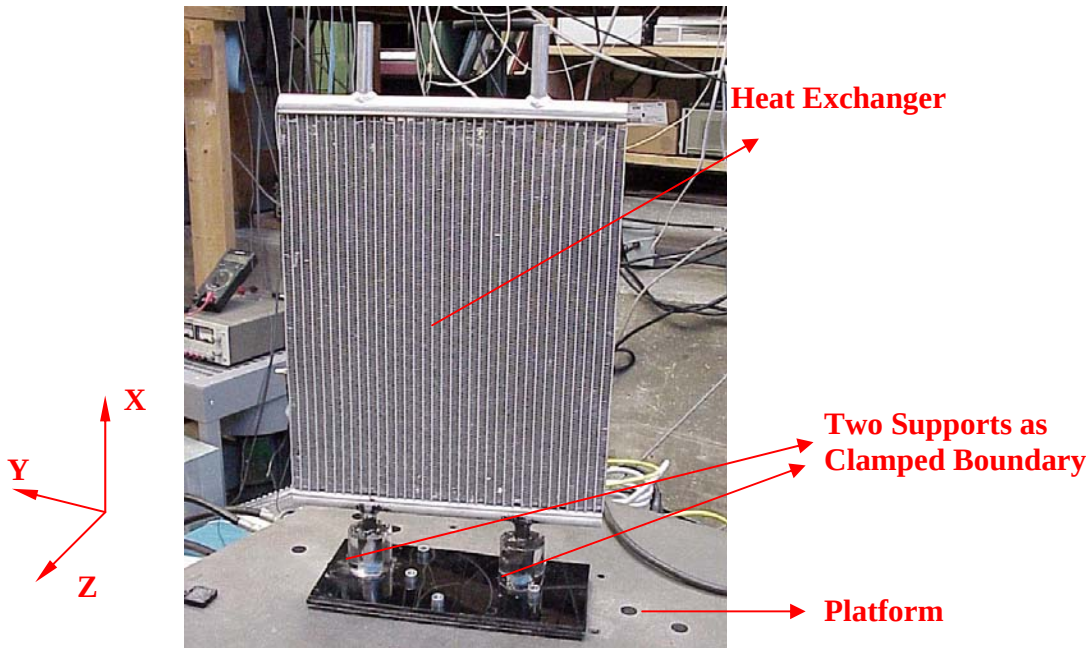

Figure 6.24. Microchannel heat exchanger

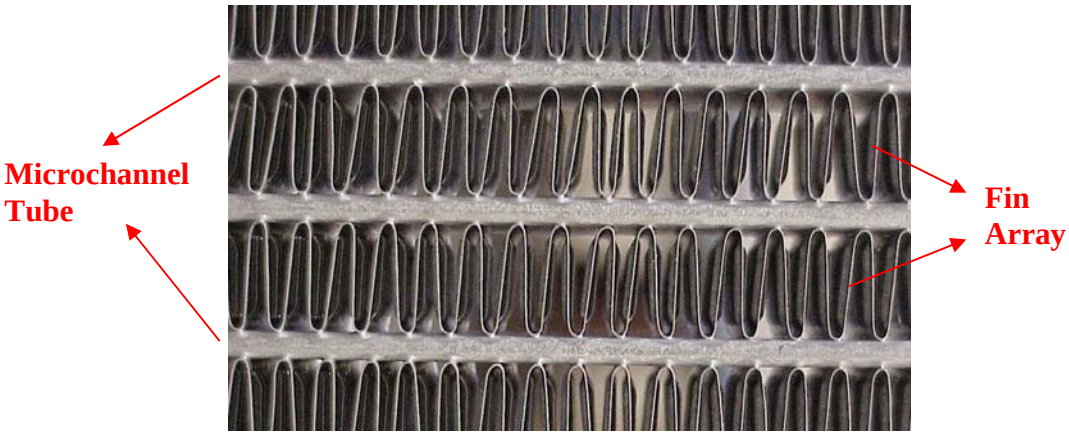

Figure 6.25. Fin arrays in microchannel heat exchanger

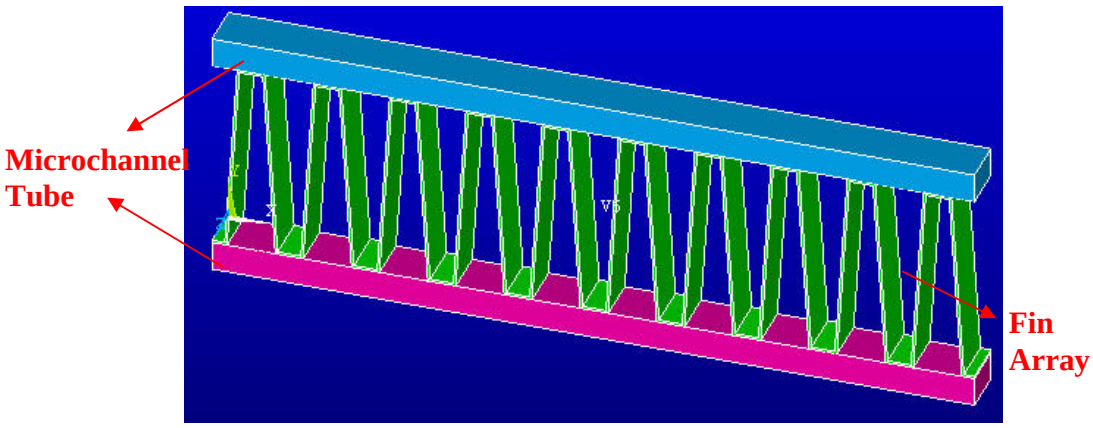

Figure 6.26. Fin array model used in the heat exchanger

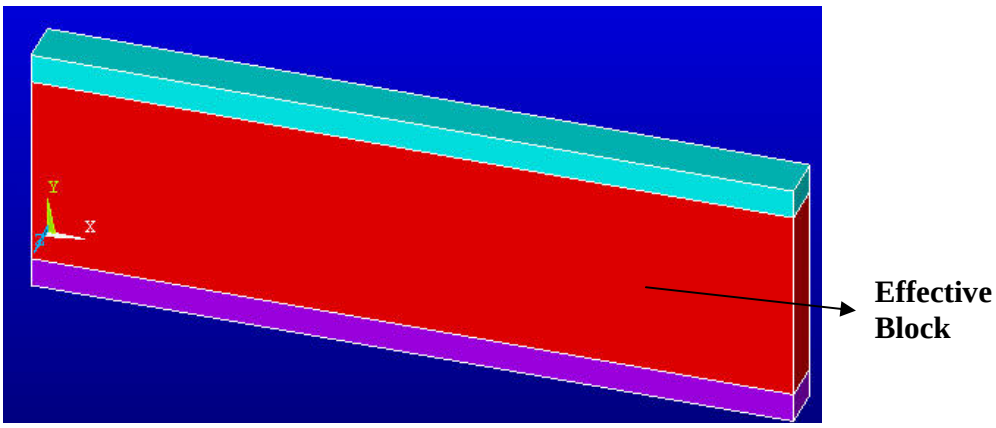

Figure 6.27. Modified effective block approximation of fin array

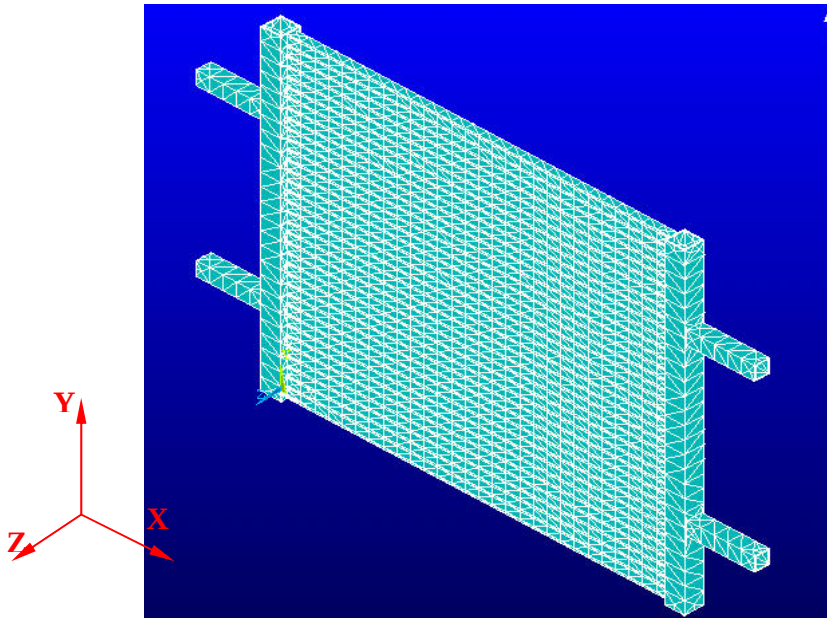

Figure 6.28. Simulation model of the heat exchanger

Modal analysis was conducted by using the simulation model. The first vibration mode about the Y-axis is shown in Figure 6.29 (left side) with a natural frequency of 28.3 *Hz*. The first vibration mode about the Z-axis is shown on the right side of this figure with a natural frequency of 84.6 *Hz*.

Experimental power spectra results obtained at one location of the heat exchanger are shown in Figure 6.30. Three possible natural frequencies were located: 26 *Hz*, 52 *Hz*, and 82 *Hz*.

The numerical predictions for the first natural frequencies for bending vibrations about two different axes (Z and Y) are shown in Table 6.5 along with the experimental values. The agreement is good.

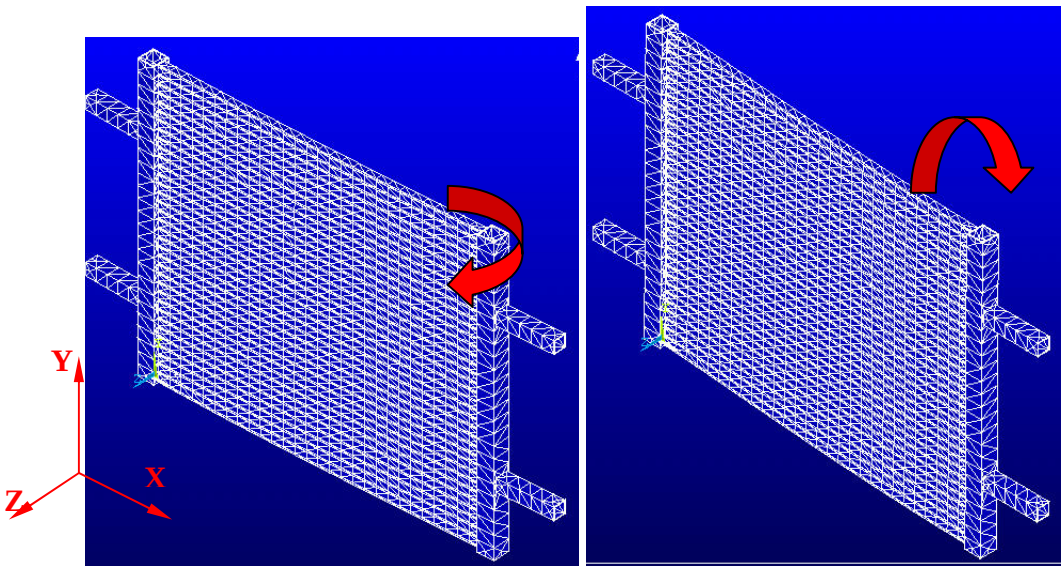

Figure 6.29. First vibration modes about the Y-axis and about the Z-axis

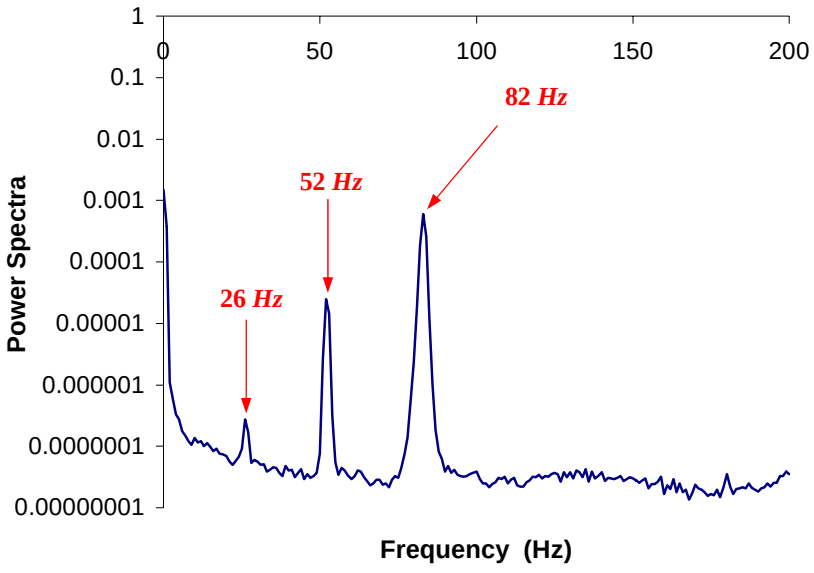

Figure 6.30. Experimentally obtained power spectra indicating possible natural frequency locations

Table 6.5. Natural Frequency Results of the Heat Exchanger

	Experiment	Simulation	Deviation
Vibration about Z-axis	26 Hz	28.3 Hz	9%
Vibration about Y-axis	82 Hz	84.6 Hz	3%

The frequency of 52 Hz in the experiments (Figure 6.30) is the second harmonic (twice the fundamental frequency) of the response of 26 Hz, which may be due to non-linearities in the system and/or a second harmonic in the excitation. The analysis does not capture this, since the model consists of a linear system subjected to a harmonic input.

6.4 Implementations

In the above section, an FEM-based simulation scheme of structural and dynamical analysis for tube-fin heat exchangers was developed. It can serve as a guide for the structural design of heat exchangers for a variety of applications. The tool will be very useful for determining the effects of all kinds of design parameters. In the following sub-sections, many implementations of the simulation are given in order to illustrate its usefulness.

6.4.1 Temperature Effect

For CO_2 HXs, the temperature difference between the refrigerant inlet and outlet may be up to 70 ^oC. The thermal effect of the temperature gradient on the natural

frequencies is studied here.

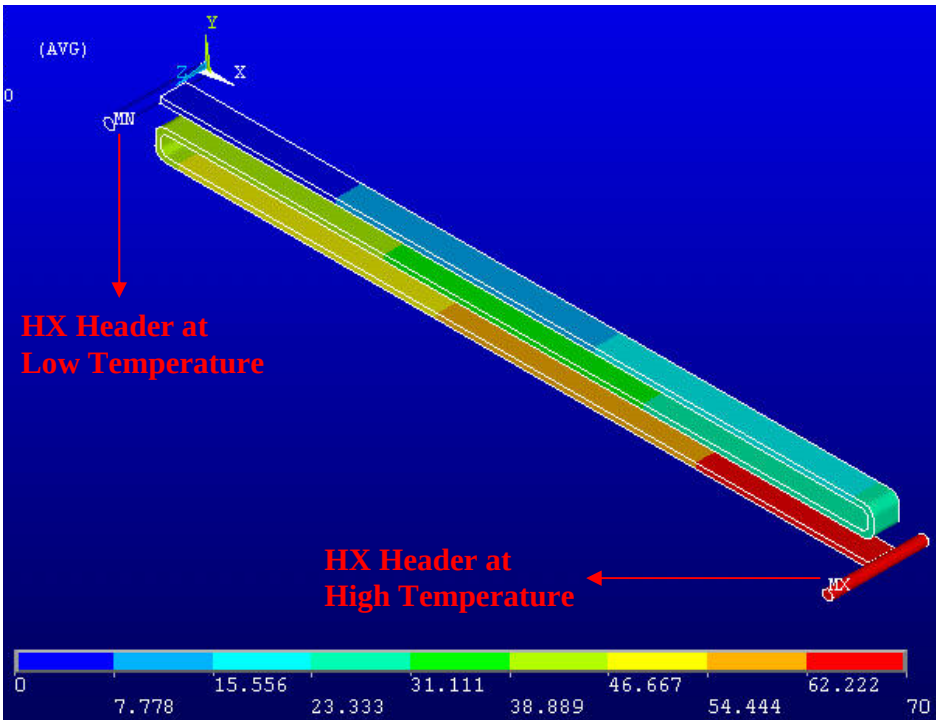

Figure 6.31. Temperature field of a HX unit (°C)

In Figure 6.31, the temperature field of an HX unit with 3 passes and 300 *mm* each pass is shown; the temperature difference between two headers is 70 *°C*. Different colors are used to indicate the temperature contours. The detailed process used for determining the thermal effect on natural frequencies is as follows:

1) According to the temperature boundary condition, the temperature field is solved.

2) The stress field is solved for the given temperature field.

3) The stress solution is applied as the initial stress field and modal analysis is performed to get the natural frequencies.

The first three natural frequencies obtained are listed in Table 6.6, both with and without temperature gradient. From the results shown, the thermal effect on natural frequencies does not exceed 3%. Based on this observation, the thermal effect on the natural frequencies of the HX unit is rather small, perhaps negligible in this case.

Table 6.6. Thermal effect on natural frequencies of HX unit

Mode #	Frequencies (*Hz*) w/ Uniform Temperature	Frequencies (*Hz*) w/ Temperature Gradient	Difference
1	16.1	15.6	3%
2	34.0	34.1	3%
3	50.5	50.3	0.4%

6.4.2 Pressure Effect

In this sub-section, the effect of pressure on one HX unit is studied. Due to the computational limitations, it is impossible to model and analyze the 10-port microchannel tube. Therefore, only the tube with one channel is modeled.

With full meshing, an HX unit with 5 passes and 300 *mm* each pass has been modeled. The meshing elements of the one-channel HX unit with fins are shown in Figure 6.32. Modal analysis shows that the corresponding natural frequency is 63 *Hz* for this one-channel HX unit, which is very close to 62 *Hz* obtained for the 10-channel HX unit. This result is expected because the size change in the direction perpendicular to the vibration plane doesn't affect the vibration frequencies.

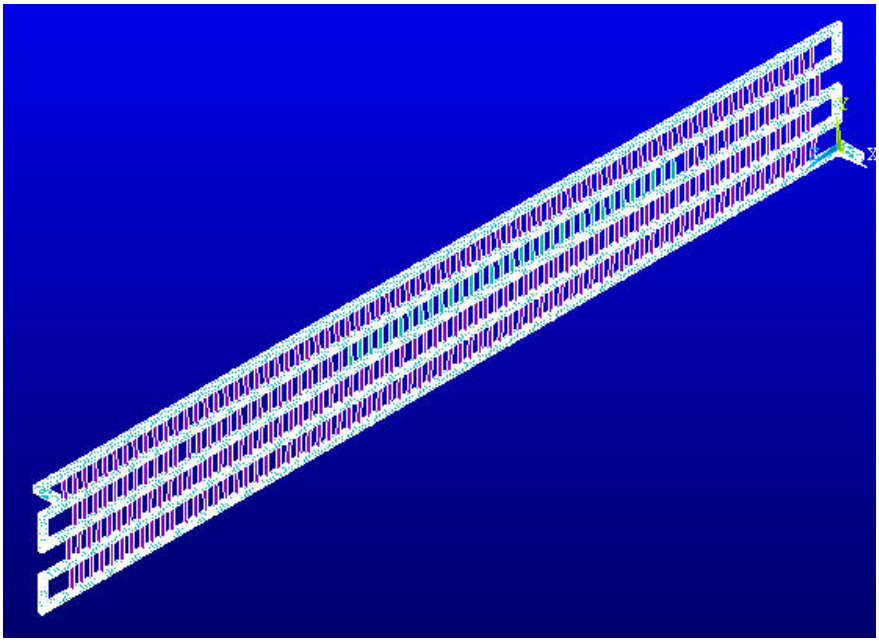

Figure 6.32. Meshing elements of the one-channel HX unit

Table 6.7. Pressure effect on natural frequencies of HX unit

	w/o Pressure	**Pressure of 10 *MPa***	**Pressure Effect**
5-pass HX unit with fins	63 *Hz*	89 *Hz*	+ 41%

The steps undertaken to study the pressure effect are similar to those used to study the temperature effect. First, the stress field is solved for the given pressure field. Then, this stress field is applied as the initial stress field, and modal analysis is performed to get the natural frequencies and the corresponding vibration modes.

Applying a pressure of 10 *MPa* inside the tube, the corresponding first natural frequency increases to 89 *Hz*, which is a 41% increase from 63 *Hz*. The comparison

results are shown in Table 6.7.

The pressure effect may vary for different geometries of HX units, such as the pass numbers and pass lengths. But, one thing is certain, a high pressure leads to an increase in the natural frequencies.

6.4.3 Modal Analysis

Modal analysis is used to determine the natural frequencies and mode shapes of a structure. The natural frequencies and mode shapes are important parameters in the design of a structure for dynamic loading conditions. They are also required for determining the responses to different types of steady and unsteady forcing.

In the design of CO_2 heat exchangers, it is required that the HX survive in certain operating frequency ranges. To this end, the goal is to design the HX with a first natural frequency that is much higher than the operating frequency range. Modal analysis can be used as tool to carry out this design.

In Figure 6.33, a preliminary design is shown for an HX unit with 3 passes and 300 *mm* in each pass. Performing modal analysis, the first natural frequency is determined to be 71.9 *Hz*. For various pass lengths and pass numbers, the results of the modal analysis as shown in Figure 6.34.

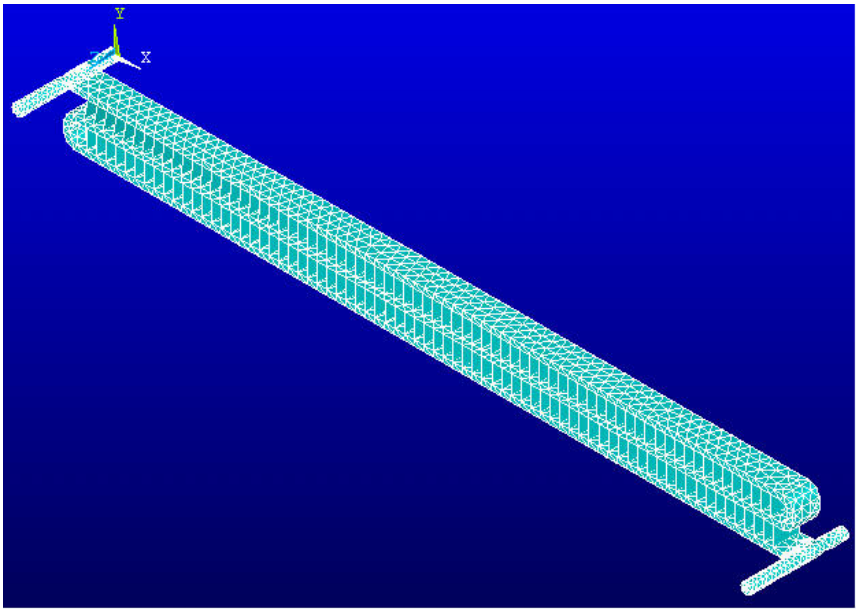

Figure 6.33. Three-pass HX unit with 300 *mm* in each pass

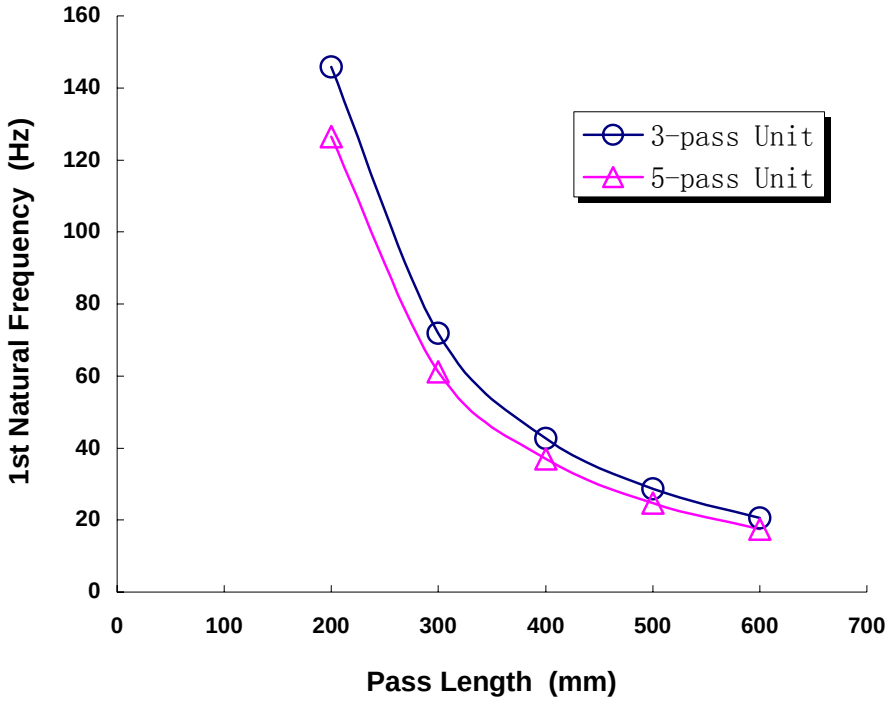

Figure 6.34. First natural frequency versus pass length

As seen, the first natural frequency decreases dramatically as the pass length increases, but it is not sensitive to the pass number. Such characteristics provide useful information for practical design. For example, in Figure 6.35 and Figure 6.36, two different designs of a single HX unit are shown, i) 3-pass unit with 500 *mm* in each pass and ii) 5-pass unit with 300 *mm* in each pass. Both have the same total effective length (1500 *mm*) of microchannel tubes, and they will have the same total heat exchange area, with many units in one heat exchanger, and therefore the two designs will not show much difference in the heat transfer performance.

However, the two designs differ from each other in dynamic characteristics. The first natural frequency of the 3-pass unit is 29.0 *Hz*, while that of the 5-pass unit is 61.8 *Hz*. From the discussion presented above, it becomes clear that the unit with the shorter pass length is the better design for the same total tube length, without loss in the heat transfer performance.

With modal analysis, some other geometry parameters can also be studied, such as fin density, fin span, and fin height. The results are presented in a later section.

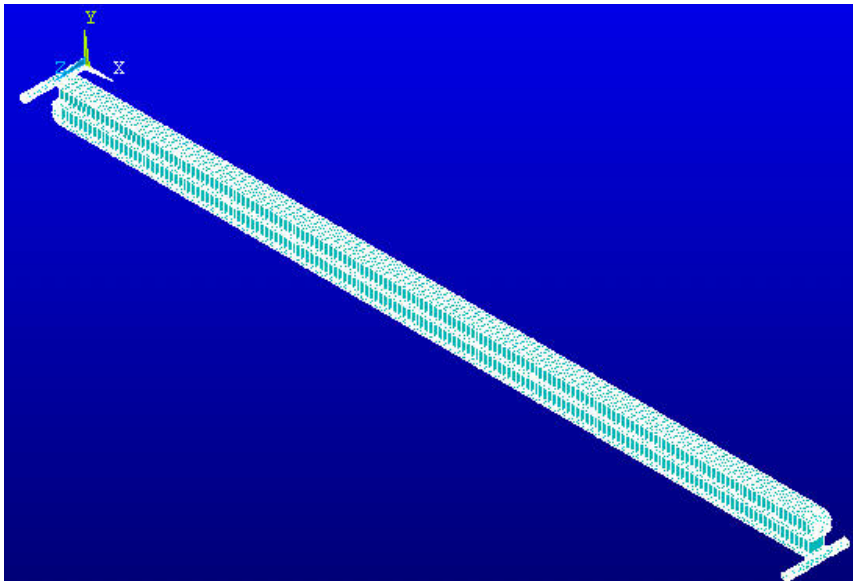

Figure 6.35. 3-pass HX unit with 500 *mm* in each pass

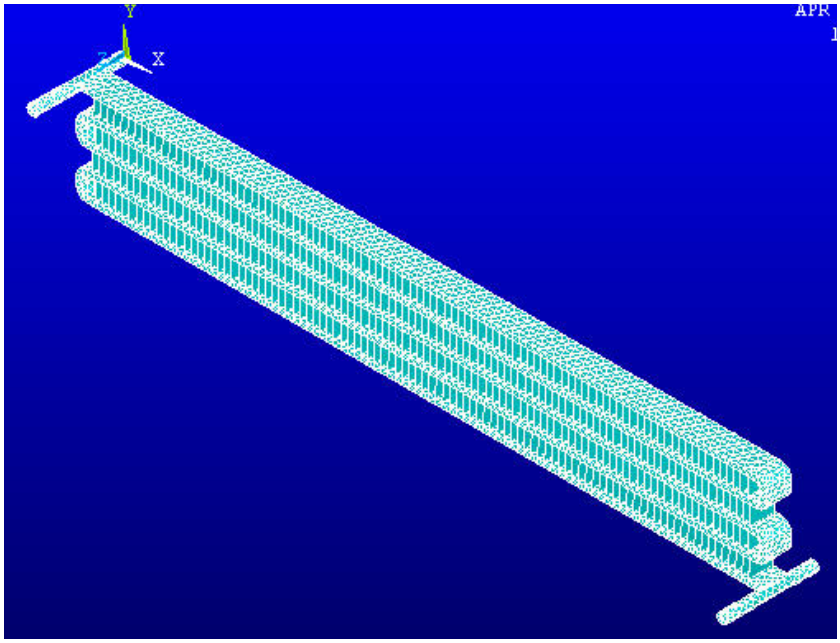

Figure 6.36. 5-pass HX unit with 300 *mm* in each pass

6.4.4 Harmonic Analysis

The harmonic response analysis is a technique used to determine the steady-state response of a linear structure to loads that vary sinusoidally (*harmonically*) in time. The idea is to calculate the structure's response at several frequencies to obtain a graph of some response quantity (usually displacements) versus frequency. "Peak" responses are then identified on the graph and stresses reviewed at those peak frequencies. Further, this analysis technique allows only for the calculation of the steady-state, forced vibrations of a structure. The transient vibrations, which occur at the beginning of the excitation, are not accounted for in a harmonic response analysis.

A schematic diagram of a linear system is shown in Figure 6.37. The linear system is identified with the frequency-response function $H_x(\omega)$.

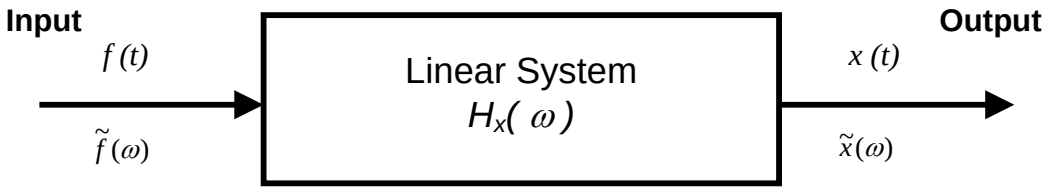

Figure 6.37. Schematic of a linear system

For a harmonic input *f(t)* and an output *x(t)*, the frequency domain forms are given in Equation (6.3).

$$\tilde{x}(\omega) = \mathcal{F}\left(x(t)\right)$$

$$\tilde{f}(\omega) = \mathcal{F}\left(f(t)\right) \tag{6.3}$$

The frequency-response function $H_x(\omega)$ can be used as follows:

$$\tilde{x}(\omega) = H_x(\omega)\ \tilde{f}(\omega) \tag{6.4}$$

Furthermore, from random vibrations, the power spectral density (or autospectral density function) $S_{xx}(\omega)$ can be predicted by using the frequency-response function, as follows:

$$S_{xx}(\omega) = \left|H_x(\omega)\right|^2\ S_{ff}(\omega) \tag{6.5}$$

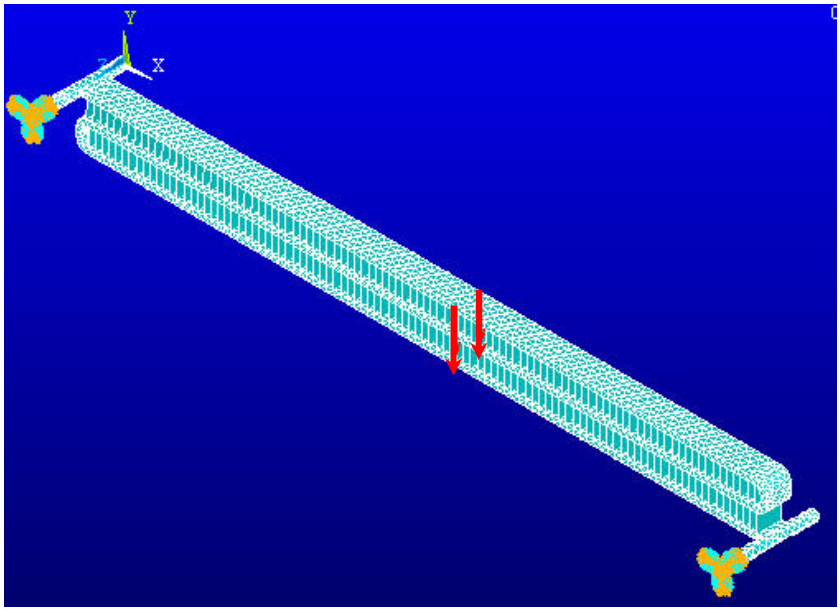

Figure 6.38. Harmonic forces on clamped-clamped HX unit

Harmonic response analysis is carried out for the HX unit shown in Figure 6.33. The harmonic forces are applied on the top center of the clamped-clamped HX unit, as shown in Figure 6.38.

When the displacement of the top center, where the harmonic forces are applied, is chosen as the output, the frequency-response function for a damping ratio of 0.1 is as calculated in Figure 6.39. As shown, the maximum displacement is located at a frequency of 72 *Hz*, which is very close to the first natural frequency of 71.9 *Hz*. This is not surprising, since the maximum vibration amplitude is expected to be near the natural frequencies.

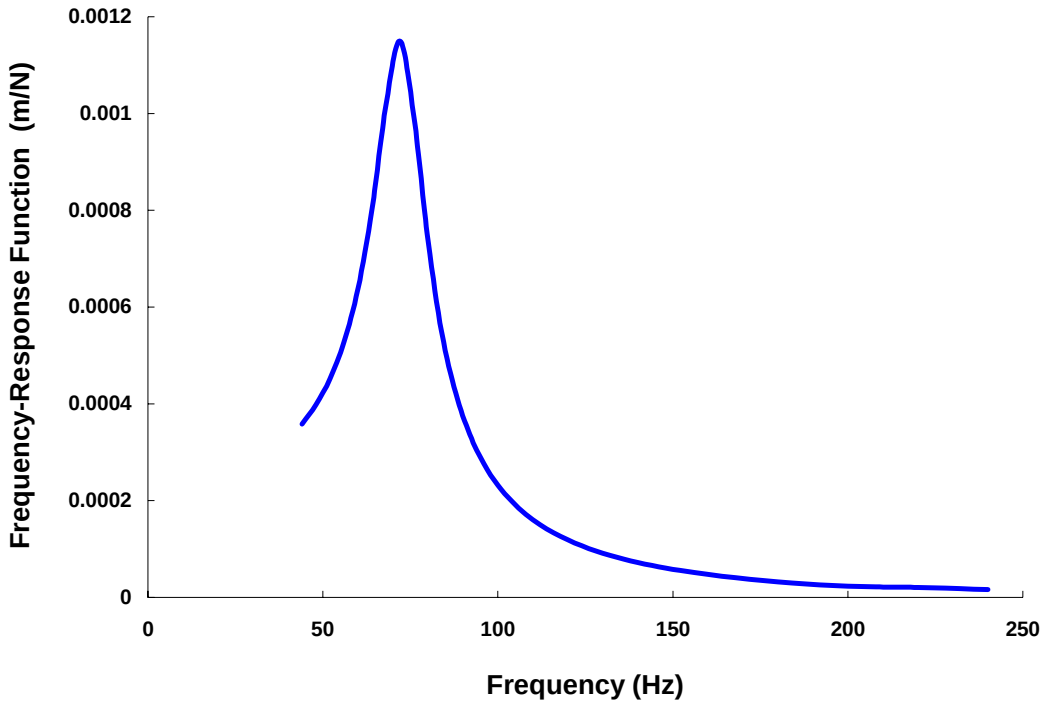

Figure 6.39. Frequency-response function with damping ratio of 0.1

In Figure 6.40, the stress distribution is shown for harmonic forces at a frequency of 72 *Hz*. The maximum stress is located at the junction between the microchannels tube and the headers.

For various pass lengths and pass numbers, the maximum amplitude of the frequency-response function (FRF) for a dumping ratio of 0.1 is calculated through harmonic response analysis, and the results are shown in Figure 6.41.

With harmonic forcing, the maximum vibration amplitude increases dramatically as the pass length increases. This suggests that severe damage may be caused to HX units with long pass lengths. The harmonic response analysis can be applied to any location of the HX unit, along any direction.

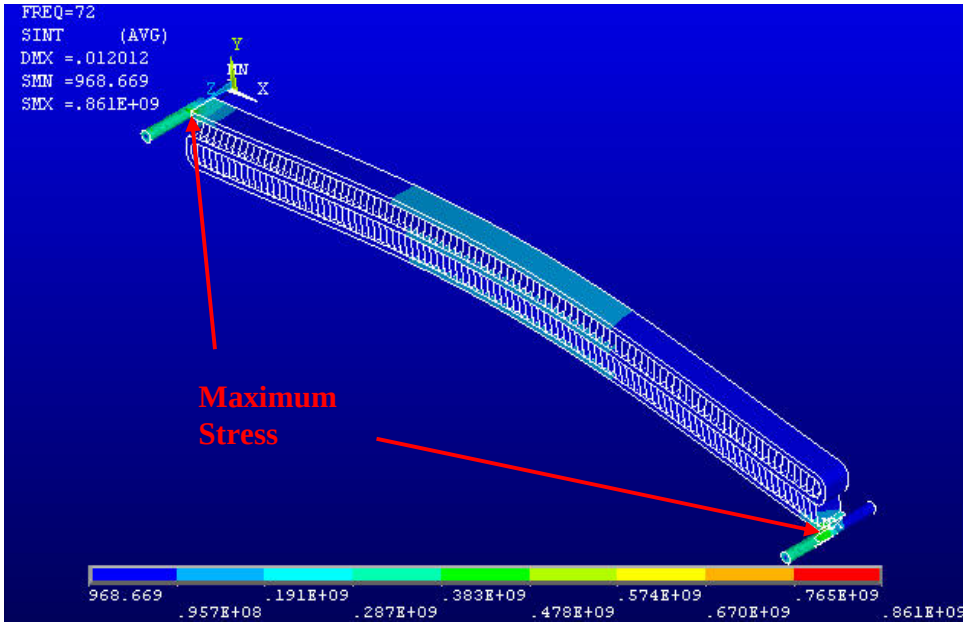

Figure 6.40. Stress distribution with harmonic forces at 72Hz

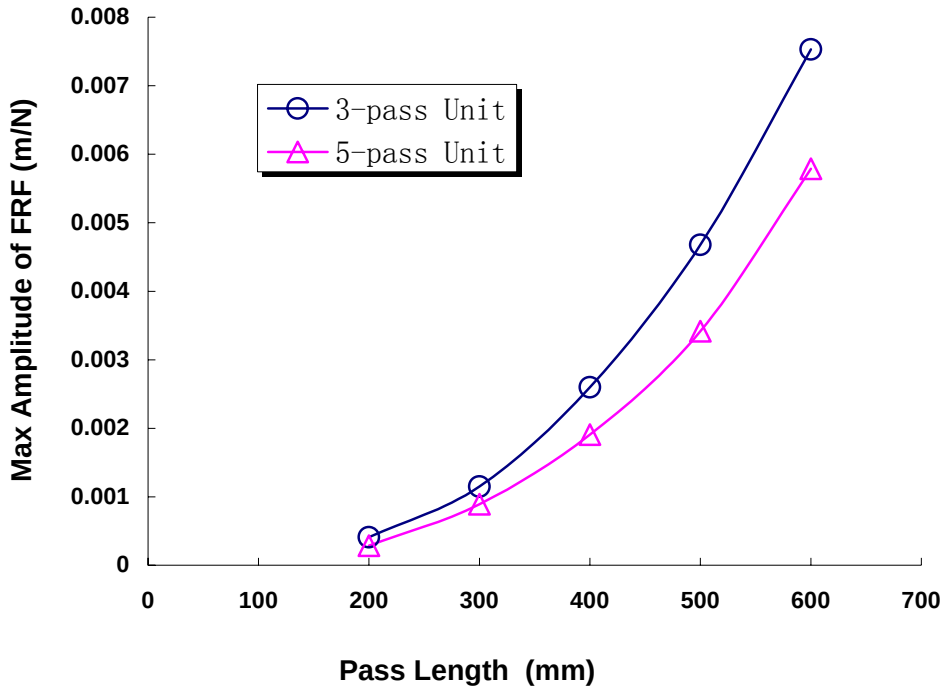

Figure 6.41. Max amplitude of FRF versus pass length

6.5 Case Study: Thermal and Mechanical Evaluation of a Heat Exchanger Design

In the previous sections, a FEM based analysis of tube-fin heat exchangers was used to develop a model for HX design, which was validated through experimental results. The present work can serve as a guide for structural and mechanical design analysis of heat exchangers for a variety of applications.

In this section, examples of a thermal and mechanical evaluation of a heat exchanger design are given, and the effects of fin geometry are evaluated. The clamped-

clamped tube-fin heat exchanger unit shown in Figure 6.42, which has 3 passes with 300 *mm* per pass, is studied.

For thermal evaluation purposes, airflow with velocity of 3.0 *m/s* is assumed to blow across the heat exchanger unit. The thermal boundary condition was assumed to have a constant heat flux of 15000 W/m^2 from the microchannel tubes. The software FLUENT was employed for the thermal analysis and ANSYS was employed for the dynamic analysis.

In Figure 6.43, the fin geometry is shown on the left, this includes two identical "fin units". In the numerical simulations with FLUENT, only one quarter of one fin unit is modeled (Figure 6.40, right side) by using symmetry boundary conditions. The definition of the fin thickness and the fin pitch are also illustrated in the figure.

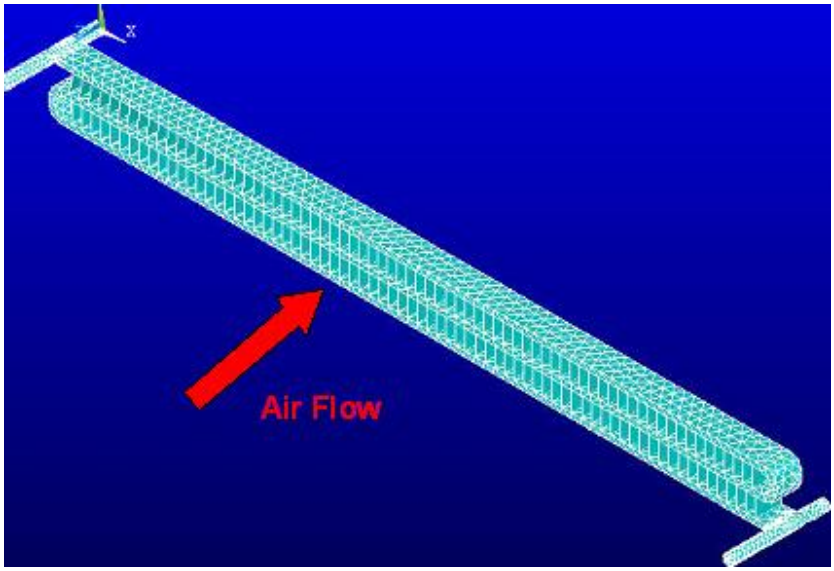

Figure 6.42. Evaluated heat exchanger unit

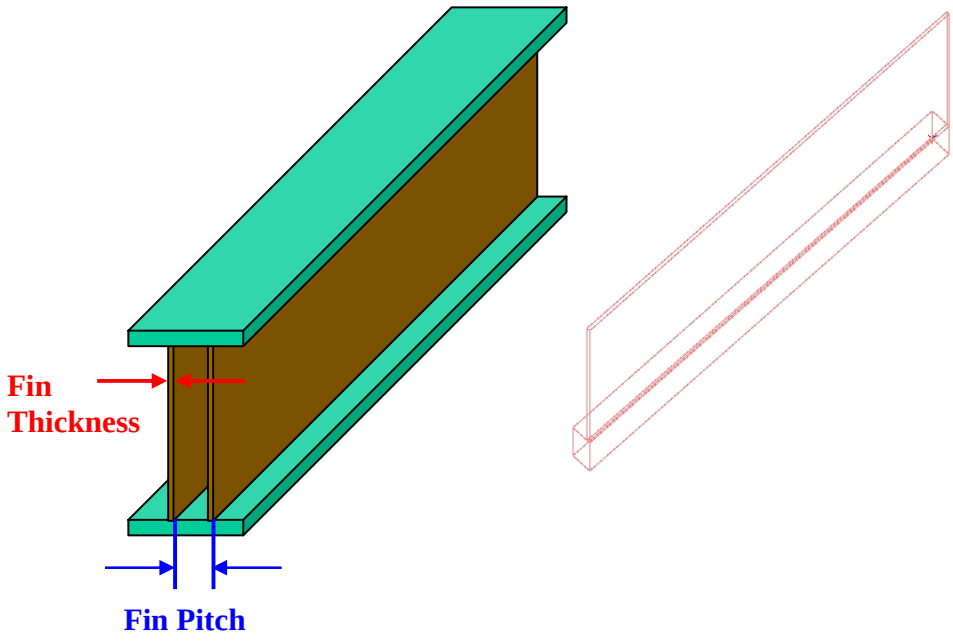

Figure 6.43. Simulation model in FLUENT

In Figure 6.44 and 6.45, the simulation results are presented to show the effect of fin thickness. As the fin thickness increases, the first natural frequency of the HX unit decreases, while the heat transfer coefficient, the pressure drop, and the density of the HX increase. In the other words, thicker fins have a positive effect on heat transfer, but a negative effect on pressure drop, material saving, and the dynamic characteristics.

In Figure 6.46 and 6.47, the simulation results are shown to illustrate the effect of fin pitch. As the fin pitch increases, the first natural frequency of the HX unit increases, while the heat transfer coefficient, the pressure drop, and the density of the HX decrease. A larger fin pitch has the opposite effect compared to a thicker fin.

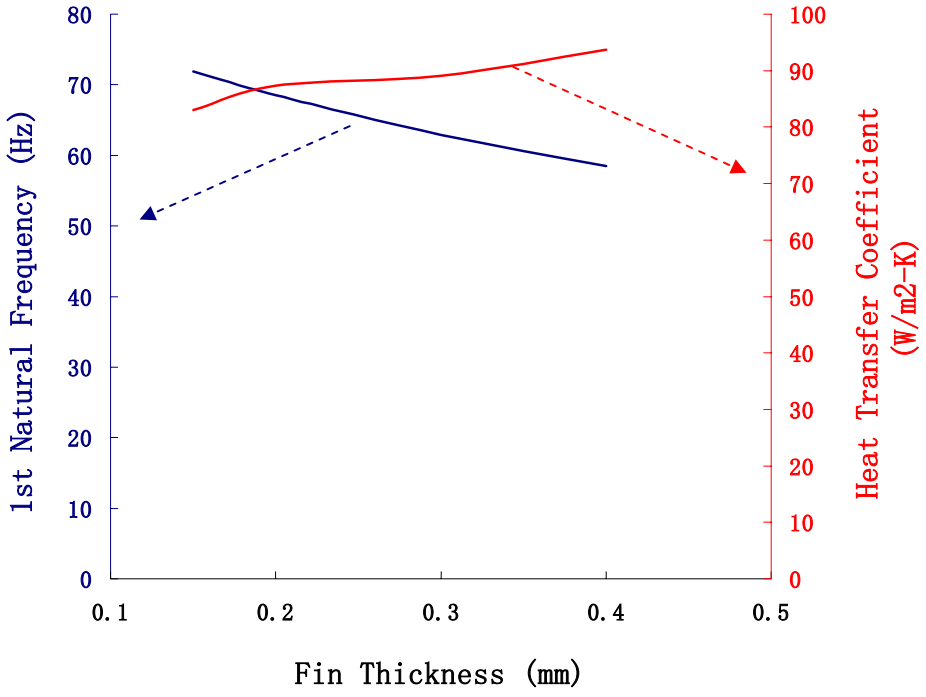

Figure 6.44. First natural frequency and heat transfer coefficient versus fin thickness

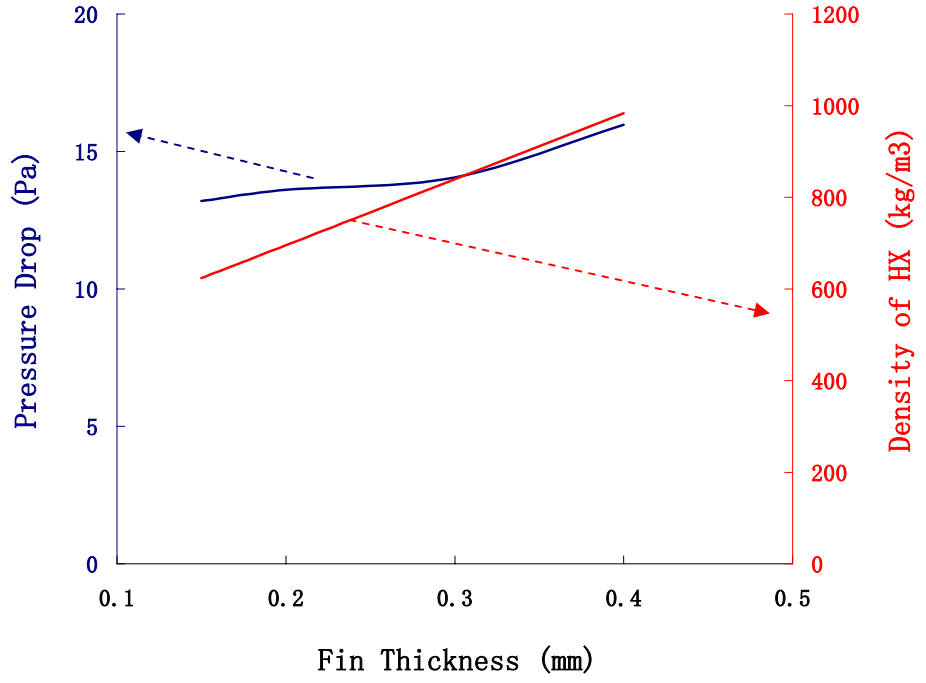

Figure 6.45. Pressure drop and HX density versus fin thickness

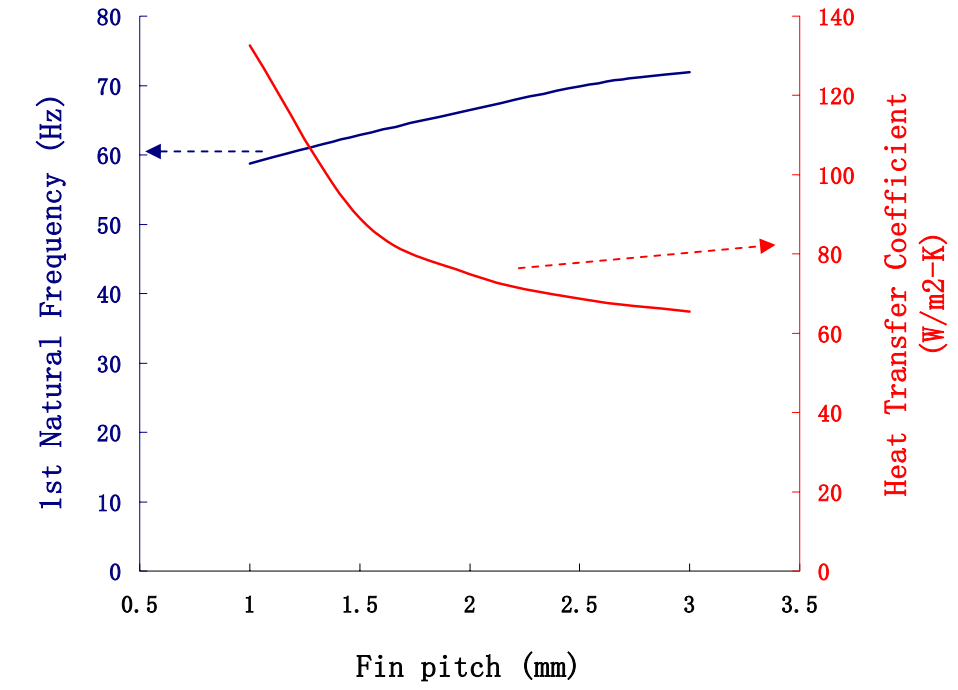

Figure 6.46. First natural frequency and heat transfer coefficient versus fin pitch

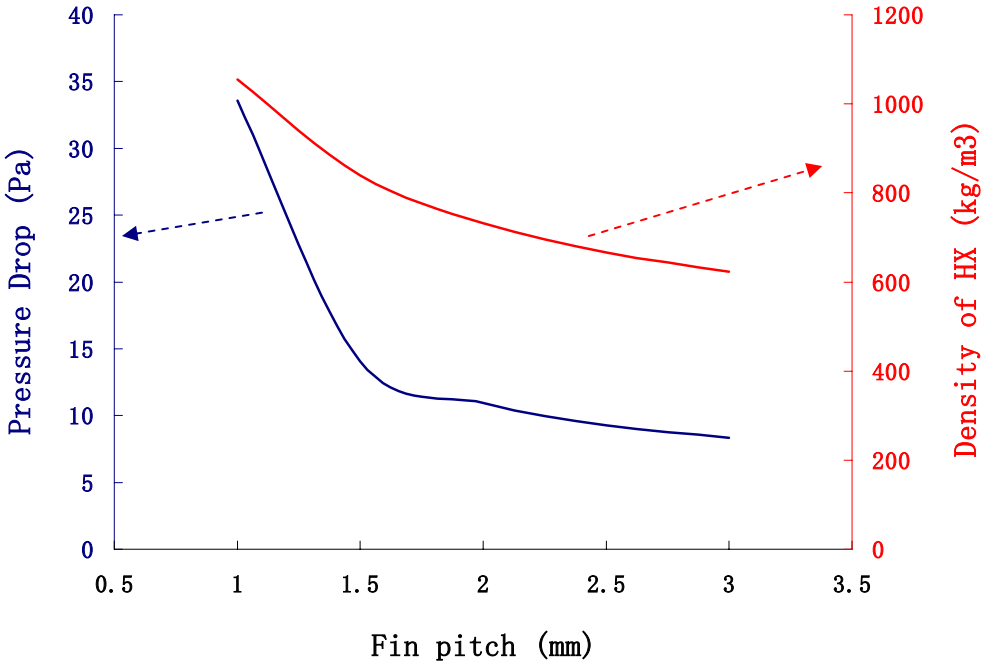

Figure 6.47. Pressure drop and HX density versus fin pitch

In heat exchanger design, there is a trade-off between all these factors, depending on the design goals. The present research on the FEM model of the tube-fin heat exchanger provides an effective guide for structural and mechanical design analysis to achieve such goals.

6.6 Design Guideline

The present work can serve as a guide for structural and mechanical design analysis of heat exchangers for a variety of applications. The guideline can be summarized as the following steps:

1) Determine the bending axis or vibration direction of concern. Based such assumption, generate equivalent geometry to simplify the physical model. In the other words, different solid models are required for different vibrating models;

2) Perform fin approximation for tube-fin heat exchangers. Two different methods, shell-element approximation and effective-block approximation, may fulfill the need. Shell-element approximation requires strictly perpendicular-parallel fin arrays, where effective-block approximation works for general cases.

3) Apply sub-structuring technique for large-scale structure modeling, which effectively reduce the computational workload.

4) Generate a solid model of the heat exchangers.

5) Perform design analysis of concern on the developed solid model.

6.7 Conclusions

A FEM based analysis of tube-fin heat exchangers has been carried out to develop a model for HX thermal and mechanical design. The solid modeling and simulation scheme included fin approximation as the first step, followed by modeling of large-scale structures using the sub-structuring method. Two alternative methods were proposed to approximate the fins, and the results were found to be similar. The experimental results also showed good agreement with the developed model results. Temperature gradient in the heat exchanger unit was found to have a minor effect on the natural frequencies, while an increase in the pressure significant increased the natural frequencies.

Dynamic analysis, in the form of modal analysis and harmonic response analysis, was performed to study the effect of geometry of the HX unit. Pass length had the dominant influence on natural frequencies. Increasing the pass length leads to a drop in natural frequencies. Higher pass numbers slightly decrease the natural frequencies.

A case study was conducted to evaluate both the dynamic and thermal performance of heat exchangers with different fin geometries. The effects of fin thickness and fin pitch were studied. Natural frequency, heat transfer coefficient, pressure drop, and density of heat exchanger show different trends for different fin geometry parameters. In practice, the goal of design of heat exchangers is to determine a reasonable trade-off between the fin geometry parameters.

The present work can serve as a guide for structural and mechanical design analysis of heat exchangers for a variety of applications. The developed modeling approach enables structural design to be carried out in parallel with thermal design. The

mathematical model developed in this study can serve as an effective tool for the design of practical heat exchangers that need to meet both mechanical and thermal requirements in conventional and harsh-environment operating conditions.

CHAPTER 7

CONCLUSIONS AND FUTURE WORK

7.1 Conclusions

The current study presented an experimental investigation on the gas cooling heat transfer characteristics of supercritical CO_2 in microchannels. Based on the experimental data collected, a semi-empirical correlation was developed to predict heat transfer coefficients of supercritical CO_2 in microchannels. The effect of oil addition on heat transfer and pressure drop performance was experimentally investigated as well.

In addition, a finite-element method (FEM) based analysis of tube-fin heat exchangers was carried out to develop a simulation model of heat exchanger mechanical design. This solid modeling and simulation scheme can serve as an effective design guide for the mechanical design of CO_2 heat exchangers.

7.1.1 Gas Cooling of Supercritical CO_2 in Microchannels

A series of experiments were conducted to investigate gas cooling heat transfer characteristics of supercritical CO_2 in microchannels. The tested microchannel tubes included 11 ports, each with channel diameter of 0.79 *mm*. A modified Wilson plot method was employed to determine the thermal resistance of the water side. Heat transfer and pressure drop coefficients were measured in each test run. The effects of temperature, pressure, and mass flux were studied in the experiments. The uncertainty analysis showed errors within 20% for most experimental data. Results showed that mass flux had a

significant effect on both heat transfer and pressure drop coefficients. The higher the mass flux, the larger the associated heat transfer and pressure drop coefficients.

It was found that pseudo-critical temperature plays an important role in the supercritical region. Heat transfer coefficient is enhanced near the pseudo-critical temperature, mainly because of the large specific heat. When the pressure changes, the peak of the heat transfer coefficient shifts, just as the pseudo-critical temperature does. It was also found that the peak value is enhanced when the pressure approaches critical pressure.

Experimental data on pressure drop were compared with Colebrook-White's correlation (1938). Some deviation was observed at low temperatures, caused by uneven thermo-physical properties at low temperatures and effects due to flow mal-distributions.

An extensive review of the literature indicated a lack of comprehensive data that fully explains the heat transfer characteristics in gas cooling of supercritical CO_2 in microchannels. The present study partially supplements the database for future design and applications of microchannel heat exchangers with CO_2 as the working fluid. Such heat exchangers might have a wide range of applications in industry, particularly in the refrigeration and air conditioning, automotive, and process industries.

7.1.2 Empirical Correlation Development

It was found that the conventional heat transfer correlation (Gnielinski's correlation) for forced convection, in-tube flow failed to predict the experimental data near the pseudo-critical region, where the thermophysical properties have uneven values. Due to the difficulty in dealing with the steep property variations in the supercritical

region, satisfactory analytical methods have not been developed yet. Therefore, empirical generalized correlations based on experimental data are usually used to predict the heat transfer coefficient near supercritical pressure.

As outlined in details in Chapter 4, Gnielinski's correlation, Krasnoshchekov-Protopopov's correlation, Ghajar-Asadi's correlation, Pitla et al's correlation, and Huai et al's correlation were selected for comparison with the present experimental results for pure supercritical CO_2 gas cooling in microchannel tubes. These correlations using the curve-fitting technique showed a better match with the experimental data of the present study.

A new empirical correlation was proposed in this study to predict the heat transfer of the supercritical gas cooling process in microchannel tubes. The new model is based on Ghajar-Asadi's correlation and re-defines the average specific heat to account for the effect of fluctuation along the whole test section, since, based on experimental data, the heat transfer coefficient is strongly dependent on specific heat, and the local specific heat has extremely uneven values along the test section. Using the specific heat at the mean temperature simply overlooks such fluctuations along the test section.

Since it is the average value of heat transfer coefficient along the test section that is measured, it is reasonable to integrate the average specific heat along the test section into the correlation. The newly developed predicting model agrees quite well with the experimental data within an error of 15% for most (91%) experimental data.

A literature review shows that no general correlation has yet been developed for predicting heat transfer performance in the supercritical region. The present study partially fulfills this need.

7.1.3 Gas Cooling of CO_2/Oil Mixtures in Microchannels

In the present study, efforts were focused on investigating the influence of oils on the gas cooling heat transfer and pressure drop characteristics of supercritical CO_2 in microchannels.

Different oils, PAG/AN (immiscible), PAG (immiscible), and POE (miscible), were experimentally studied as a function of such operational conditions as oil concentration and temperature. Tests were conducted in a horizontal circular microchannel tube with a hydraulic diameter of 0.79 *mm*. The heat transfer and pressure drop coefficients were measured. The experimental data chosen in the temperature region were around the pseudo-critical temperature, with a given pressure of 9 *Mpa* and mass flux of 890 kg/m^2-*s*. The studied range of oil concentration (weight percent) was between 0 *wt%* to 5 *wt%*.

As expected, oil addition has a significant negative effect on both heat transfer and pressure drop coefficients, increasing flow resistance and thermal resistance to the channel wall, due to the small size of the microchannels. At higher oil concentrations the heat transfer coefficients are substantially lower and the pressure drops are substantially higher. The heat transfer coefficient decreases by up to 57% for immiscible oil PAG/AN and 38% for miscible oil POE at oil concentration of 5 wt.% , operating pressure of 9 *MPa*, and mass flux of 890 kg/m^2-*s*. The pressure drop increases by up to 49% for immiscible oil PAG and 20% for miscible oil POE.

The immiscible oil had a stronger negative effect on the pressure drops than the miscible oil. This is understandable because miscible oil usually mixes better with CO_2 than immiscible oil.

No previous study in the open literature has investigated the supercritical oil/CO_2 mixtures. The present study provides the first set of comprehensive data that addresses the oils' effects on heat transfer performance in the supercritical region in microchannels, and thus it establishes a database for design purposes and further future work in this area.

7.1.4 Mechanical Design Analysis of Microchannels CO_2 Heat Exchanger

The present study systematically developed a model for microchannel heat exchangers. A FEM-based analysis of tube-fin heat exchangers was developed as a model for heat exchanger design. The solid modeling and simulation scheme starts with fin approximation, followed by modeling of large-scale structure using the sub-structuring method. Two alternative methods were proposed to approximate the fin, with similar results.

Experiments were conducted to check the validation of the simulation model. The experimental data on the natural frequencies showed good agreement with the developed model. Temperature gradient in the heat exchanger unit was found to have a minor effect on the natural frequencies, while the inner high pressure shows significant enhancement on natural frequencies.

Dynamic analysis, such as modal analysis and harmonic response analysis, was performed to study the effect of the geometry of the HX unit. Pass length was found to have the dominant influence on natural frequencies. Increasing pass length leads to a drop

in natural frequencies. A higher pass number of HX unit slightly decreases the natural frequencies.

A case study was conducted to evaluate both the dynamic and thermal performance of heat exchangers with different fin geometries. The effects of fin thickness and fin pitch were studied. Natural frequency, heat transfer coefficient, pressure drop, and density of heat exchanger show different trends for different fin geometry parameters. In practice, the goal of design of heat exchangers is to determine a reasonable trade-off between the fin geometry parameters.

An extensive literature review indicated that no previous study has dealt with the systematic development of a model of heat exchanger for such structural and dynamical design. This study certainly fulfilled this need and can serve as a guide for structural and mechanical design analysis of heat exchangers for a variety of applications. The developed modeling approach allows the structural design to be carried out in parallel with the thermal design. A detailed guideline is summarized in the chapter as well.

In the mechanical design analysis of tube-fin heat exchangers, it is found that the fin approximation is essential and critical, which will directly affect the accuracy of the final results. The pass length of the heat exchanger plays dominant role for dynamic characteristics, while the pass number has slight effect. The larger the pass length, the lower the natural frequencies. A heat exchanger design with long pass should be avoided in this matter.

7.2 Future Work

During the course of this project, many questions, ideas and opportunities became apparent and are included here. The work includes recalling and discussing important phenomena of CO_2 and microchannel heat exchangers, and proposing problems for future study, some of which are given in the following section.

7.2.1 Un-Pairing Thermal Resistances in Test Section

The overall thermal resistance of heat exchanging in the test section consists of thermal resistances from the water side and CO_2 side. The heat transfer coefficient of the water side is fixed in all the tests. From an uncertainty analysis point of view, the accuracy of the heat transfer coefficient in CO_2 side directly depends on its magnitude. The larger the heat transfer coefficient, the less the accuracy.

It is obvious that improvement of the heat transfer at the water side would help at some level. But in order to ensure a certain level of temperature difference of the water between the inlet and outlet, the heat transfer is limited by the low mass flow rate of water. A smaller temperature difference would enlarge the uncertainty caused by temperature measurement.

The heat transfer coefficient near the pseudo-critical temperature is much larger than that far from the pseudo-critical temperature. If the mass flux of CO_2 is also large, the heat transfer coefficient will become as high as up to 10-20 times of that on the water side. In such cases, most of the thermal resistance is from the water side, which magnifies the uncertainty of the calculation of heat transfer coefficient on the CO_2 side.

Therefore, taking into account the above observations, to investigate the heat transfer characteristics near the pseudo-critical temperature in the supercritical region, more experimental data is needed for small and moderate mass fluxes.

7.2.2 Oil Separation Techniques

Oil addition in supercritical CO_2 has been shown to have significant negative effects on heat and mass transfer performance. Furthermore, it forms carbon sludge during circulation, which is detrimental to all parts of the system. It is essential to separate the oil from the CO_2 after it leaves the pump.

Currently the industry applies passive separation techniques in traditional vapor compression systems. Three examples are given in Figure 7.1, Figure 7.2 and Figure 7.3.

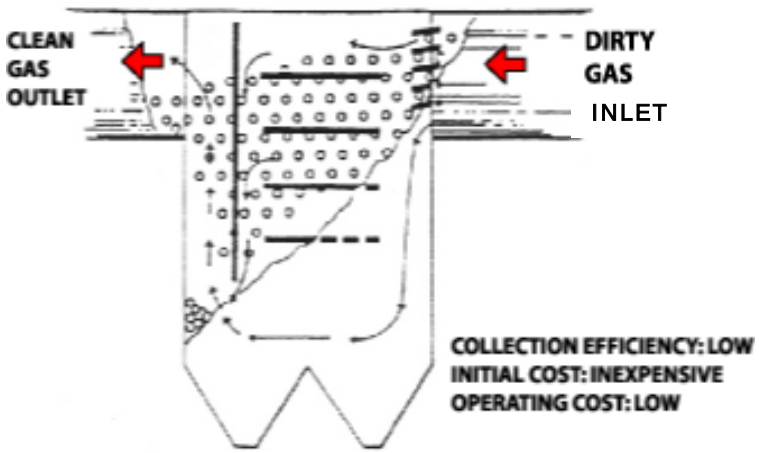

Figure 7.1. Settling chamber oil separator

Figure 7.2. Coalescing filtration oil separator

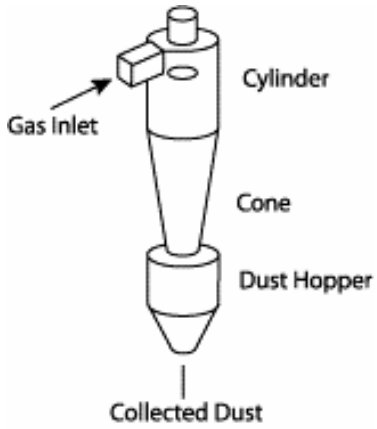

Figure 7.3. Cyclone oil separator

Figure 7.1 shows a settling chamber oil separator. Oil particles are collected by force of gravity. This kind of oil separator is inexpensive to manufacture and operate.

However, the collection efficiency is low, and it typically works only for very large particles with sizes from > 60 ~ 100 μm.

A coalescing filtration oil separator is shown in Figure 7.2. The filter is used to capture the oil particles. Obviously, the size of collected particles depends on the mesh size of the filter. The pressure drop is relatively large due to the filter, and dirty clogging is expected after a certain operating time.

In Figure 7.3, a cyclone oil separator is presented. Like the impactor oil separator, oil is separated from refrigerant due to the inertial difference. Therefore, the efficiency of oil separation is dependent on the inertial difference, and subsequently, on the size of oil particles. Very poor efficiency has been found for capturing small droplets in the fogging region.

Generally, the density of the oil is about 900 kg/m^3. In CO_2 heat exchangers, the supercritical CO_2 temperature may be up to 100 ℃ with pressure up to 10 *MPa* at the exit of the compressor. At such conditions, the density of CO_2 is around 180 kg/m^3, compared with R134a's density of 60 kg/m^3. The smaller difference of inertia, when compared to R-134a, makes it more difficult to separate oil from supercritical CO_2 using traditional, passive oil separation techniques.

With its promising performance, the Electrohydrodynamics (EHD) technique may fulfill the challenging requirement for oil separation with supercritical CO_2. Further research in this area is important.

7.2.3 Mechanical Design of Microchannels HX

A solid model of microchannel heat exchangers was established in the present study. Modal analysis was performed to obtain the natural frequencies and vibrating mode shapes. Harmonic response analysis was performed to predict the amplitude of vibration and the relative stress distribution. In the future work, one may evaluate the impact analysis by conducting a study of the dynamic response of heat exchangers to impact behaviors.

The current project studied modeling of the heat exchanger itself. The flow inside the heat exchanger was not included. In engineering practice, the effect of the inside flow cannot be ignored, not only because of its additional mass, but also because of the interactivity between the flow and the heat exchanger, and thus its impact on vibration analysis and mechanical design of the heat exchanger. Further study on the effect of the flow inside the heat exchanger will certainly enhance the current solid modeling of microchannel heat exchangers.

7.2.4 Additional Recommendations for Future Work

The current project experimentally investigated the heat transfer characteristics of supercritical CO_2 gas cooling in microchannels and established a solid model of microchannel heat exchangers for mechanical design analysis. Additional research is needed to expand the database. For future research, the following specific additional work is recommended to develop a better understanding of supercritical CO_2 gas cooling

in microchannels and a better solid modeling of microchannel heat exchangers for mechanical design analysis.

i) Conduct more experiments with small and moderate mass flux near pseudo-critical temperature.

ii) Conduct more experiments with microchannels for different hydraulic diameters.

iii) Develop a numerical model for supercritical CO_2 gas cooling in microchannels.

iv) Conduct experiments on oil separation from supercritical CO_2 with EHD technology, building up in what already exists in this area.

v) Perform impact analysis with microchannels heat exchanger via FEM modeling.

vi) Develop a solid model of microchannels heat exchanger with inside fluid flow. The current work assumed static flow conditions.

REFERENCES

Admas, T.M., S.I. Abdel-Khalik, S.M. Jeter and Z.H. Qureshi, 1998, "An Experimental Investigation of Single-phase Forced Convection in Microchannels," *Int. J. Heat Mass Transfer* 41(6): 851-857.

ASHRAE Handbook of Fundamentals, 2005, SI Edn, ASHRAE Inc., Atlanta, GA.

Balachandran, B. and E.B. Magrab, 2003, *Vibrations*, Brooks/Cole-Thomson Learning, CA.

Bouhaddi, N. and R. Fillod, 1996, "Model Reduction by a Simplified Variant of Dynamic Condensation", *Journal of Sound and Vibration*, Vol. 191, No. 2, pp233-250.

Bouma, J.W.J., 1993, "Global Warming and Heat Pumps", Proceedings of the 4th International Energy Agency Heat Pump Conference, Maastricht, Neth, pp33-42.

Bourke, P.J., D.J. Pulling, L.E. Gill, and W.H. Denton, 1970, "Forced Convective Heat Transfer to Turbulent Carbon Dioxide in the Supercritical Region", *International Journal of Heat and Mass Transfer*, Vol.13, pp1339-1348.

Bringer, R.P. and J.M. Smith, 1957, "Heat Transfer in Critical Region", *AIChE Journal*, Vol.3, No.1, pp49-55.

Chang, Y., C.T. Hsu, and C. Wang, 1996, "Single-Tube Performance of Condensation of R-134a on Horizontal Enhanced Tubes", *ASHRAE Transactions: Symposia*, pp821-829.

Cheung, Y.K. and A.Y.T. Leung, 1991, *Finite Element Methods in Dynamics*, Kluwer Academic Publishers and Science Press, Hong Kong.

Choi, S.B., R.F. Barron, and R.O. Warrington, 1991, "Liquid Flow and Heat Transfer in Microtubes," *Micromechanical Sensors, Actuators and Systems*, ASME DSC 32: 123-134.

Colebrook, C. F., 1938-1939, "Turbulent Flow in Pipes with Particular Reference to the Transition Region between Smooth and Rough Pipe Laws", *Journal of the Institution of Civil Engineers*, Vol. 11, pp. 133-156.

Craig, R.R. Jr., 1995, "Substructure Methods in Vibration", *Journal of Mechanical Design, Transactions of the ASME*, Vol. 117B, pp207-213, June.

Cutler, B., Y.H. Hwang, L. Bogdanic, and R. Radermacher, 2000, "Development of A Transcritical Carbon Dioxide Environmental Control Unit," *IIF-IIR Commission* B1, B2, E1, and E2, Purdue University.

Ghajar A.T and A. Asadi, 1986, "Improved Forced Convec-tive Heat Transfer Correlation for Liquids in the Near Critical Region", *AIAA Journal* Vol. 24, No 12, pp.2030-2037.

Gnielinski, V., 1976, "New Equations for Heat and Mass Transfer in Turbulent Pipe and Channel Flow", *Int. Chemical Engineering*, 16, pp359-368.

Green, J.R. and E.G. Harptmann, 1971, "Forced Convective Heat Transfer from a Cylinder in Carbon Dioxide Near the Thermodynamic Critical Point", *ASME Transactions, Journal of Heat Transfer*, Vol.93, pp290-296.

Hartmann, F. and C. Katz, 2004, *Structure Analysis with Finite Elements*, Springer, New York.

Hauk, A., and E. Weidner, 2000, "Thermodynamic and Fluid-Dynamic Properties of Carbon Dioxide with Different Lubricants in Cooling Circuits for Automobile Application", *Ind. Eng. Chem. Res.*, Vol. 39, pp4646-4651.

Huai X.L., S. Koyama, and T.S. Zhao, 2005, "An Experimental Study of Flow and Heat Transfer of Supercritical Carbon Dioxide in Multi-Port Mini Channels under Cooling Conditions", Chemical Engineering Science, Vol. 40, pp3337-3345.

Hwang, Y., 1997, "Comprehensive Investigation of Carbon Dioxide Refrigeration Cycle", Ph.D. Dissertation, University of Maryland.

http://www.mscsoftware.com.au/services/cases/macro/

Kakac, S. and H. Liu, 2002, *Heat Exchangers: Selection, Rating, and Thermal Design*, 2nd edition, CRC Press, Boca Raton.

Kaliakin, V.N., 2002, *Introduction to Approximate Solutions Techniques, Numerical Modeling, and Finite Element Methods*, Marcel Dekker, New York.

Kays, W.M. and A.L. London, 1984, *Compact Heat Exchangers*, 3rd edition, McGraw-Hill Book Company, New York.

Krasnoshchekov, E.A. and V.S. Protopopov, 1966, "Experimental Study of Heat Exchange in Carbon Dioxide in the Supercritical Range at High Temperature Point", High Temperature, Vol.4, No.3, pp375-382.

Kuang, G., M. Ohadi, and Y. Zhao, 2003, "Experimental study of miscible and immiscible oil effects on heat transfer coefficients and pressure drop in microchannel gas cooling of supercritical CO2", *Proceedings of 2003 ASME Summer Heat Transfer Conference*, Las Vegas, Nevada, July 21-23, 2003, pp671-675.

Kuang, G., M. Ohadi, and Y. Zhao, 2004, “Experimental Study on Gas Cooling Heat Transfer for Supercritical CO2 in Microchannels”, 2nd *International Conference on Microchannels and Minichannels (ICMM2004),* Rochester, NY, June 17-19, pp325-332.

Kuang, G., B. Balachandran, M. Ohadi, and Y. Zhao, 2004, “Advanced Micro Channel Heat Exchangers -- Structural and Mechanical Design Analysis”, *Proceedings of ASME IMECE04 2004 ASME International Mechanical Engineering Congress and Exposition*, Anaheim, CA, November 13-20, pp37-42.

Kuppan, T., 2000, *Heat Exchanger Design Handbook*, Marcel Dekker, New York.

Leung, Y.T., 1979, “An Accurate Method of Dynamic Substructuring with Simplified Computation”, *International Journal for Numerical Methods in Engineering*, Vol. 14, pp1241-1256.

Liao, S.M. and T.S. Zhao, 2002, “An experimental investigation of convection heat transfer to supercritical carbon dioxide in miniature tubes”, *Int. Journal of Heat and Mass Transfer*, v 45, pp 5025-5034, June.

Liao, S.M. and T.S. Zhao, 2002, “Measurements of Heat Transfer Coefficients from Supercritical Carbon Dioxide Flowing in Horizontal Mini/Micro Channels”, *Journal of Heat Transfer*, Vol. 124, pp413-420, June.

Lorentzen, G., 1995, “The Use of Natural Refrigerants: A Complete Solution to the CFC/IICFC Replacement,” *Int. J. Refrig.*, Vol. 18(3): 190-197.

Micropolskii, L. and M.E. Shitsman, 1957, "Heat Transfer to Water and Steam at Variable Specific Heat (in Near Critical Region) ", *Soviet Physics-Technical Physics*, Vol.2, No10, pp2196-2208.

Mills, A.F., 1995, "Heat and Mass Transfer", Richard D. Irwin, Inc.

Morales, C. A., 2000, "Rayleigh-Ritz Based Substructure Synthesis for Multiply Supported Structures," *Journal of Vibration and Acoustics* Vol. 122, no. 1, pp2-6.

Ohadi, M.M. and B. Mo, 1997, "Natural Refrigerants—Historical Development, Recent Research, and Future Trends", *Proceedings, 1997 Taipei International Conference on Ozone Layer Protection*, Dec 9-10, Taipei, Taiwan.

Olson, D.A. and D. Allen, 1998, “Heat Transfer in Turbulent Supercritical Carbon Dioxide Flowing in a Heated Horizontal Tube,” NISTIR 6234.

Ortiz, T.M. and E.A. Groll, 2000, “Steady-State Thermal Finite-Element Analysis of A Microchannel CO2 Evaporator,” *IIF-IIR Commission* B1, B2, E1, and E2, Puerdue University.

Peng, X.F. and G.P. Peterson, 1996, “Convective Heat Transfer and Flow Friction for Water Flow in Microchannel Structures,” *Int. J. of Heat Mass Transfer* 39(12): 2599-2608.

Perelmuter, A.V. and V.I. Slivker, 2003, *Numerical Structure Analysis: Methods, Models and Pitfalls*, Springer, New York.

Pettersen, J., A. Hafner, G. Skaugen and H. Rekstad, 1998, “Development of Compact Heat Exchangers for CO_2 Air-Conditioning Systems,” *Int. J. Refri.* 21(3): 180-193.

Pettersen, J., R. Rieberer, and S.T. Munkejord, 2000, "Heat Transfer and Pressure Drop for Flow of Supercritical and Subcritical CO2 in Microchannel Tubes", *Final Report for US Army*, Contract No. N-68171-99-M-5674.

Petukhov, B.S., E.A. Krasnoshchekov and V.S. Protopopov, 1961, “An Investigation of Heat Transfer to Fluids Flowing in Pipes Under Supercritical Conditions”, *Proceedings of the 2nd International Heat Transfer Conference*, pp569-578.

Pfahler, J., J. Harley, H.H. Bau, and J. Zemel, 1991, “Gas and Liquid Flow in Small Channels,” Micromechanical Sensors, Actuators and Systems, ASME DSC 32: 49-60.

Pitla, S., D. Robinson, E. Groll, and S. Ramadhyani, 1998, “Heat Transfer from Supercritical Carbon Dioxide in Tube Flow: A Critical Review”, *HVAC&R Research*, Vol. 4, No. 3, pp281-301.

Pitla, S., K. Bhatia, V. Khetarpal, and G. Strikis, 2000, “Numerical Heat Transfer Analysis in Heat Exchangers for Transcritical CO_2 System,” *IIF-IIR Commission* B1, B2, E1, and E2, Purdue University.

Pitla, S., E. Groll, and S. Ramadhyani, 2001, “Convective Heat Transfer From In-Tube Cooling of Turbulent Supercritical Carbon Dioxide: Part 2 – Experimental Data and Numerical Predictions”, *HVAC&R Research*, Vol. 7, No. 4, pp367-382.

Pitla, S., E. Groll, and S. Ramadhyani, 2002, “New Correlation to Predict the Heat Transfer Coefficient during In-Tube Cooling of Turbulent Supercritical CO_2”, International Journal of Refrigeration, Vol. 25, pp887-895.

Petrov, N.E. and V.N. Popov, 1985, “Heat Transfer and Resistance of Carbon Dioxide Being Cooled in the Supercritical Region”. *Thermal Engineering*, 32 (3), pp131-134.

Ravigururajan, T.S., J. Cuta, C.E. McDonald, and M.K. Drost, 1996, “Single-Phase Flow Thermal Performance Characteristics of a Parallel Micro-Channel Heat Exchanger,” *ASME, Heat Transfer Division, (Publication) HTD Proceedings of the 31st ASME National Heat Transfer Conference*. Part 7 (of 8), v 329, n 7, Houston, TX.

Riehl, R.R., P. Jr. Seleghim, and J.M. Ochterbeck, 1998, “Comparison of Heat Transfer Correlations for Single- and Two-Phase Microchannel Flows for Microelectronics Cooling”, *1998 InterSociety Conference on Thermal Phenomena*, pp409-416.

Singh, K.P., and A.I. Soler, 1984, *Mechanical Design of Heat Exchangers and Pressure Vessel Components*, Joseph Oat Corp., Camden, NJ, USA.

Smith E.M., 1997, *Thermal Design of Heat Exchangers - A Numerical Approach: Direct Sizing & Stepwise Rating*, John Wiley & Sons, Inc., New York.

Swamee P.K. and A.K. Jain, 1975, "Explicit Equations for Pipe-Flow Problems", *Journal of the Hydraulic Division, Proc. of the American Society of Civil Engineers*, Vol.102, No.HY5, pp657-664.

Wang, B.X. and X.F. Peng, 1994, “Experimental Investigation on Liquid Forced-Convection Heat Transfer through Microchannels,” *Int. J. Heat Mass Transfer* 37(Suppl. 1): 73-82.

Webb, R.L. and M. Zhang, 1997, “Heat Transfer and Friction in Small Diameter Channels,” Presented at Workshop on Thermophysical Phenomena in Microscale Sensors, Devices and Structures, 1997 National Heat Transfer Conference, Baltimore, MD.

Wei, D., Y.T. Ma, et al., 2002, “Research on Heat Transfer to Supercritical Carbon Dioxide in Tube Flow”, *Journal of Engineering Thermophysics*, Vol. 23, No. 1, pp85-88.

West, H.H. and L.F. Geschwindner, 2002, *Fundamentals of Structural Analysis*, John Wiley, New York.

Yamagata, K., K. Nishikawa, S. Hasegawa, T. Fujii, S. Yoshida, 1972, "Forced Convective Heat Transfer to Supercritical Water Flowing in Tubes", *International Journal of Heat and Mass Transfer*, Vol.15, pp2575-2593.

Yang, Y.C. and R.L. Webb, 1996, "Friction Pressure Drop of R-12 in Small Hydraulic Diameter Extruded Aluminum Tubes With and Without Micro-fins", *International Journal of Heat and Mass Transfer*, Vol.39, No.5, pp801-809.

Yee, A. and T. Leung, 1978, “An Accurate Method of Dynamic Condensation in Structural Analysis”, *International Journal for Numerical Methods in Engineering*, Vol. 12, pp1705-1715.

Yoon, S.H., J.H. Kim, et al., 2003, “Heat Transfer and Pressure Drop Characteristics during the In-Tube Cooling Process of Carbon Dioxide in the Supercritical Region”, *International Journal of Refrigeration*, Vol. 23, pp857-864.

Zhao, Y., 2001, "Flow Boiling Characteristics of Carbon Dioxide in Microchannles", Ph.D. Dissertation, University of Maryland.

Zhao, Y., M. Molki and M.M. Ohadi, 2000, “Heat Transfer and Pressure Drop of CO_2 Flow Boiling in Microchannels,” Proceedings of the ASME Heat Transfer Division, HTD-366(2): 243 – 248.